VSB TECHNICAL UNIVERSITY OF OSTRAVA | FACULTY OF ELECTRICAL ENGINEERING AND COMPUTER SCIENCE

Modelling of Transport Properties of Molecular Ions of Helium in Air

Modelování transportních vlastností molekulových iontů helia ve vzduchu

Ing. Martin Beseda

PhD Thesis

Supervisors:

prof. RNDr. René Kalus, Ph.D.,

prof. Thierry Leininger, Ph.D.,

MCF-HDR Malika Benhenni, Ph.D.

Ostrava, 2022

There is always a well-known solution to every human problem – neat, plausible, and wrong.

H. L. Mencken

Abstrakt a přínos práce

Tato práce je zaměřena na modelování transportních vlastností chladného plazmatu na bázi helia při interakci s dusíkem v atmosféře. Hlavním zaměřením této práce je důkladný popis molekulárních interakcí. Získané výsledky jsou dále předávány do simulací molekulové dynamiky a mezoskopických modelů transportních vlastností. Interakce jsou získávány ab initio přístupem s využitím metod Multi-Configurational Self-Consistent Field a Multi-Reference Configuration Interaction spolu s Numerovovou metodou pro řešení Schrödingerovy rovnice při výpočtu rotačně-vibračních excitací. Molekulová dynamika je počítání hybridním kvantově-klasickým přístupem, kdy jsou jádra popisována klasicky a elektrony kvantově. Kromě toho jsou v dynamických simulacích využity nejen ab initio metody „za běhu“, ale také umělé neuronové sítě, aby se zkrátila doba potřebná pro výpočetně náročné konfigurace. Transportní vlastnosti kolizních komplexů jsou modelovány Monte Carlo přístupem. V této práci je provedena důkladná analýza molekulových interakcí pro základní a první excitované stavy N_2^+ a N_2^+/He je dáno s ohledem na různé báze, orbitální prostory a metody. Chování je popsáno nejen pro hodnoty potenciální energie, ale i pro různé rotačně-vibrační excitace N_2^+ a předběžné výsledky jsou uvedeny až po 11. excitovaný stav N_2^+ a 7. excitovaný stav N_2^+/He. Jak reaktivní, tak nereaktivní účinné průřezy byly získány ze simulací molekulové dynamiky a následně porovnány s pseudoexperimentálními daty získanými z měření mobilit. V této souvislosti byl podrobně analyzován také vliv vodorovného vyrovnání N_2^+ na výsledné účinné průřezy. Konečně, mezoskopické modelování bylo zaměřeno na získání mobility N_2^+ v He, charakteristických energií podélné i příčné difuze a rychlostní konstanty N_2^+ difuze indukované srážkou s He. Zatímco tak toto téma není vyčerpáno, tyto teoretické poznatky jsou již užitečné pro další experimentální výzkum a pomáhají s „tuningem“ studeného plazmatu pro specifické aplikace.

Klíčová slova

studené plazma; dusík; helium; MCSCF; MRCI; molekulová dynamika; ab initio; Monte Carlo; transportní vlasnosti

Abstract and Contributions

This thesis is focused on modeling of the transport properties of helium-based cold plasma in the interaction with nitrogen in the atmosphere. The main focus of this thesis is on thorough description of molecular interactions. The obtained results are further passed into molecular dynamics simulations and mesoscopic models of transport properties. The interactions are obtained via ab initio approach, utilizing Multi-Configurational Self-Consistent Field and Multi-Reference Configuration Interaction methods together with Numerov method for solving Schrödinger equation when computing vibrational-rotational excitations. Molecular dynamics is being performed in a hybrid quantum-classical approach, as nuclei are being treated classically and electrons in a quantum manner. Furthermore, not only ab initio methods on-the-fly, but also Artificial Neural Networks are involved in the dynamics simulations to reduce necessary runtime for the most expensive parts. Transport properties of the collision complexes are modelled using Monte Carlo. In this thesis, a thorough analysis of the molecular interactions for the ground and the first excited states of N_2^+ and N_2^+/He is given, with respect to different basis sets, orbital spaces and methods. The behavior is evaluated not only for the values of potential energy, but also for different rotational-vibrational excitations of N_2^+ and the preliminary results are also provided for the higher excited states up to 11th one and the 7th one in the case of N_2^+ and N_2^+/He , respectively. Both reactive and non-reactive cross-sections were obtained from molecular dynamics simulations and compared subsequently with the pseudo-experimental data obtained from mobility measurements. In this context, also the effect of the N_2^+ horizontal alignment on the resulting cross-sections was analyzed in detail. Finally, the mesoscopic modeling part was focused on obtaining N_2^+ mobility, in He gas, the characteristic energies of both longitudinal and transversal diffusion and the rate constant of N_2^+ diffusion induced by collision with He. That said, while the topic is not exhausted in any way, these theoretical findings are already useful for further experimental research, helping with “tuning” cold plasma for specific applications.

Keywords

cold plasma; nitrogen; helium; MCSCF; MRCI; molecular dynamics; ab initio; Monte Carlo; transport properties

Acknowledgement

I would like to thank prof. RNDr. René Kalus, Ph.D., prof. Thierry Leininger, Ph.D., and MCF-HDR Malika Benhenni, Ph.D. for the supervision of my thesis, and prof. Florent Xavier Gadéa, Ph.D. for all the valuable insights. I also thank Bc. Silvie Illésová for all the advice, support, and patience during the last years. The other thanks belong to my family and friends for all the support and faith in the optimistic outcome. And last, but not least, I thank all my students who kept me motivated and who showed me, that basics usually deserve many more repetitions than I would expect.

Contents

Acronyms

ANN artificial neural network

AO atomic orbital

AV5Z aug-cc-pV5Z

AV6Z aug-cc-pV6Z

AVQZ aug-cc-pVQZ

AVQZ′ aug-cc-pVQZ(spdf)

AVTZ aug-cc-pVTZ

BO Born-Oppenheimer

BOA Born-Oppenheimer approximation

CAS complete active space

CASSCF complete-active-space self-consistent field

CI configuration interaction

CID *collision-induced dissociation*

CISD configuration interaction singles and doubles

CSF configuration state function

EOMs equations of motion

FFANN feed-forward ANN

HF Hartree-Fock

IC initial condition

ic-MRCI internally-contracted MRCI

IM *inverse method*

IP ionization potential

IVP initial value problem

LCAO linear combination of atomic orbitals

MCSCF multi-configurational self-consistent field

MDS molecular dynamics simulation

ML machine learning

MO molecular orbital

MRCI multi-reference configuration interaction

MRCISD MRCI singles and doubles

MT momentum-transfer

MTCS momentum-transfer cross-section

MTCS1 type 1 MTCS

MTCS2 type 2 MTCS

NAC non-adiabatic coupling

NO natural orbital

NRS *non-reactive scattering*

OS orbital space

OS1 orbital space 1

OS2 orbital space 2

OS3 orbital space 3

OS4 orbital space 4

PDE partial differential equation

PEC *potential energy curve*

PES potential energy surface

PIP permutation invariant polynomial

QC quantum chemistry

QCT quasi-classical trajectory

QM quantum mechanics

RG rare-gas

RHF *restricted Hartree-Fock*

SCF self-consistent field

SD Slater determinant

SE Schrödinger equation

SoA state-of-the-art

SRCI single-reference CI

TCIE truncated configuration interaction expansion

TDSE time-dependent Schrödinger equation

TISE time-independent Schrödinger equation

uc-MRCISD uc-MRCI singles and doubles

uc-MRCI uncontracted MRCI

List of Figures

List of Tables

Chapter 1

Introduction

Plasma is one of the four fundamental states of matter consisting of atoms, ions, and free electrons e^-. The share of ions is characterized by *ionization degree* α given by

$$\alpha = \frac{n_i}{n_i + n_0}, \tag{1.1}$$

with n_i and n_0 being the number density of ions and neutral atoms, respectively. With a growing amount of ions, the collision frequency grows accordingly, with Coulomb (electron-ion) collisions ν_{ei} becoming more frequent than electron-neutral ν_{en} ones if $n_i > n_0$. If $\nu_{\mathrm{ei}} >> \nu_{\mathrm{en}}$, we talk about *fully ionized gas* [1] and a *weakly ionized gas* if $\nu_{\mathrm{ei}} << \nu_{\mathrm{en}}$. We further refer to ionized gases where the temperature of electrons T_{e} is equal to the temperature of atoms and ions T_{ai} as *thermal plasma* and to the case where $T_{\mathrm{e}} > T_{\mathrm{ai}}$ as *non-thermal* plasma. That said, while T_{e} can be high, T_{ai} can be around room temperature in non-thermal plasmas, making it possible to be in contact with various objects (like human skin) without causing any harm to them. Note also that a special case of the non-thermal plasma exists where ions' temperature is much higher than the temperature of electrons, i.e. where $T_{\mathrm{ai}} >> T_{\mathrm{e}}$.

Rare-gas (RG) based cold plasmas seem to be one of the widely researched topics in nowadays plasma physics, molecular physics, and chemistry, mostly due to wide experimentally-proven applications and extensive potential. The most prominent application areas seem to be food processing [2, 3, 4], surface treatment [5, 6, 7] and plasma medicine [8, 9, 10, 11], which is the closest one to our research motivations due to a long-term research involvement of LAPLACE research centre[1] in the field [12, 13]. While the experimental evidence is already wide, the common problem of applications, most significantly seen in the biomedical field, is a poor understanding of the underlying principles. Like in many cases, there is no detailed explanation of the experimental results [13] with promising application potential. Such a lack

[1] `www.laplace.univ-tlse.fr`

of a deeper understanding hinders our ability to adjust the used substances to fit our specific needs [14].

The process of plasma generating is based on a cascade ionization occurring in the gas called *Townsend discharge* [15] which leads to an avalanche breakdown, i.e. gives rise to conductivity in a gas. The main ingredient of a plasma generator is a gas (so-called carrier and/or buffer gas) flowing under the influence of an electric field, thus speeding up free electrons which subsequently free other electrons, multiplying the number of free ones and so creating ions from previously neutral atoms. This process is schematically illustrated in Figure 1.1.

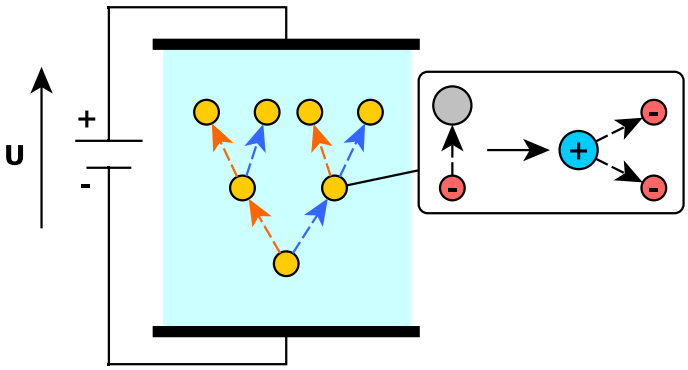

Figure 1.1: Townsend avalanche process

Yellow circles represent ionization events, grey circles an atom, and blue and red circles $p^+$and e^-, respectively. Orange arrows then represent paths of newly liberated $e^-$and blue arrows paths of the original ionizing e^-.

That said, experimental experience is already wide and cold plasmas are usually generated using either *dielectric barrier discharge* or "pin-to-hole" devices [16], with *plasma jet* being the most prominent example. Its simplified scheme can be seen in Figure 1.2, where the red line highlights the area of the first collisions between He^+ and the air. The in-depth description of collisions in this area is also the main motivation behind this dissertation thesis. While Ne, Ar, Kr and Xe are all being used as carrier-gas for plasma generating [17, 18, 19], He was chosen in this thesis because of its simplicity, i.e. low number of electrons and low mass. Both of these properties are numerically convenient, as they allowed us to work with a computationally-easier problem than the other gases and to ignore occurring relativistic effects, most prominently spin-orbit interaction. That said, He provided also one *a priori* known numerical difficulty – the high ionization potential (IP) 24.6 eV.

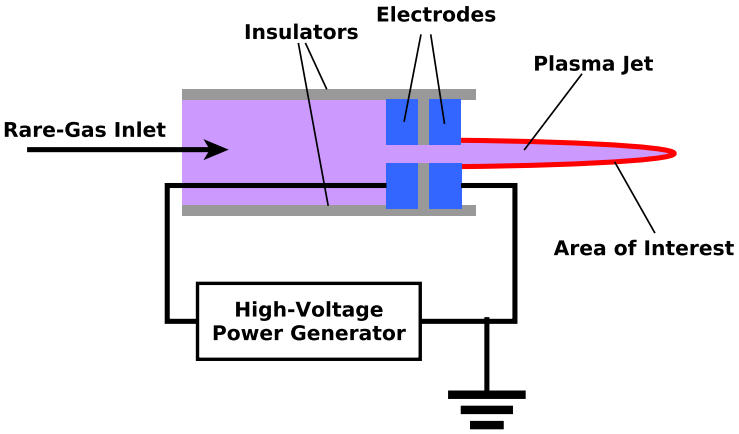

Figure 1.2: Plasma jet generator

As a consequence, the collision-induced charge transfer,

$$\mathrm{He}^+ + \mathrm{N}_2 \rightarrow \mathrm{N}_2^+ + \mathrm{He} \tag{1.2}$$

$$\mathrm{He}^+ + \mathrm{N}_2 \rightarrow \mathrm{N}^+ + \mathrm{N} + \mathrm{He} \tag{1.3}$$

$$\mathrm{He}^+ + \mathrm{N}_2 \rightarrow [\mathrm{NHe}]^+ + \mathrm{N} \tag{1.4}$$

represent the very first step of the interaction of the helium plasma jet with the atmosphere, He being the most widely used RG in biomedical applications and N_2 being the most abundant air molecule, and as seen in Equation (1.4), when the charge transfer occurs between them, secondary ions N_2^+, N^+ (and theoretically also $[NHe]^+$) are produced. We will focus on modeling the interactions of these secondary ions, especially of N_2^+, with the carrier gas He.

While an extensive experimental work focused on reactions of RG atoms with N_2^+ has been done in this area [20, 21, 22, 23, 24, 25], theoretical results are not nearly as frequent and neither their extent nor their accuracy are sufficient for practical usage [26, 27, 28, 29, 30, 31, 32, 33]. The final goal of our research efforts has been to perform efficient nonadiabatic molecular dynamics simulations (MDSs) and their subsequent confirmation by comparison with available experimental data. In this thesis, then, I aimed to a) obtain an in-depth description of the electronic structure of the collision complexes given by Equation (1.4), i.e. their potential energy surfaces (PESs) and gradients, b) represent PESs together with gradients via machine learning (ML) based methods, most notably utilizing fundamental invariant polynomials as the systems' descriptors.

This thesis directly follows Van de Steen's work [18, 34, 35, 36] focused on processes of an avalanche ionization occurring inside plasma generators. It is focused predominantly on the microscopic modeling phase, i.e. ab initio computations of electron interactions, thus obtaining PESs together with their gradients and their representation via machine-learning

approach, namely artificial neural networks (ANNs) combined with permutation invariant polynomials (PIPs) as descriptors. As this approach combines the benefit of ab initio accuracy with computational demands nearing these of empirical models.

The next section of this thesis introduces basic technical concepts followed by a description of adopted numerical methods. In the third section, the computational details and settings are listed together with descriptions of PES-representation approaches. The fourth section further summarizes all the results achieved during the thesis together with their comparison against state-of-the-art (SoA) computations. Eventually, the possible future application and the following research outlook are outlined.

Chapter 2

Theory

In this section, the basic terms are introduced considering all phases of the dissertation project – computations of interactions, i.e. quantum chemistry, molecular dynamics simulations, and mesoscopic modeling aiming to obtain relevant transport properties. The text is written in a general, introductory manner, as the specific computational details are described in the following section.

2.1 Quantum Chemistry

To introduce the relevant quantum chemistry terms, this section goes over an elaborate description of both time-dependent and time-independent variants of the Schrödinger equation, followed by the description of the Born-Oppenheimer approximation, thus decreasing the dimension of the solved problems and the related distinction between the electronic and the nuclear Schrödinger equation. Finally, the section ends with a brief description of a charge density and several numerical methods to obtain its values.

2.1.1 Time-Independent Schrödinger Equation

Similarly to classical mechanics, it is necessary to be equipped with an equation describing the behavior of a physical system in time and also in the field of Quantum mechanics (QM). Considering a non-relativistic, conservative system we can describe its time-dependent evolution via Time-dependent Schrödinger equation (TDSE). The equation takes a vital position in QM, as it is also one of its foundational postulates [37].

That said, the meaning of TDSE formulation is apparent, when the total energy of a classical system is given by the equation

$$E = \frac{\vec{p}^2}{2m} + V(\vec{r}), \tag{2.1}$$

with $\vec{p}^2 = p_x^2 + p_y^2 + p_z^2$ denoting a scalar product of two momentum vectors $\vec{p} = (p_x, p_y, p_z)$, m denoting the total relativistic mass of the system and $V(\vec{r})$ being a general potential function depending on a vector of coordinates $\vec{r}$, is considered first. Subsequently, a substitution

$$E \to i\hbar \frac{\partial}{\partial t} \tag{2.2}$$

$$\vec{p} \to -i\hbar \nabla \tag{2.3}$$

can be performed, thus obtaining an operator equation, holding its meaning when applied to a wavefunction $\psi(\vec{r}, t)$ depending on both spatial coordinates $\vec{r}$ and time t. Bearing that in mind, inserting $\psi(\vec{r}, t)$ in the equation finally provides

$$i\hbar \frac{\partial}{\partial t} \psi(\vec{r}, t) = \left(-\frac{\hbar^2}{2m} \Delta + V(\vec{r}) \right) \psi(\vec{r}, t), \tag{2.4}$$

where Δ stands for a scalar product of gradients $\nabla = (\frac{\partial}{\partial x}, \frac{\partial}{\partial y}, \frac{\partial}{\partial z})$, i.e. for *Laplace operator*. As can be seen, the bracket on the right-hand side of Equation (2.4) represents a linear self-adjoint operator which is conventionally called the Hamilton operator (or briefly the Hamiltonian $\widehat{H}$), i.e.

$$\widehat{H} = \left(-\frac{\hbar^2}{2m} \Delta + V(\vec{r}) \right). \tag{2.5}$$

Given both Equation (2.4) and Equation (2.5) together with the fact, that it is a first-order partial differential equation (PDE) in time, a need arises to have an initial condition to be able to determine $\psi(\vec{r}, t)$. Thus, the time-dependent evolution of a non-relativistic physical system in QM is determined via initial value problem (IVP)

$$\widehat{H} \psi(\vec{r}, t) = i\hbar \frac{\partial}{\partial t} \psi(\vec{r}, t), \tag{2.6}$$

$$\psi(\vec{r}, t_0) = \psi_0, \tag{2.7}$$

where (t_0, ψ_0) denotes the initial condition (IC).

Being equipped with TDSE, i.e. Equations (2.6) and (2.7) and assuming time-independent $\widehat{H}$ given by Equation (2.5), we can non-rigorously describe derivation of the equation relevant for this thesis, i.e. Time-independent Schrödinger equation (TISE). Under the assumption, a wavefunction can be represented in the form

$$\psi(\vec{r}, t) = \omega(\vec{r}) \varphi(t), \tag{2.8}$$

thus we can perform *separation of variables* by substituting it into Equation (2.6) like

$$\left[-\frac{\hbar^2}{2m}\Delta + V(\vec{r})\right]\Big(\omega\left(\vec{r}\right)\varphi\left(t\right)\Big) = i\hbar\frac{\partial\omega(\vec{r})\varphi(t)}{\partial t} \tag{2.9}$$

$$-\frac{\hbar^2}{2m}\Delta\Big(\omega\left(\vec{r}\right)\varphi\left(t\right)\Big) + V(\vec{r})\Big(\omega\left(\vec{r}\right)\varphi\left(t\right)\Big) = i\hbar\frac{\partial\omega(\vec{r})\varphi(t)}{\partial t} \tag{2.10}$$

$$-\frac{\hbar^2}{2m}\varphi\left(t\right)\Delta\omega\left(\vec{r}\right) + V(\vec{r})\omega\left(\vec{r}\right)\varphi\left(t\right) = i\hbar\omega(\vec{r})\frac{\partial\varphi(t)}{\partial t} \tag{2.11}$$

$$-\frac{\hbar^2}{2m}\Delta\omega\left(\vec{r}\right) + V(\vec{r})\omega\left(\vec{r}\right) = \frac{i\hbar}{\varphi(t)}\omega(\vec{r})\frac{\partial\varphi(t)}{\partial t} \tag{2.12}$$

$$\left[-\frac{\hbar^2}{2m}\Delta + V(\vec{r})\right]\omega\left(\vec{r}\right) = \left[\frac{i\hbar}{\varphi(t)}\frac{\partial\varphi(t)}{\partial t}\right]\omega(\vec{r}) \tag{2.13}$$

$$\widehat{H}\omega\left(\vec{r}\right) = \left[\frac{i\hbar}{\varphi(t)}\frac{\partial\varphi(t)}{\partial t}\right]\omega(\vec{r}) \tag{2.14}$$

$$\frac{\widehat{H}\omega\left(\vec{r}\right)}{\omega(\vec{r})} = \frac{i\hbar}{\varphi(t)}\frac{\partial\varphi(t)}{\partial t}, \tag{2.15}$$

where, due to the fact, that both sides of Equation (2.15) hold for arbitrary coordinates $(\vec{r}, t)$ making them equal to the same energy constant E, i.e.

$$\frac{\widehat{H}\omega\left(\vec{r}\right)}{\omega(\vec{r})} = \frac{i\hbar}{\varphi(t)}\frac{\partial\varphi(t)}{\partial t}, \tag{2.16}$$

providing a system of two equations,

$$\widehat{H}\omega\left(\vec{r}\right) = E\omega(\vec{r}) \tag{2.17}$$

$$\frac{i\hbar}{\varphi(t)}\frac{\partial\varphi(t)}{\partial t} = E\varphi(t), \tag{2.18}$$

where Equation (2.17) is TISE. Since the measurable energies of a system are corresponding to the eigenvalues of $\widehat{H}$, i.e. its discrete spectrum, we can rewrite Equation (2.17) as

$$\widehat{H}\omega_n(\vec{r}) = E_n\omega_n(\vec{r}), \quad n = 1, 2, 3, \ldots \tag{2.19}$$

with n denoting the index of an eigenstate of $\widehat{H}$.

Finally, it is necessary to pinpoint, that in the rest of this thesis only TISE will be of importance, so that wavefunctions will be denoted as $\psi(\vec{r})$ albeit depending only on the spatial coordinate vector(s) to conform with usual literature notation.

That said, the TISE will be denoted as

$$\widehat{H}\psi_n(\vec{r}) = E_n\psi_n(\vec{r}), \quad n = 1, 2, 3, \ldots \tag{2.20}$$

2.1.2 Born-Oppenheimer Approximation

A PES is a function describing the potential energy V of a system depending on a chosen set of descriptors. Those are usually either Cartesian or, preferably, *internal coordinates*, i.e. coordinates, which do not depend on a position in an underlying domain but describe the system solely using relative positions of its particles by a specification of angles and distances among them. PESs can be defined in many ways, either by physics-based analytical formulas, regression models, or ANNs.

Very simple 1-dimensional example with r being an internuclear distance, D_e a bond strength and r_e a bond length (i.e. an equilibrium distance), can be seen in Figure 2.1. For $r < r_e$ repulsive forces together with V grow steeply (dominantly due to the Pauli repulsion [38]), while for $r > r_e$ bond strength gradually weakens together with V (e.g. induction forces or London dispersion interactions [39]). The position where no interaction between particles occurs is called a *dissociation*, and it is described by

$$\lim_{r\to\infty} V(r) = 0. \tag{2.21}$$

That said, we usually talk about a *dissociation distance* r_d in a context, where $V(r_d) \approx 0$, so that we can work with r_d, respectively a dissociation in general, numerically.

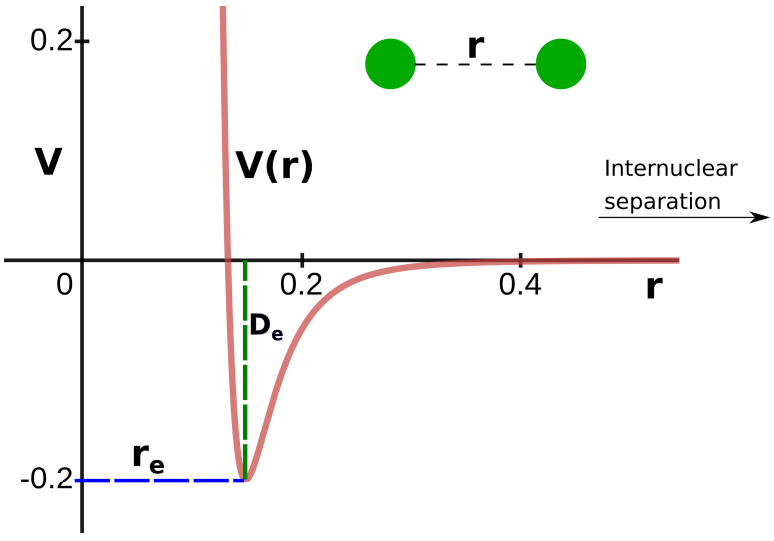

Figure 2.1: 1-D PES for $D_e = 0.2$ and $r_e = 0.15$

In this one-dimensional example of a two-particle system, the situation is straightforward - it is obvious that the internuclear distance itself is enough to describe the system completely. But, for systems with more particles ((non-linear in general) is the situation slightly more complex. Every n-particle system can be completely described by $3n$ coordinates, e.g. the Cartesian ones. In this context, we talk about $3n$ spatial *degrees of freedom* (DOFs). Now, while there are always $3n$ spatial DOFs to specify the n-particle system, they can be described in different ways. Considering three-dimensional space with an axis for every dimension, the whole system can be moved along all of them - i.e. *system translations* form a set of 3 DOFs. Furthermore, the system can be rotated around every axis, every time changing the position of at least some of its particles, except for the case where all the molecules are positioned along with one of the axes and the system rotates around it. Thus, *system rotations* form another set of 3 DOFs in a non-linear case or 2 DOFs if the system is linear. That said, the number of remaining DOFs for $3n - 6$ and $3n - 5$ DOFs for non-linear and linear systems, respectively. These are called, in the case of bound systems, *vibrational degrees of freedom* as they represent vibrations of particles around their equilibrium positions.

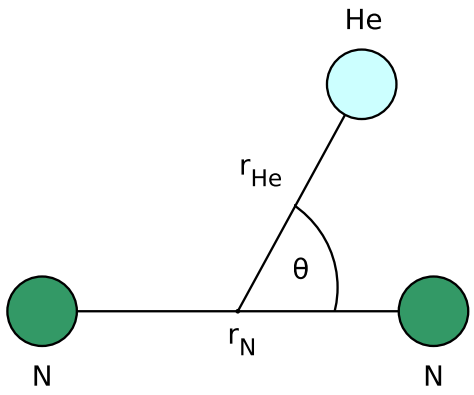

Figure 2.2: Internal coordinates for $[N_2/He]^+$ collision complex

As we work with a three-particle system and as such we need 3 DOFs in a general case, we adopted an internuclear distance between N atoms r_{N}, a distance between its center and a He atom r_{He} and an angle between those two lines θ, as our internal coordinates as can be seen in Figure 2.2. Thus, our PES is given as a function $V(r_{\mathrm{N}}, r_{\mathrm{He}}, \theta)$, depending on these three variables.

In order to obtain adiabatic PESs, we must first solve TISE, while the formulas

$$\widehat{H} = \widehat{T}_n + \widehat{V}_{nn} + \widehat{H}_e \tag{2.22}$$

$$\widehat{T}_n = -\sum_{A=1}^{M} \frac{1}{2m_A} \nabla_A^2 \tag{2.23}$$

$$\widehat{V}_{nn} = \sum_{A=1}^{M} \sum_{B=A+1}^{M} \frac{Z_A Z_B}{\vec{R}_{AB}} \tag{2.24}$$

$$\widehat{H}_e = \widehat{T}_e + \widehat{V}_{ee} + \widehat{V}_{en} \tag{2.25}$$

$$\widehat{T}_e = -\frac{1}{2} \sum_{i=1}^{N} \nabla_i^2 \tag{2.26}$$

$$\widehat{V}_{ee} = \sum_{i=1}^{N} \sum_{j=i+1}^{N} \frac{1}{\vec{r}_{ij}} \tag{2.27}$$

$$\widehat{V}_{en} = -\sum_{i=1}^{N} \sum_{A=1}^{M} \frac{Z_A}{\vec{r}_{Ai}}, \tag{2.28}$$

describe its Hamiltonian operator for M-body system in atomic units, with N, $\vec{r}$ and $\vec{R}_{AB}$ denoting the number of electrons, coordinates of i-th electron, and the distance between nuclei A and B. Given, that the Equation (2.20) with Equation (2.22) is obviously complex and subsequently difficult to solve numerically, we can use the fact, that nuclei move at about 10^{-3} of the electron speed and make the solution for electronic energies $E_e(\vec{R})$ and wavefunctions $\psi_e(\vec{r}, \vec{R})$ faster, as we can approximately consider nuclei being stationary. With that assumption, we can omit the $\hat{T}_n$ term. Furthermore, we can simplify Equation (2.22) by omitting $\hat{V}_{nn}$ term, as it is a constant, obtaining eventually *electronic Hamiltonian* $\widehat{H}_e$.

This procedure is called *Born-Oppenheimer approximation* [40]. Utilizing this simplification we can further work with the *electronic* TISE

$$\widehat{H}_e \psi_e(\vec{r}, \vec{R}) = E_e \psi_e(\vec{r}, \vec{R}).\text{,} \tag{2.29}$$

Considering the much faster movement of electrons compared to nuclei, it is a reasonable simplification to assume, that nuclei are moving in a mean-energy field, i.e. in relation to an average electronic coordinates, averaged over the electronic wavefunction $\psi_e(\vec{r}, \vec{R})$ [41]. This provides a nuclear Hamiltonian $\widehat{H}_n$ given by

$$\widehat{H}_n = \widehat{T}_n + \widehat{V}_{nn} + \left\langle \psi_e \middle| -\frac{1}{2} \sum_{i=1}^{N} \nabla_i^2 + \sum_{i=1}^{N} \sum_{j=i+1}^{N} \frac{1}{\vec{r}_{ij}} - \sum_{i=1}^{N} \sum_{A=1}^{M} \frac{Z_A}{\vec{r}_{Ai}} \middle| \psi_e \right\rangle \tag{2.30}$$

$$\widehat{H}_n = \widehat{T}_n + \widehat{V}_{nn} + \left\langle \widehat{H}_e \right\rangle, \tag{2.31}$$

where

$$\widetilde{E}_{\text{total}} = \widehat{V}_{nn} + \left\langle \widehat{H}_e \right\rangle, \tag{2.32}$$

with $\widetilde{E}_{\text{total}}$ denoting an approximation to the total energy, constitutes PES, i.e. a potential for nuclear motion under Born-Oppenheimer approximation (BOA). That said, nuclei under BOA move on PES obtained by solving the electronic problem given by Equation (2.29). Nuclear Schrödinger equation (SE)

$$\widehat{H}_n \psi_n(\vec{R}) = \widetilde{E}_{\text{total}} \psi_n(\vec{R}) \tag{2.33}$$

describes the vibration, rotation and translation of a molecule and $\widetilde{E}_{\text{total}}$ describes the sum of vibrational, rotational, translational, and electronic energy. In correspondence with that, BOA to the total energy wavefunction is

$$\psi(\vec{r}, \vec{R}) = \psi_e(\vec{r}, \vec{R}) \psi_n(\vec{R}). \tag{2.34}$$

Furthermore, local minima and saddle points of PESs correspond to *stable chemical species* and *transition states*, respectively. Thus, to fully utilize calculated PES, it is necessary to obtain also its first and second derivatives (gradients).

As the energy of every physical system is quantized, we differentiate between the configurations with the lowest one called *ground state* and the higher ones called *excited states*. Different PESs then correspond directly to these *electronic states*.

And finally, as the system can transition between states, we will also assess the probability of both radiative and non-radiative transitions as described in subsequent sections. The spin-orbit coupling will be omitted, as both He and N are very light elements, where spin-orbit interactions are not of much significance for theoretical spectroscopic computations, as can be seen in [42].

2.1.3 Hartree-Fock Approximation and Beyond

The Hartree-Fock (HF) method is one of the simplest approximations accounting properly for fermionic permutation symmetry [43]. The main idea behind the method lies in the variational optimization of a single-determinant n-electron wave function. The trial wavefunction is then defined via a Slater determinant (SD) as

$$\psi_T\left(\vec{x_1},\vec{x_2},\ldots,\vec{x}_n\right)=\frac{1}{\sqrt{n!}}\begin{vmatrix}\chi_1(\vec{x_1}|\theta_1) & \chi_2(\vec{x_1}|\theta_2) & \cdots & \chi_n(\vec{x_1}|\theta_n)\\ \chi_1(\vec{x_2}|\theta_1) & \chi_2(\vec{x_2}|\theta_2) & \cdots & \chi_n(\vec{x_2}|\theta_n)\\ \vdots & \vdots & \ddots & \vdots\\ \chi_1(\vec{x_n}|\theta_1) & \chi_2(\vec{x_n}|\theta_2) & \cdots & \chi_n(\vec{x_n}|\theta_n)\end{vmatrix} \tag{2.35}$$

$$=\left|\chi_1(\vec{x_1}|\theta_1),\chi_2(\vec{x_2}|\theta_2),\ldots,\chi_n(\vec{x_n}|\theta_n)\right\rangle, \tag{2.36}$$

where $\chi_i, i=1,\ldots,n$ denotes a chosen one-particle wavefunction with $(\vec{x_i}|\theta_i)$ being a set of spatial and spin coordinates $\vec{x_i}$ and θ_i, respectively.

The main idea behind HF method, is to utilize the variational principle

$$E_0\leq\frac{\langle\psi_T|\widehat{H}|\psi_T\rangle}{\langle\psi_T|\psi_T\rangle}, \tag{2.37}$$

which describes that the variational functional given by Equation (2.37) is always greater or equal to ground state energy E_0 depending on the parametrization of a trial wavefunction ψ_T, i.e. that ground state energy (and ground state wavefunction ψ_0) can be approximated via minimization of the variational functional with respect to ψ_T parameters.

Considering the normalization condition

$$\int\psi_T^*\psi_T\,d\vec{x}=1, \tag{2.38}$$

$$d\vec{x}=\prod_{i=1}^{n}d\vec{x_i} \tag{2.39}$$

and the fact, that spin-orbitals remain orthonormal, i.e.

$$\langle\chi_i|\chi_j\rangle=\delta_{ij}, \tag{2.40}$$

HF method aims approximate ground state energy like

$$E^{HF}\leq\min_{\vec{\chi_i}}\langle\psi_T|\widehat{H}|\psi_T\rangle. \tag{2.41}$$

Minimization of the variational functional with Born-Oppenheimer (BO) Hamiltonian leads to the system of equations

$$\widehat{f}(\vec{x_i})\chi_k(\vec{x_i})=\varepsilon_k\chi_k(\vec{x_i}), \tag{2.42}$$

i, k denoting indices of an electron and a spin-orbital, respectively [41, 44]. Considering ε_i coefficients, they approximate energies required for removal of one electron in spin-orbital

χ_k from the molecule [41]. The one-electron Fock operator

$$\widehat{f}\left(\vec{x_i}\right) = -\frac{1}{2}\nabla_i^2 - \sum_{A=1}^{M}\frac{Z_A}{r_{iA}} + v^{HF}\left(\vec{x_i}\right), \tag{2.43}$$

with

$$v^{HF}\left(\vec{x}_i\right) = \sum_j \int \frac{\left|\phi_j\left(\vec{r}'\right)\right|^2}{\left|\vec{r}-\vec{r}'\right|}\phi_i(\vec{r})\,\mathrm{d}\vec{r}' - \sum_j \delta_{\sigma_i,\sigma j}\int \frac{\phi_j^*\left(\vec{r}'\right)\phi_i\left(\vec{r}'\right)}{\left|\vec{r}-\vec{r}'\right|}\phi_j(\vec{r})\,\mathrm{d}\vec{r}' \tag{2.44}$$

representing the mean electronic potential of the i-th electron moving in the field of the remaining electrons in the molecule with θ_i denoting an i-th molecular orbital.

The first term of Equation (2.44) denotes the electrostatic repulsion of electron clouds, and is called *Hartree term*. The second "exchange" term denotes a sum over all pairs of orbitals with the same spin projection, and corresponds to the antisymmetry of the total wave function with respect to electron's exchanges [45]. The term enforces Pauli exclusion principle [46, 47], keeping the same-spin electrons apart, thus giving rise to, so-called, *Fermi hole* with a unit positive charge around electrons [48].

As the whole potential influencing i-th electron depends on the average motion of all other electrons, an iterative approach is adopted. The iterations are performed until self-consistency is achieved – inspiring another name for the method, talking about *self-consistent field*.

The HF method makes several significant simplifications, namely a) relying on the assumption, that every wavefunction can be sufficiently approximated utilizing only one SD, b) omitting relativistic effects completely and c) adopting "mean-field approximation", i.e. not accounting many-particle interaction precisely, omitting Coulomb interaction and strictly imposing HF inability to describe London dispersion [49].

That said, the HF solution in the limit of a complete basis set, i.e. the exact HF solution corresponds to E^{HF}. It follows straightforwardly, that, due to a variational property [50, 51] given by Equation (2.37), E^{HF} imposes an upper-bound to the exact ground-state energy E_0. Their difference

$$E_{\mathrm{corr}} = E^{HF} - E \tag{2.45}$$

is called *correlation energy*. It describes a difference between mean-field energy and an exact solution and despite being an important quantity in quantum chemistry (QC), its definition tends to be ambiguous over the available literature [52, 53, 54, 55] and not strictly limited to HF [56].

Due to the above-mentioned deficiencies, it is crucial to involve many-body interactions in the computation. Probably the simplest approach describing the many-body electronic effects is configuration interaction (CI). The core idea is the diagonalization of n-electron

Hamiltonian utilizing a basis of SDs or their linear combinations called configuration state functions (CSFs). The number of determinants possible to be constructed from a set of $2k$ one-electron spin-orbitals is $\binom{2k}{n}$ [41].

The complete many-electron basis set allows a full CI expansion

$$|\psi\rangle = c_0 |\psi_0\rangle + \sum_a \sum_r c_a^r |\psi_a^r\rangle + \sum_{a<b} \sum_{r<s} c_{ab}^{rs} |\psi_{ab}^{rs}\rangle + \sum_{a<b<c} \sum_{r<s<t} c_{abc}^{rst} |\psi_{abc}^{rst}\rangle + \cdots , \tag{2.46}$$

allowing to obtain energies of both the ground and excited states of the system, making it an exact solution *within a chosen basis set*.

Determinants present in the expansion are the ground state $|\Psi_0\rangle$ (usually HF reference), singly excited states $|\Psi_a^r\rangle$, doubly excited determinants $|\Psi_{ab}^{rs}\rangle$, triply excited determinants $|\Psi_{abc}^{rst}\rangle$, etc., up to n-tuply excited determinants. The wavefunction $|\psi\rangle$ is subsequently optimized with respect to the coefficients $c_0, c_a^r, c_{ab}^{rs}, c_{abc}^{rst}, \ldots$, to minimize the total energy expectation value.

Numerically, we can handle only a finite set of n-electron trial functions. Thus, we employ truncated configuration interaction expansions (TCIEs) to limit the number of trial functions. Truncated CI expansions provide an upper bound to exact solutions. For example, if single and double excitations are included, we have a configuration interaction singles and doubles (CISD) method. Disadvantages of truncated CI method are the lack of *size-extensivity* and *size-consistency*. The size-extensivity problem means incorrect scaling of E with the number of electrons [48, 57, 58]. The size-consistency problem, related to size-extensivity, denotes a lack of separability when a total energy of the composite system $E(A+B)$ with A and B fully separated is not equal to the sum of the energies for both isolated systems, i.e. the methods where $E(A+B) \neq E(A)+E(B)$ are not size-consistent [59]. There exist numerous corrective approaches to mitigate or fully remove both of these undesirable effects [60, 61, 62, 63, 64, 65, 66, 57, 67, 68, 69].

The optimal CISD expansion recovers some fraction of electronic correlations missing at the HF level and may therefore serve as a better approximation beyond HF. The CI natural orbitals (NOs) [70, 67, 71, 72] diagonalizing the first-order density matrix allow one to select only the most populated orbitals for subsequent calculations making their determinant expansions shorter [73] for higher-level theories. Subsequently, NOs-based expansions lead to faster convergence with respect to the corresponding canonical orbitals diagonalizing the Fock operator [74, 75, 76, 77, 78].

2.1.4 Multi-Configuration Calculations

One of the methods offering a compromise between accuracy and computational demands and their scaling with a possibility of being size-consistent is multi-configurational self-consistent field (MCSCF). It relies on the variational optimization of the expansion coefficients c_i (in CI-like fashion), simultaneously with the self-consistent field (SCF) improvement of orbitals in determinants Ψ_i in the sum

$$\left|\Psi^{MC-SCF}\right\rangle = \sum_i c_i \left|\Psi_i\right\rangle .$$

The sum has a truncated CI expansion form.

The computational effort is reduced by partitioning electrons to orbitals of interest (usually taken from previous HF, CISD, etc., calculations) into four groups according to their chemical importance:

1. The doubly-occupied *frozen orbitals* which are kept intact during the calculation (typically the group is empty or only the core orbitals are included),
2. The so-called *inactive orbitals* that are doubly-occupied and SCF optimized (inactive space), and
3. the orbitals allowed to be CI-like populated and SCF optimized simultaneously with a space 2. This space of orbitals is usually called *active space*.
4. The external orbitals (*virtual orbitals*) serve as a basis for mixing with occupied orbitals in variational SCF procedure.

The size-consistent behavior of the method is achieved by allowing the maximum order of excitation to be equal to the number of electrons in the group or the number of empty orbitals in the space 3 (priority lies with the larger number). Of relevance are all occupied valence orbitals that play role in the studied process (e.g. bond breaking or excitation) and all corresponding correlating unoccupied orbitals from the reference. This approach is known as complete-active-space self-consistent field (CASSCF) [79]. It allows one to study (at a qualitative level) larger systems compared to the high-level methods of quantum chemistry, but the combinatorial increase of the CPU time and memory requirements are still prohibitive. In CASSCF, relatively small active spaces are available, while in practical MCSCF studies, one must often restrict the active space and consider fewer electrons than should be considered and even lower the maximum allowed excitation leading to MCSCF which is not guaranteed to be size consistent. With a proper orbital selection based on chemical intuition, MCSCF results may be qualitatively correct and useful for interpretations. Larger CI/complete active space (CAS) spaces are now tractable by virtue of the density matrix renormalization

approaches [80, 81, 82, 83]. That said, CASSCF approach is a mean-field method in a sense a part of dynamical correlations could be missed. This can be partially compensated for via subsequent *perturbative treatment* [84, 85] or *Monte-Carlo approach* [86, 87].

One of the most prominent approaches adopted also in this thesis is the MRCI method [88, 89, 90, 91, 92, 93]. MRCI operates by a) initially constructing a space of reference configurations, b) exciting electrons out of these configurations, and c) solving TISE via minimization of the energy in the resulting configuration space. In its *uncontracted* variant, uncontracted MRCI (uc-MRCI), excitations are performed with respect to each individual reference configuration. Subsequently, many contraction schemes have been developed to cope with the increasing computational cost of uc-MRCI through a reduction of the number of relevant configurations, from which the most popular one is internally-contracted MRCI (ic-MRCI) [94, 95].

The MRCI method is relatively simple and, in its uncontracted form, the working equations are equivalent to single-reference CI (SRCI) with the exception that a larger set of configurations is considered. Thus, MRCI is very flexible, both in the choice of configuration space and the construction of the molecular orbitals, and can be applied to a variety of quantum systems. Due to the variational properties of MRCI, it follows, that wave function properties, such as energy gradients, dipole moments, etc. can be computed easily, especially when considering uc-MRCI. The main caveat of MRCI is its lack of size-extensivity whenever the CI expansion is truncated at a specific excitation level [88, 57, 96]. Thus, the system description deteriorates as the size of the molecule increases.

MRCI computations are generally performed by first constructing a space of reference configurations and subsequently specifying a fixed number of allowed excitations out of this *reference space*. The reference space is intended to cover non-dynamic electron correlation whereas the excitations out of it represent dynamic correlation [97, 98]. In the context of MRCI method, we recognize *virtual*, *active*, *reference (doubly-occupied)* and *frozen core* orbitals, as can be seen in Figure 2.3, with active and reference being sometimes denoted together as *internal* orbitals.

By default, the inner electron shells of the system, e.g., the 1s orbitals of the second row elements are considered frozen core orbitals. Sometimes more orbitals are considered frozen to decrease computational demands, a typical example being the "freezing" of all σ-electrons in a π-system [99]. The reference orbitals are doubly occupied in all reference configurations with excitation allowed when generating MRCI wave function. The active orbitals, on the other hand, possess various occupation patterns already in the reference configurations. Lastly, virtual orbitals are unoccupied in the reference configurations but are populated by one or two electrons during the MRCI procedure. It is also possible to freeze the virtual orbitals and, thus, effectively remove them from the computation. As a consequence, they do not affect the result at all.

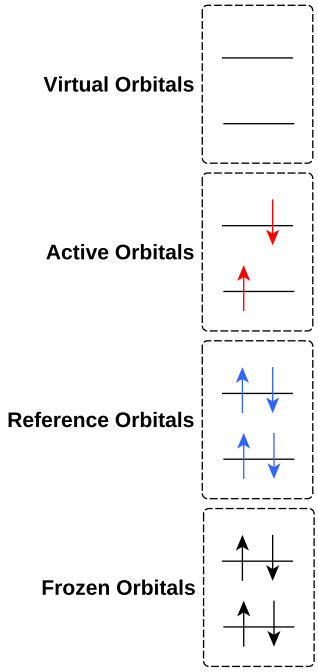

Figure 2.3: Classification of molecular orbitals in MRCI

At the heart of the MRCI computation is the reference space constructed by exciting electrons within the active orbital space. It is common to construct the reference space as a complete active space, i.e., by allowing all possible occupations within the active orbital space, on top of the CASSCF wave function. Alternatively, occupation restrictions can be imposed to reduce the size of the reference space and ultimately the configuration space, thus decreasing the computational cost. With the reference space set up, MRCI wave function is defined by exciting electrons out of this space.

The frequently adopted type is uc-MRCI singles and doubles (uc-MRCISD) where excitations are performed with respect to the individual reference configurations and up to two excitations are allowed. This leads to various singly excited configurations, namely excitations from reference to active orbitals, from active to virtual orbitals, and directly from the reference to virtual orbitals. The excitations from active to active orbitals only become relevant with incomplete reference spaces. Secondly, considering doubly excited configurations, any combination of the above-mentioned excitation types is possible.

Considering MRCI singles and doubles (MRCISD), a general wavefunction is of the form

$$|\psi\rangle = \sum_{k=1}^{n_r} c^r \, |\phi_k^r\rangle + \sum_l c_l^s \, |\phi_l^s\rangle + \sum_m c_m^d \, |\phi_m^d\rangle \,, \tag{2.47}$$

with $|\phi_k^r\rangle$, $|\phi_l^s\rangle$ and $|\phi_m^d\rangle$ denoting reference, singly- and doubly-excited configurations, respectively. In contrast with SRCI where only excitations from occupied to virtual orbitals are

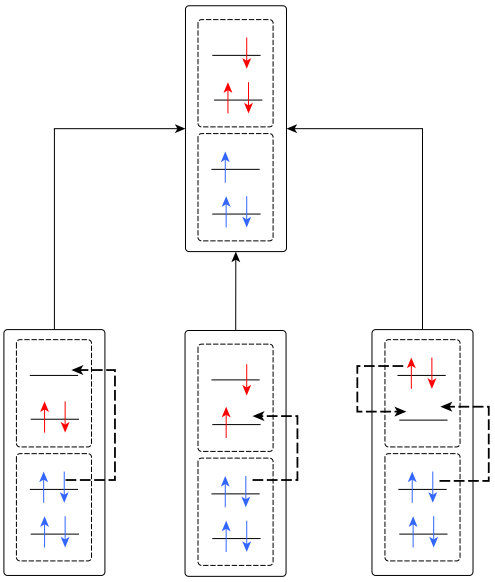

Figure 2.4: Three (redundant) ways to obtain a singly-excited state from different reference configurations

considered, a larger number of orbital spaces MRCI allows for problems with configuration redundancy to arise as multiple excitations can lead to the same excited configuration as can be seen in Figure 2.4.

Eventually, MRCI wavefunction given by Equation (2.47) is used in Equation (2.37) and optimized with respect to its parameters. For clarity, a full basic MRCI workflow is described by Figure 2.5.

2.1.5 Charge Density

From a measurement point of view, electrons do not possess a precise position due to Heisenberg's uncertainty principle [100]. Thus, the charge is also not localized in discrete points, but acts as a continuous distribution. If we consider the i-th molecular orbital (MO) wavefunction $\psi_{MO,i}$ in the form of linear combination of atomic orbitals (LCAO)

$$\psi_{MO,i} = \sum_{j=1}^{n_b} c_{ij}\phi_j, \tag{2.48}$$

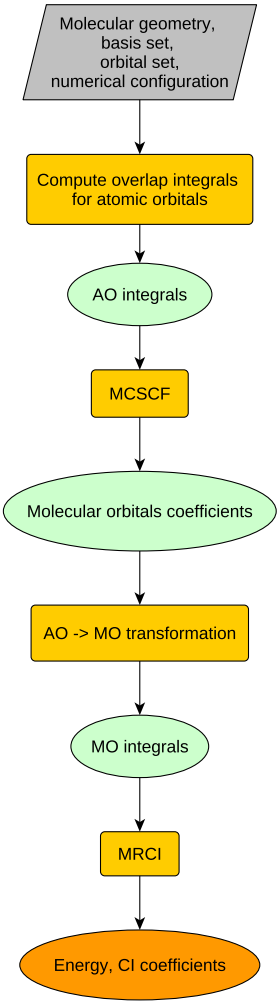

Figure 2.5: MRCI workflow

with atomic orbitals ϕ_j denoting a normalized j-th function of the chosen basis set(e.g. [101, 102, 103]) and n_b denoting the number of basis set functions, the charge density can be described as

$$\rho_{i,q}(\vec{r}_i) = q\,|\psi_i(\vec{r}_i)|^2 \tag{2.49}$$

$$= q\sum_{j=1}^{n_b}\sum_{k=1}^{n_b} c_{ij}c_{ik}\phi_j^*(\vec{r}_i)\phi_k(\vec{r}_i), \tag{2.50}$$

where q denotes charge of a particle – i.e. $q = 1$ considering atomic units. Thus, considering the total charge density in atomic units

$$\rho(\vec{r}) = \sum_{i=1}^{N} |\psi_i(\vec{r}_i)|^2\,, \tag{2.51}$$

with N denoting the number of MOs, the integral over the whole 3D (Cartesian) coordinate space D can be obtained as

$$\int_D |\psi(\vec{r})|^2 \, d^3r, \tag{2.52}$$

with d^3r representing an appropriate integration measure over the space D.

Considering the importance of knowledge of atomic charges in a molecule, numerous methods were invented to compute it utilizing the abovementioned knowledge of charge density. The historically most prominent one is certainly Mulliken population analysis [104, 105], being accompanied by other methods, compensating for some of its deficiencies, like like Löwdin's approach [106] or Natural population analysis [107]. Also, it is possible to obtain atomic charges utilizing electron density, which is subsequently integrated over, in contrast to the previous method based on assembling a density matrix. Representatives of this second group are Hirshfeld's method [108] or the approach based on the Atoms-in-Molecules approach [109, 110].

2.1.6 Interstate Transitions

Transition dipole moment $\vec{\mu}_{1,2}$ is an electric dipole moment corresponding to the transition between two electronic states $|\psi_1\rangle$ and $|\psi_2\rangle$ given by

$$\vec{\mu}_{1,2} = \langle\psi_2|\vec{\mu}|\psi_1\rangle = \int \psi_2^* \vec{\mu} \psi_1 \;\; d\tau, \tag{2.53}$$

with the *dipole moment operator*

$$\vec{\mu} = \sum_{i=0}^{n} q_i \vec{x}_i, \tag{2.54}$$

defined here for n particles, q_i and $\vec{x}_i$ being the i-th particle charge and its position operator, respectively [111, 112, 113]. Also, $d\tau$ denotes integration over a whole adopted domain, i.e. the same as $dx\,dy\,dz$ in three-dimensional space. That said, according to Szabó and Gustaffson [114], $\vec{\mu}_{i,j}$ can be used to predict a probability of the *spontaneous emission*, i.e. a non-stimulated (except for vacuum fluctuation) radiative transition from the state $|\psi_i\rangle$ to the state $|\psi_2\rangle$ in a specific time-step t like

$$P_{i,j}(t) = \frac{4\omega_{i,j}^3(t)}{3\hbar c^3} \Delta t (N_{ph} + 1) |\vec{\mu}_{i,j}(t)|^2 \tag{2.55}$$

$$\omega_{i,j}(t) = \frac{max(0, V_i(t) - V_j(t))}{\hbar}, \tag{2.56}$$

where N_{ph} is a number of photons in the radiation field, and $\omega_{i,j}$, being the difference of electronic energies divided by $\hbar$ of the involved PESs, denotes the frequency of the emitted

photon.

Such a case of spontaneous emission is illustrated in Figure 2.6, where an electronic subsystem transitions to a lower state by radiating an amount of energy as a photon.

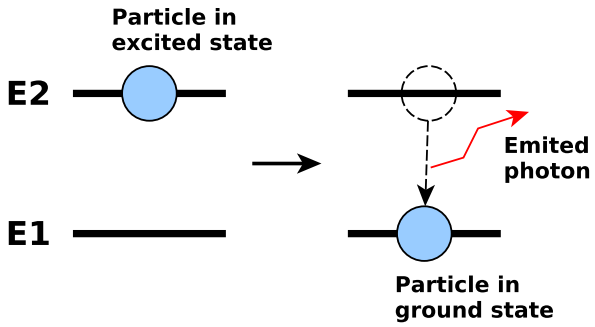

Figure 2.6: Spontaneous emission of photon

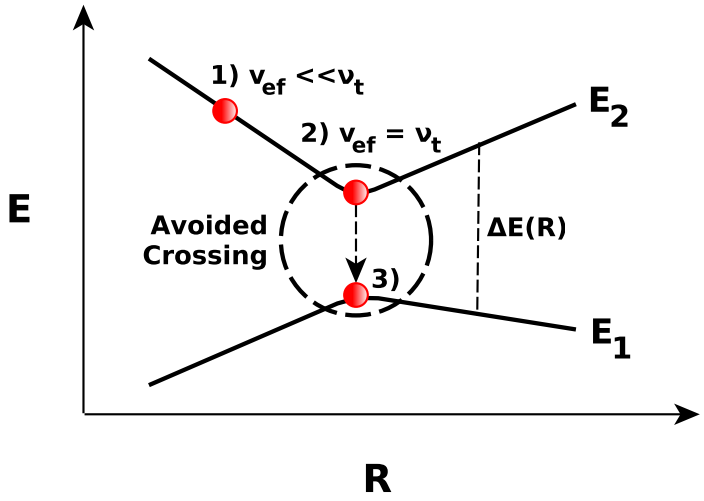

Figure 2.7: Non-radiative transition of electron

Using BOA the coupling between electrons and nuclei is neglected, i.e. electrons are assumed to move infinitely fast and adapt to the electric field from the nuclei with no time delay, as mentioned beforehand. In such a case, the *transition frequency* ν_t is much greater than the rate of a change of a nuclei electric field v_{ef}. However, if $v_{ef} = \nu_f$ and an energy difference between PESs is not too large, electron-nuclei coupling is not negligible anymore and a non-radiative transfer can occur as can be seen in Figure 2.7. This transition is called the non-adiabatic transition and the mediating electron-nuclei interaction non-adiabatic coupling (NAC) [115, 116, 117]. The non-radiative transition probability was described by Desouter-

Lecomte and Lorquet [118] as

$$P_{i,j} = e^{-(p/4)\xi} \tag{2.57}$$

$$\xi = \frac{\Delta E(\vec{q})}{\hbar|\frac{\partial}{\partial t}\vec{q}||\lambda_{i,j}(\vec{q})|}, \tag{2.58}$$

where ΔE is the energy difference between two PESs and $\frac{\partial}{\partial t}\vec{q}$ a time derivative of a nuclear displacement vector parallel to the non-adiabatic coupling $\vec{\lambda_{i,j}}$ given by

$$\vec{\lambda_{i,j}} = \langle\phi_i|\frac{\partial}{\partial\vec{q}}|\phi_j\rangle\,. \tag{2.59}$$

From Equation (2.57), it can be seen that the non-radiative transition probability increases with decreasing energy difference between the two involved PESs.

2.1.7 Molecular Symmetry

Molecular symmetry plays an important role in determining molecule properties, e.g. in recognizing of allowed electronic transitions [119, 120, 121] or prediction of a non-zero dipole moment [122, 123, 124] and/or higher multipoles. For these properties to be efficiently exploited, they are described formally utilizing group theory in a subfield called *representation theory* [125, 126, 127, 128].

In this context, the relevant group is constructed upon a set of *symmetry operators*, i.e. actions that leave an object looking the same after they have been carried out. The symmetry operators considered here are the identity operator $\widehat{I}$, rotation operator $\widehat{C}_\alpha$, improper rotation operator $\widehat{S}_\alpha$, the inversion operator $\widehat{i}$ and reflection operator σ_β, with α denoting, that if the molecule is rotated by $360°/\alpha$ around an axis it preserves its symmetry, the improper rotation meaning combination of subsequent rotation and reflection via a mirror plane perpendicular to the rotation axis and β being the mirror plane type, where planes intersecting a rotation axis are denoted as σ_v, while the planes perpendicular to it σ_h. All the operators corresponding to the point $\overrightarrow{x} = [x, y, z]^T$ in 3-D space are described by matrices given by Equations (2.60) to (2.64). Considering, that there is always at least one point left "untouched" by these operators, we call groups consisting solely of them *symmetry point groups*. With that said, Hermann-Mauguin, Shubnikov, or Schoenflies notation is usually adopted to denote the relevant point groups, the first one being preferred in crystallography, while the third one behind the standard in spectroscopy-related fields [129, 130, 131]. Due to this thesis being oriented at theoretical spectroscopy, solely Schoenflies notation is used from now on.

$$\widehat{I} = \begin{bmatrix} 1 & 0 & 0 \\ 0 & 1 & 0 \\ 0 & 0 & 1 \end{bmatrix} \tag{2.60}$$

$$\widehat{i} = \begin{bmatrix} -1 & 0 & 0 \\ 0 & -1 & 0 \\ 0 & 0 & -1 \end{bmatrix} \tag{2.61}$$

$$\widehat{S}_\alpha = \begin{bmatrix} \cos\theta & -\sin\theta & 0 \\ \sin\theta & \cos\theta & 0 \\ 0 & 0 & -1 \end{bmatrix} \tag{2.62}$$

$$\widehat{\sigma}_{xy} = \begin{bmatrix} 1 & 0 & 0 \\ 0 & 1 & 0 \\ 0 & 0 & -1 \end{bmatrix} \tag{2.63}$$

$$\widehat{C}_\alpha = \begin{bmatrix} \cos\theta & -\sin\theta & 0 \\ \sin\theta & \cos\theta & 0 \\ 0 & 0 & 1 \end{bmatrix} \tag{2.64}$$

Considering the symmetry operators (matrices), their sets, denoting a specific behavior of an observed object with respect to the relevant symmetry operations, are called a *symmetry representation*. These can be further categorized as reducible and irreducible, the former being linear combinations of the latter, which can be obtained from the reducible ones utilizing known reduction rules [125]. Both types of representation can be illustrated via *character table*, where instead of operators themselves only their *characters* are listed, as can be seen in Table 2.1. The characters, in this context, represent traces of the matrix operators given as

$$Tr(A) = \sum_i \sum_i A(i,i), \tag{2.65}$$

with i denoting the (common) rank of the symmetry matrices as the symmetry matrices are square. Furthermore, from Table 2.1 it can be seen, that the irreducible representations A_1, A_2, B_1 and B_2 give rise to the reducible representation Γ as $\Gamma = A_1 + B_2$.

C_{2v}	E	C_2	σ_{xz}	σ_{yz}
A_1	1	1	1	1
A_2	1	1	-1	-1
B_1	1	-1	1	-1
B_2	1	-1	-1	1
Γ	2	0	0	2

Table 2.1: Table of C_{2v} point group with a reducible representation Γ.

2.2 Dynamics

MDSs is used to analyze the physical motion of nuclei involved in the inspected process. With the advantage of only needing computational resources instead of laboratory equipment, it allows for long periods of interactions and subsequent observations than would be practical otherwise. MDSs were performed in this thesis on the ground-state PES of N_2^+/He adopting

a hybrid approach, i.e., treating atomic nuclei in a classical manner and electrons quantum-mechanically, according to the equations

$$\dot{c}_\alpha = -\frac{i}{\hbar} E_\alpha c_\alpha - \sum_\beta \sigma_{\alpha\beta} c_\beta, \tag{2.66}$$

$$\dot{\overrightarrow{r}}_k = \frac{\overrightarrow{p}_k}{m_k}, \tag{2.67}$$

$$\dot{\overrightarrow{p}}_k = \overrightarrow{F}_k, \tag{2.68}$$

where

$$\sigma_{\alpha\beta} = \sum_k \overrightarrow{\lambda}^{(k)}_{\alpha\beta} \dot{\overrightarrow{r}}_k, \tag{2.69}$$

$$\overrightarrow{F}_k = -\sum_\alpha |c_\alpha|^2 \nabla_k E_\alpha - \sum_{\alpha\neq\beta} c^*_\beta c_\alpha \left(E_\beta - E_\alpha\right) \overrightarrow{\lambda}^{(k)}_{\alpha\beta}, \tag{2.70}$$

$$\overrightarrow{\lambda}^{(k)}_{\alpha\beta} = \langle \phi_\beta | \nabla_k \phi_\alpha \rangle \,, \tag{2.71}$$

where the total electronic wave function of the collision complex given by $\psi = \sum_i c_i \phi_i$ is the solution of the corresponding Schrödinger equation with c_i being a probability amplitude, i.e. $|c_i|^2$ denotes the probability of the system is in state $|i\rangle$ and ϕ_i being the wave function of a state $|i\rangle$ with the sum running over all possible adiabatic electronic states. $\overrightarrow{r}_k$ denotes the vector of a k-th particle position, $\dot{\overrightarrow{r}}_k$ then stands for the velocity of k-th particle, $\overrightarrow{p}_k$ its linear momentum, and m_k its mass. Furthermore, E_α is a potential energy of a system in state $|\alpha\rangle$ and $\overrightarrow{\lambda}^{(k)}_{\alpha\beta}$ a vector of nonadiabatic coupling projected on atom k. These quantities will serve as an input to subsequent dynamical calculations and obtaining them is the main focus of this project as a whole.

The quasi-classical trajectory (QCT) approach [132, 133, 134] has been adopted to obtain sets of trajectories to be further utilized in calculations of collision cross-sections. Every trajectory is then evolved numerically until a termination criterion is met.

QCT pass vibrational energy into each mode in the initial step, thus improving the results of solely classical simulations, e.g. considering the calculations of photoelectron [135] or infrared spectra [136]. Improvements include the better agreement of spectral linewidths with experiments at lower temperatures and better agreement of vibrational frequencies with anharmonic calculations.

The improvements at lower temperatures can be explained by the fact, that there is nuclear motion due to zero-point motion. This fact is inherently involved in the quasi-classical initial velocities, leading to finite peak widths even at low temperatures. That is in sharp contrast with classical simulations, which yield zero peak widths in the low-temperature limit as the thermal kinetic energy vanishes with decreasing temperature. At room temperature, the

quantum vibrational energy for high-frequency modes tends to become much larger than the classical kinetic energy. Thus, at QCT regions of PES higher in energy are usually sampled as they are more anharmonic in contrast with the low-energy regions accessible to classical simulations. These two effects lead to improvements in peak widths and a more realistic sampling of the anharmonic parts of PES.

On the other hand, there are several limitations to the approach. The first one is connected to the so-called "kinetic energy spilling" problem [137], i.e. a possibility of an artificial transfer of kinetic energy among modes. This is allowed to happen due to the fact, that the initial velocities are being chosen according to quantum energy levels, which are usually much higher than the energy levels of corresponding classical systems. Moreover, the classical equations of motion (EOMs) also allow for the transfer of non-integer multiples of the zero-point energy among modes, thus leading to a change in selection rules for the transfer of kinetic energy. The second problem is that QCT is based on classical Newtonian dynamics, which means that the adopted probability distribution at low temperatures is not so reliable, i.e. can be incorrect compared to the true quantum distribution [135].

In this way, the coordinates of the colliding particles and their momenta were obtained to be used in subsequent cross-section evaluations. The numerical configuration of MDS as used in this thesis is described in detail in the following section.

A cross-section is a quantity tightly bound to a probability of some observed phenomena happening, typically in context with different types of physical interactions occurring, e.g. interaction of an alpha particle with an atomic nucleus being quantified via Rutherford cross-section [138, 139]. Simplistically said, a cross-section can be imagined as an effective geometric area around some particle, allowing the investigated reaction to occur, if hit by another interacting particle. Importantly, even if the cross-section has the same units as the area, it does not generally correspond to the actual physical size of the target given by other forms of measurement. This thesis is focused on cross-sections of two reactions dominant collisions of N_2^+ with He atoms – *non-reactive scattering* (NRS) and momentum-transfer (MT).

Specifying a cross-section as the differential limit of a function of some final-state variable, e.g. particle angle, is called a *differential cross section*, illustrated by Figure 2.8.

Subsequently, integrating over all possible "scattering-angles" (or other relevant variables) we obtain the *total cross-section*.

Considering the collision complex $[N_2/He]^+$, NRS, given by

$$N_2^+ + He \rightarrow N_2^+ + He, \tag{2.72}$$

and the *collision-induced dissociation* (CID) of the N_2^+ ion, given by

$$N_2^+ + He \rightarrow N^+ + N + He, \tag{2.73}$$

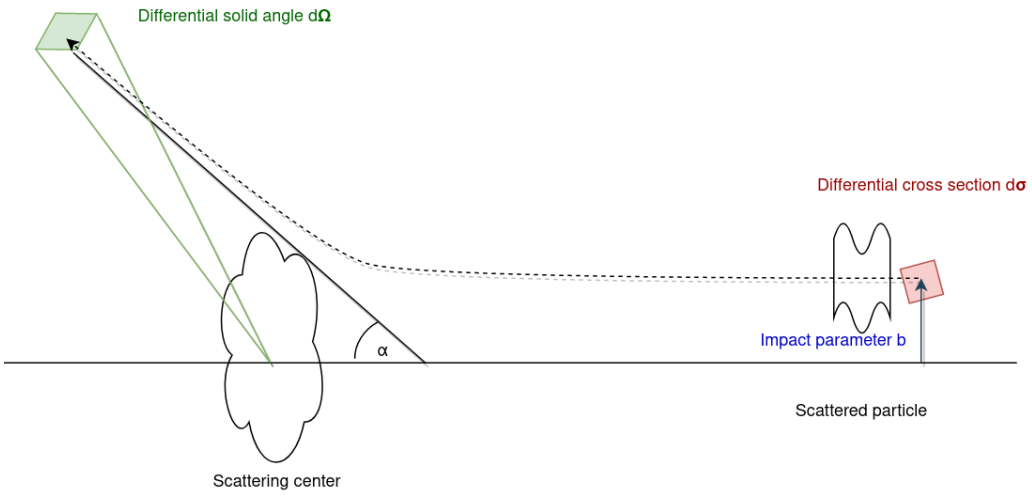

Figure 2.8: Differential cross section

are of interest in this work. The basic quantity used to quantitatively describe these collision processes is then differential cross-section, $\mathrm{d}\sigma/\mathrm{d}\Omega$.

However, the differential cross-section of the former process cannot be directly used since, within the classical approach, the differential cross-section of the NRS process has a non-integrable singularity at the zero deflection angle and, thus, the corresponding integral cross-section diverges as NRS involves the elastic scattering channel which, at the classical limit, possesses an infinite integral cross-section. Subsequently, the same holds for NRS channel itself. To deal with this problem, approximate cross-sections calculated at the momentum-transfer approximation level [140], momentum-transfer cross-sections (MTCSs), are used. Following our previous studies [141], two types of MTCSs have been considered,

$$\sigma_{\mathrm{NRS}}^{(\mathrm{MT1})} = \int_{4\pi} \left[\frac{\mathrm{d}\sigma}{\mathrm{d}\Omega}\right]_{\mathrm{NRS}} (1-\cos\theta)\,\mathrm{d}\Omega, \tag{2.74}$$

$$\sigma_{\mathrm{NRS}}^{(\mathrm{MT2})} = \int_{4\pi} \left[\frac{\mathrm{d}\sigma}{\mathrm{d}\Omega}\right]_{\mathrm{NRS}} \left(1-\frac{p'}{p}\cos\theta\right)\mathrm{d}\Omega, \tag{2.75}$$

with θ being the scattering angle, p and p' the magnitudes of the linear momentum of the He atom before and after the collision, respectively, and $[\mathrm{d}\sigma/\mathrm{d}\Omega]_{\mathrm{NRS}}$ the differential cross-section of NRS. Hereafter, we will denote the two types of cross-sections as type 1 MTCS (MTCS1) in the case of Equation (2.74) and type 2 MTCS (MTCS2) for Equation (2.75). The cosine terms in integrals on the right-hand side of Equation (2.74) and Equation (2.75) suppresses the divergence of the differential cross-section at $\theta \to 0$ and the resulting MTCSs are finite. The adoption of the momentum-transfer approximation introduces only a negligible error [142]. That said, MTCS1 was originally introduced for elastic scattering while MTCS2 represents a generalized version presumably better describing non-elastic processes with a transfer of en-

ergy between translational and internal degrees of freedom. Both approaches were successfully tested in a series of previous calculations on rare-gas-based collision complexes [143] [144].

For the CID process, a process with a non-zero energetic threshold, such problems do not arise, thus a standard integral cross-section,

$$\sigma_{\mathrm{CID}}^{(\mathrm{int})} = \int_{4\pi} \left[\frac{\mathrm{d}\sigma}{\mathrm{d}\Omega}\right]_{\mathrm{CID}} \mathrm{d}\Omega, \tag{2.76}$$

may be used even at the classical level.

2.3 Transport Properties

One of the main goals of the research the present thesis is part of was obtaining a detailed theoretical framework spanning the route from intermolecular interactions, through dynamics to mesoscopic modelings. With the necessary above-mentioned inputs, the mesoscopic models provide information about molecular transport properties, specifically *dissociation rate constants*, longitude and transverse *diffusion coefficients* and *ionic mobility*.

Dissociation reaction

$$A_x B_x \Rightarrow xA + yB \tag{2.77}$$

gives rise to a dissociation rate constant defined as

$$K_D = \frac{[A]^x [B]^y}{[A_x B_y]}, \tag{2.78}$$

where $[A]$, $[B]$, $[A_x B_y]$ denote equilibrium concentrations of reactants A, B and the complex $A_x B_y$, respectively. K_D then measures a tendency of a complex to reversibly dissociate into smaller components, e.g. separate molecules [145].

Talking about diffusion, Fick's first law

$$J = -D\frac{d\varphi}{dx}, \tag{2.79}$$

where J, D, φ, and x denote the diffusion flux, diffusion coefficient, concentration, and position, respectively, predicts, that the diffusion flux J always goes from regions of high concentration to regions with low concentration – the effect directly proportional to the concentration gradient [146]. That said, it is important to also address the character of diffusion with respect to its "directions" – i.e. the direction of the mean flow and the direction perpendicular to it with the former being denoted as longitudinal diffusion [147] and the latter as transverse diffusion [148], which denomination is also used with their respective diffusion coefficients.

Finally, ionic mobility μ is described as an ability of a charged particle to move through a medium under the influence of a force field, being pulled by the force, with electrical ion

mobility being our concern in this thesis. Assuming, that the ion moves in a carrier gas, while the motion is induced by a uniform electric field until it reaches a constant drift velocity defined v_d as

$$v_d = \mu E, \tag{2.80}$$

where E denotes the magnitude of the applied electric field.

Chapter 3

Computational Approach

In this section, the computational details are described in a detailed manner, to explain the choices made in the numerical realization of the results and also to allow their full reproduction, starting with properties of ab initio computations and going over ways to represent PESs, both via the analytical models and ANNs. The computational environment is presented, describing the utilized computational cluster in whole detail, together with the adopted parallelization approach.

3.1 Quantum Chemistry

Numerical properties of ab initio computations of molecular interactions are described here, containing details for computations of N_2, N_2^+ , and N_2^+/He . The section begins with the introduction of the most common quantum chemistry software packages, continuing with the justification of our numerical settings for all the considered molecules.

3.1.1 Available Implementations

There exist many different implementations of quantum chemistry methods. They usually offer not-only HF method, but also post-HF methods (CI...), multi-configuration (MCSCF) and multi-reference methods (MRCI), density functional theory [149, 150, 151, 152] or different perturbation-theory-based methods [153, 154, 155].

The well-known examples of software available for free are Dalton [156], Dirac [157], NWChem [158] or PSI [159]. On the other hand, the commercial software examples are, e.g., Gaussian [160], Q-Chem [161], Turbomole [162] or MOLPRO [163, 164, 165] with the last being used in this dissertation project.

MOLPRO is a comprehensive system of many ab initio solvers for electronic structure calculations, originally developed by H. J. Werner and P. J. Knowles with many later contributors. It consists of programs for "standard" computational chemistry problems, which

are often parallelized in a hybrid manner, on distributed level (via MPI [166]), threading level (via OpenMP [167]) to the vectorization of elementary numerical operations. While many methods are implemented in MOLPRO, mainly MCSCF [168, 169, 170] and MRCI [171, 172, 173] were utilized in this thesis, with details of computations described later in this section.

3.1.2 N_2 & N_2^+ Specific Settings

Detailed research of the N_2^+ electronic structure calculations and their convergence has been performed since the ion represents, with respect to *ab initio* calculations, the most computationally difficult part of the N_2^+/He complex. For the electronic states of the N_2^+ ion considered in this work, $X^2\Sigma_g^+$ and $A^2\Pi_u$, the same numerical settings and computational schemes have been adopted with some steps performed to considerably improve the convergence of calculations. As the first step, a *restricted Hartree-Fock* (RHF) calculation is run for the N_2 molecule. Then, the state-specific calculations are performed for the N_2^+ ion using a MCSCF method. Finally, the preceding calculations are made more precise, using a MRCI method, as an input.

With N_2^+ ion being a linear molecule, its symmetry is naturally described by the $D_{\infty h}$ point group. Considering that only Abelian groups are included in the MOLPRO package, the D_{2h} point group, the largest Abelian subgroup of $D_{\infty h}$, has been used for this ion. This subgroup has eight irreducible representations, A_g, B_{3u}, B_{2u}, B_{1g}, B_{1u}, B_{2g}, B_{3g}, and A_u, which are used in this work to represent the symmetry of the N_2^+ electronic states instead of the commonly used MOs notation.

The calculations were performed utilizing different augmented correlation-consistent basis sets of Dunning et al. [174] from triple through sextuple zeta cardinality, i.e. aug-cc-pVTZ (AVTZ), aug-cc-pVQZ (AVQZ), aug-cc-pV5Z (AV5Z), and aug-cc-pV6Z (AV6Z).

The dependency of *potential energy curve*s (PECs) on orbital spaces (OSs) has been investigated for the following cases: a) orbital space 1 (OS1) containing the minimal OS of N_2^+ (comprising MOs $1a_g$, $1b_{1u}$, $2a_g$, $2b_{1u}$, $1b_{3u}$, $1b_{2u}$, $3a_g$, $1b_{2g}$, $1b_{3g}$, and $3b_{1u}$)[1] augmented, with a b_{3u} MO (as recommended in [175]), b) orbital space 2 (OS2) consisting of the minimal OS augmented with two more MOs resulting from 3s atomic orbitals (AOs) of N_2 atom ($4a_g$ and $4b_{1u}$), c) orbital space 3 (OS3) containing the minimal OS augmented with the two MOs resulting from 3s AOs ($4a_g$ and $4b_{1u}$) and with two more bonding MOs resulting from $3p_{x,y}$ AOs ($2b_{3u}$ and $2b_{2u}$), and d) the most extensive orbital space 4 (OS4) with the minimal OS augmented with all the MOs resulting from all the 3s and 3p AOs of N_2 atom ($4a_g$, $4b_{1u}$, $2b_{3u}$, $2b_{2u}$, $5a_g$, $2b_{2g}$, $2b_{3g}$, and $5b_{1u}$)[2]. The lowest MOs ($1a_g$ and $1b_{1u}$) have been treated as "closed" in MCSCF calculations, i.e., always doubly occupied, and as "core" orbitals in MRCI calculations, i.e., doubly occupied and with their electrons not involved in excitations, as described in Section 2.1.4.

[1] $1\sigma_g$, $1\sigma_u$, $2\sigma_g$, $2\sigma_u$, $1\pi_x$, $1\pi_y$, $1\sigma_z$, $1\pi_x^*$, $1\pi_y^*$, $1\sigma_z^*$, and $2\pi_x$ in the standard MO notation, respectively.
[2] $3\sigma_g$, $3\sigma_u$, $2\pi_x$, $2\pi_y$, $2\sigma_z$, $2\pi_x^*$, $2\pi_y^*$, $2\sigma_z^*$

Internuclear distances were organized in a grid covering a range of $r = 0.7{-}15\,\text{Å}$ with a step of $\delta r = 0.01\,\text{Å}$ at short and medium distances (up to $r = 5\,\text{Å}$) and $\Delta r = 0.1\,\text{Å}$ in the long-distance region (up to $r = 15\,\text{Å}$). The dissociation distance, i.e. the infinite separation of the two nitrogen atoms, has been approximated via internuclear distances of $r = 20, 50, 100\,\text{Å}$.

Importantly, the spin-orbit coupling is not considered in this thesis, as it is insignificant compared to the accuracy achieved here for the N_2^+ (e.g., the spin-orbit splitting is of the order of $10\,\text{cm}^{-1}$ to $100\,\text{cm}^{-1}$ in N and N^+ [176]) and is completely out of the game in He.

A smooth representation of calculated points has been created, for each discrete PEC, for subsequent spectroscopic analysis. That said, the grids of the equilibrium distance in the N_2^+ ion, r_e, the ion binding energy, D_e, and its harmonic vibration frequency, ω_e, have been calculated while approximated via cubic spline in a small neighborhood of the presumed PEC minimum. In each case, the point with the lowest energy and eight more points around it have been used to get the PEC cubic representation via a least squares fit.

Further, fully anharmonic vibrational energies have been calculated using a broader analytic representation of discrete PECs as implemented in the LEVEL16 software package [177]. Note that the cubic splines have been applied to $r^2V(r)$ rather than to $V(r)$ itself on the repulsion wall to get a more stable numerical behavior. The three points corresponding to the three largest distances considered ($r = 20, 50, 100\,\text{Å}$) have been used to adjust the long-range part of the potentials approximated as

$$V_\text{LR}(r) = V_\text{asymp} - \sum_{n=0}^{1} c_n / r^{4+2n}. \tag{3.1}$$

This potential was also used for solving the rotational-vibrational Schrödinger equation for N_2^+.

3.1.3 N_2^+/He Specific Settings

Similar calculations were also performed for the N_2^+/He complex. Considering the increased computational demands, as compared to N_2^+, the calculations were less extensive. Also, as already mentioned above, the methodologically most involved part of the N_2^+/He complex is the inherently multi-configuration N_2^+ ion, and no dramatic change is expected in the problem complexity upon adding the helium atom until charge transfer between nitrogen and helium becomes important and, subsequently, highly excited electronic states come into play. That said, the ionization potential of the helium atom is by about 10 eV higher than that of N_2, and the charge transfer between N_2^+ and He requires electronically highly excited N_2^+ ions. Thus, only a specific OS and a chosen basis set have been considered in the N_2^+/He case. The particular choice was made with respect to prospective dynamical calculations as a trade-off between computational demands and results' accuracy.

In correspondence with the N_2^+ calculations, the three lowest electronic states of the N_2^+/He complex were considered, which asymptotically correlate to the $X^2\Sigma_g$ state and (doubly degenerate) $A^2\Pi_u$ state of the isolated N_2^+ ion. For the planar N_2^+/He complex, irreducible representations of the C_s group have been used to classify the electronic states of N_2^+/He, A' and A''. The N_2^+/He ground state, possessing the A' symmetry, asymptotically correlates to the $X^2\Sigma_g$ state of N_2^+, the first excited state of the A' symmetry and the lowest state of the A'' symmetry correspond to the doubly degenerate $A^2\Pi_u$ state of N_2^+.

An OS containing eleven a' MOs and two more a'' MOs has been used in the case of N_2^+/He calculations. It corresponds to OS2 introduced in the preceding subsection for the N_2^+ ion with a 1s orbital added for He atom. With the prospective dynamical calculations, their computational cost and desired accuracy in mind, aug-cc-pVQZ(spdf) (AVQZ′) basis set has been used with only the *spdf* functions considered and the *g* functions omitted.

As N_2^+/He complex computations possess some inherent numerical difficulties, they were performed in a sequence of steps intended to mitigate them, beginning with an RHF calculation of the (neutral) N_2He complex with the minimal OS. Subsequently, either a state-specific MCSCF calculation has been performed for the N_2^+/He in the case of the ground state calculation, or a three-state-averaged ($2\times A'+1\times A''$) MCSCF calculation for the first point followed by a series of two-state-averaged computations for the other points (in the case of the $2A'$ calculations) or state-specific calculations (in the case of $1A''$ calculations) with the wave function ansatz always taken from a preceding step. The adopted scheme of calculations proved to be crucial for achieving an overall convergence in both the MCSCF method and its MRCI refinement, where points were computed separately due to runtime demands, taking the wave function ansatz from the MCSCF step. That said, if the $2\times A'+1\times A''$ step were to be omitted, major convergence issues often emerge in MRCI level.

Talking about the angle between the N_2^+ axis and the line connecting the He atom with the center-of-mass of the N_2^+ ion, a dense grid of its values were considered in order to reliably capture the anisotropy of the N_2^+/He PES, $\theta \in [0°, 90°]$ with $\Delta\theta = 15°$, and a broad range and a grid of internal distances, i.e. the distances between the two N atoms, r, and the distance between the He atom and the center-of-mass of the N_2^+ ion, R, were used, $r = 0.7{-}5\,\text{Å}$ and $R = 0.7{-}5\,\text{Å}$ with $\Delta r = 0.1\,\text{Å}$ and $\Delta R = 0.1\,\text{Å}$, to get an extended and sufficiently detailed representations of the N_2^+/He PESs. In addition, asymptotic values of $r = 100\,\text{Å}$ and $R = 100\,\text{Å}$ were added to assess the dissociation energy. Continuous smooth representations of selected 1D and 2D cuts through the three N_2^+/He PESs considered in this work were obtained approximately using 1D and 2D cubic splines, respectively, as implemented in the MATLAB software package [178].

3.2 Representation of Potential Energy Surfaces

As already stated, the following molecular dynamics simulations will be using continuous and accurate representations of a PES. They are useful so that it is not necessary to perform the calculations "on the fly" – i.e. run ab initio methods every time new energy is necessary, for the new geometry.

The disadvantage of utilizing interpolation techniques is that they are highly sensitive to the density of the grid computed beforehand, so, in a realistic scenario, artificial oscillations would appear on the resulting PES representation in the regions where the density of grid nodes is too low. A situation like that sometimes occurs with the grid computed both by aforementioned ab initio methods and a discrete-time Monte Carlo methods [179, 180], due to possible convergence problems in the former case and a stochastic aspect of the latter one. Thus, another two approaches can be adopted – the usage of analytical models and machine-learning-based models.

3.2.1 Analytical Models

To achieve the desired smoothness, analytical functions based on physical approximations were introduced and used both in a general manner [181] and in special cases of physical systems like classical force fields [182]. One of the most well-known and simplest examples is Lennard-Jones potential [183] given by

$$V_{LJ} = 4\epsilon \left[\left(\frac{\sigma}{r} \right)^{12} - \left(\frac{\sigma}{r} \right)^{6} \right], \tag{3.2}$$

where r, ϵ and σ denote an internuclear distance between two particles, dispersion energy and distance, where $V = 0$, respectively. As typical for the analytical models, they are assembled empirically, i.e. with their terms having a specific physical meaning – in this case, the first term, raised to the power of twelve, is a repulsive one, acting in a way of *Pauli repulsion*. The second term, raised to the power of six, describes an attractive behavior in long-distance interactions, acting as *dispersion forces*.

Such a model can be fitted in a straight-forward manner solving the problem

$$\min_{\overrightarrow{\theta}} \sum_{i=1}^{n} \left(V_i(\overrightarrow{\theta}) - \widehat{V}_i(\overrightarrow{\theta}) \right)^2, \tag{3.3}$$

where $\overrightarrow{\theta}$, i, n and $\widehat{V}$ denote a vector of fittable parameters, the index of an element from the data-set computed ab initio, the number of elements in the data-set and a value predicted by the analytical model.

The strength of analytical models lies in a very fast evaluation, which causes a minimal overhead from the perspective of the whole simulation, and in their analytical derivatives known *a priori*. On the other hand, their fixed forms impose severe limitations on their ability to describe various PESs they were not explicitly created for.

One such example can be classical force fields and their difficulties with a description of creating and breaking of bonds, leading to an invention of new reactive force fields potentials [184]. Besides them, *spline-fitting procedures* can be successfully applied in some cases [185], similarly to *many-body expansion* [186], *Shepard interpolation* [187], *reproducing kernel Hilbert space* [188], and *interpolating moving least squares* [189].

3.2.2 Artificial Neural Networks

Another way to combine a sufficient smoothness of PES functions concerning density and homogeneity of the grid, its ability to describe various functional forms and beforehand-known analytical derivatives, is the utilization of machine learning. At this field, many different approaches are being investigated, e.g. *Moment tensor potentials* [190, 191, 192], *Spectral neighbor analysis* [193, 194], *Atomic cluster expansion* [195, 196, 197], *Support vector machine regression* [198, 199, 200] or *Gaussian Process Regression* [201, 202, 203], but the most prominent one stays the usage of ANNs.

That said, there are multiple widely-utilized methods, on how to represent PESs via ANNs. While there are convolutional ANNs, Hopfield ANNs, counterpropagation ANNs and Kohonen maps also used in chemistry [204, 205, 206, 207, 208], PESs are usually represented via "classical" feed-forward ANNs (FFANNs) as illustrated in Section 3.2.2. The output of such a network is then given as

$$y(t) = \sum_{i=1}^{n} \alpha_i \, f(t w_i + b_i), \tag{3.4}$$

where t, $y(t)$ and $f(t)$ stand for the input, the output and the *activation function*, which will be described in this section, too. Variables w_n, α_n and b_n denote so-called *weights* and *biases*, which represent "fittable" parameters of the ANN model. The picture also illustrates one of the main advantages of machine-learning models – their ability to be enlarged systematically, i.e. to increase its flexibility without the need to provide additional knowledge of the system's physical properties, in contrast with the analytical, "empirical" models. The enlargement can be done via a) addition of neurons in a hidden layer, i.e. increasing n, or b) addition of one or more hidden layers, which is an approach widely known as *deep learning*.

Talking about activation functions, they determine, how the weighted sum of the inputs is transformed into an output from a node in a hidden layer with a typical choice being the

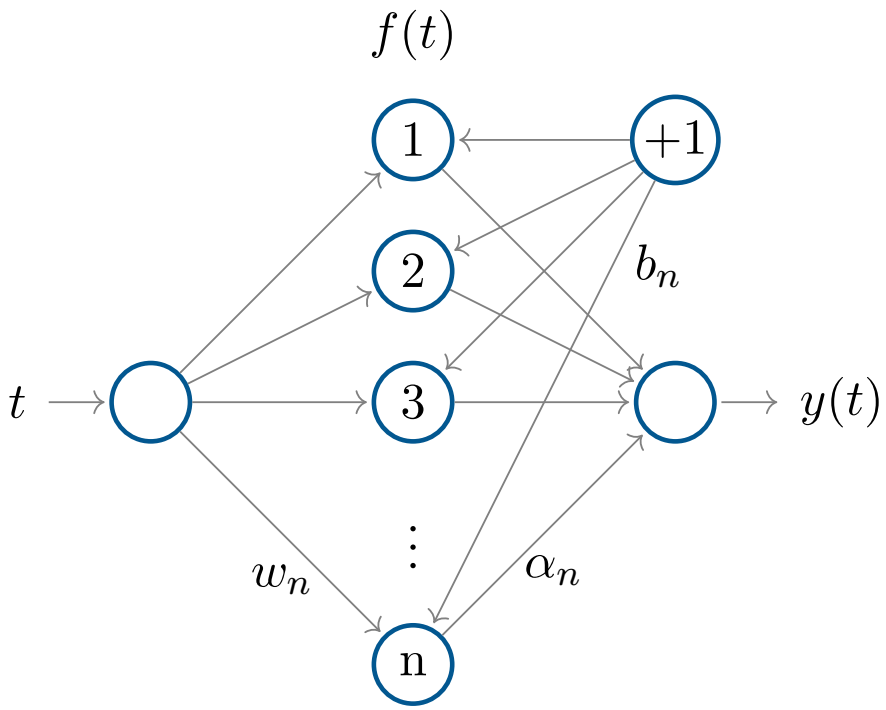

Figure 3.1: The scheme of a simple feed-forward ANN with one hidden layer.

functions of the sigmoidal family, like the logistic function

$$f(x) = \frac{c}{1 + e^{-k(x-x_0)}}, \quad c, k, x_0 \in \mathbb{R}, \tag{3.5}$$

or the hyperbolic tangent

$$f(x) = \frac{e^x - e^{-x}}{e^x + e^{-x}}. \tag{3.6}$$

Due to possible numerical problems like *exploding* and *vanishing gradient* [209, 210] there are many possible functions to mitigate these effects, e.g. *rectifier linear unit* [211, 212, 213], *softmax functions* [214], *rankmax functions* [215], *Gaussian functions* [216, 217] and many others.

Having chosen an activation function, the "ANN training" is straightforward and in principle very similar to Equation (3.3), as its main part is also optimization of the cost function $C\left(\overrightarrow{w}, \overrightarrow{\alpha}, \overrightarrow{b} \middle| x\right)$ with respect to both weights and biases, i.e.

$$\min_{\overrightarrow{w}, \overrightarrow{\alpha}, \overrightarrow{b}} C\left(\overrightarrow{w}, \overrightarrow{\alpha}, \overrightarrow{b} \middle| x\right). \tag{3.7}$$

Now, the cost function can be, again, different with respect to the required numerical properties, e.g. *mean absolute percentage error* [218, 219]

$$MAPE = \frac{100}{n}\sum_{i=1}^{n}\left|\frac{A_i - \widehat{A_i}}{A_i}\right| \quad [\%]\,, \tag{3.8}$$

its symmetrical version [220, 221]

$$SMAPE = \frac{100}{n}\sum_{i=1}^{n}\frac{\left|A_i - \widehat{A_i}\right|}{\left(|A_i| + \left|\widehat{A_i}\right|\right)^2} \quad [\%]\,, \tag{3.9}$$

the sum of squared errors [222]

$$SSE = \sum_{i=1}^{n}\left(A_i - \widehat{A_i}\right)^2, \tag{3.10}$$

or *the root-mean-squared error* [223]

$$RMSE = \sqrt{\frac{\sum_{i=1}^{n}\left(A_i - \widehat{A_i}\right)^2}{n}}, \tag{3.11}$$

where n is the number of elements in a training data-set, i.e. number of *ab initio* computed energies for different geometries of the system.

All of the abovementioned functions exhibit strong tendencies to multimodality, i.e. to possess many local optima making it rather difficult, or even impossible, to localize and recognize the global one. That said, a model can be able to perform reasonably well, with respect to its prediction capacity, even when equipped with parameters corresponding to a local minimum close enough to the global one, which, unfortunately, does not remove the optimization problem.

To deal with it, many approaches were developed, starting with different variants of gradient-based methods [224, 225, 226], utilization of specific activation functions [227] or training via gradient-free methods like evolution-based approaches [228, 229, 230] or swarm-based methods [231, 232, 233, 234, 235].

The point of optimization in functions of such a general character is to take care of both *exploratory* and *exploitative* aspects of the optimization approach [236, 237], i.e. to look at its ability to investigate a numerical domain at a large scale [238, 239, 240, 241] and detect promising global minima or local minima close-enough to them and of the ability to get as close as possible to the localized minimum [242, 243, 244]. While simple gradient-based methods, typically tend to get stuck at local minima close to the initial point of the numerical optimization, swarm-based methods, for example, do struggle to get close to the minimum itself, keeping "jumping" in its neighborhood very often. The usual approach is to either use

a robust method efficient enough for our needs [245] or to chain several of these methods to explore the numerical domain globally and to approximate the localized minima as close as possible via any "local" approach [246].

Another possible caveat of ANNs training is its possible insufficient flexibility. Aside from manual solutions, like creating oversized networks and simplifying afterward considering its results, the more systematic way consists of the optimization of ANN's *hyperparameters* – the parameters, determining ANN's architecture itself, e.g. number of its hidden layers and their sizes. For that reason, many different hyperparameter approaches were developed [247, 248, 249, 250, 251], usually combined with cross-validation to prevent problems with ANN overfitting [252, 253].

Overfitted, but also underfitted ANN is an obvious danger, depending not only on the optimizer but on the quality of the training data set, too. The most prominent problem with *ab initio* data is usually an occurrence of outliers, making it necessary to detect and remove them [254, 255, 256, 257, 258] before the training itself.

The last important thing which needs to be considered before representing PES is the choice of *geometry descriptors*, i.e. the convenient particles' coordinates, which need to be invariant with respect to the equivalent system's geometries. Taking simple Cartesian coordinates into account, they will differ after the system is just translated – albeit it is a physically equivalent situation, considering an isolated system, from ML model's point-of-view the descriptors, i.e. inputs, are completely different, thus the resulting energy will be probably also different. An obviously better choice would be *internal coordinates*, as illustrated in Figure 3.2 for a 3-body system with two internuclear distances and one angle. Looking at the figure, it is obvious, that such description offers an invariance with respect to both translational and rotational transformations. However, it is not sufficient for permuted systems, where their atoms got exchanged. In such a case, the description of both internal distances and angles differs, thus it is not self-sufficient for ML.

One of the most popular "self-sufficient" methods for assembling convenient geometry descriptors is the Behler-Parrinello approach based on atomic-centered symmetry functions [259, 260], which describe an atomic neighborhood defined strictly by cutoff limit, thus limiting the number of described interactions. This approach is very useful for large systems, where small inaccuracies are not significant for an overall behavior and the number of particles involved renders other approaches infeasible. However, due to the small number of particles in N_2^+/He collision complex, this one, or other novel approaches [261, 262] was not in our interest.

The other approach, more suitable to smaller systems and very-well researched [263, 264, 265] is utilization of PIPs. The approach is, in our case, advantageous because of its simplicity, thus it was adopted in this thesis.

The method utilizes *the monomial symmetrization* approach [266, 267, 268] starting with the system described via all the internuclear distances r_{ij}, between i-th and j-th particle,

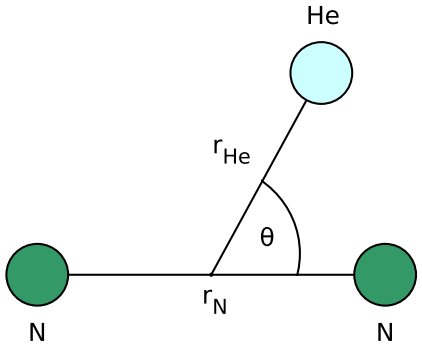

Figure 3.2: An example of internal coordinates for 3-body system

rendering inner angles unnecessary for its purposes, as illustrated in Figure 3.3.

The first step is the transformation from the distances to reciprocal values

$$y_{ij}(r_{ij}) = \frac{1}{r_{ij}} \tag{3.12}$$

or to Morse variables [266]

$$y_{ij}(r_{ij}) = 1 - e^{-r_{ij}/c},\ c \in \mathbb{R} \tag{3.13}$$

which are further expanded in multinomials. For example, in the case of a 3-body system, the potential looks like

$$V = \sum_{m=0}^{M} C_{abc} \left[y_{12}^{a}\ y_{13}^{b}\ y_{23}^{c} \right] \quad (m = a + b + c), \tag{3.14}$$

where C are real coefficients. In the next step, multinomials get replaced with monomials like

$$V = \sum_{m=0}^{M} D_{abc}\ \mathcal{S} \left[y_{12}^{a}\ y_{13}^{b}\ y_{23}^{c} \right], \tag{3.15}$$

with $\mathcal{S}$ denoting a general operator, that symmetrizes monomials. For illustrative purposes, the symmetrization approach is shown at Table 3.1, considering a model molecule A_2B with basis elements listed in Table 3.2. The potential V then looks like

Atom labels (A A B)	Monomial	Normal order
1 2 3	$y_{12}^a y_{13}^b y_{23}^c$	$y_{12}^a y_{13}^b y_{23}^c$
2 1 3	$y_{12}^a y_{23}^b y_{13}^c$	$y_{12}^a y_{13}^c y_{23}^b$
Symmetrized term	$y_{12}^a \left(y_{13}^b y_{23}^c + y_{13}^c y_{23}^b \right)$	

Table 3.1: An example of monomial symmetrization

m	Basis elements		
0	[0 0 0]		
1	[1 0 0]	[0 1 0]	[0 0 1]
2	[1 1 0]	[1 0 1]	[0 1 1]
	[2 0 0]	[0 2 0]	[0 0 2]

Table 3.2: Example basis for A_2B molecule

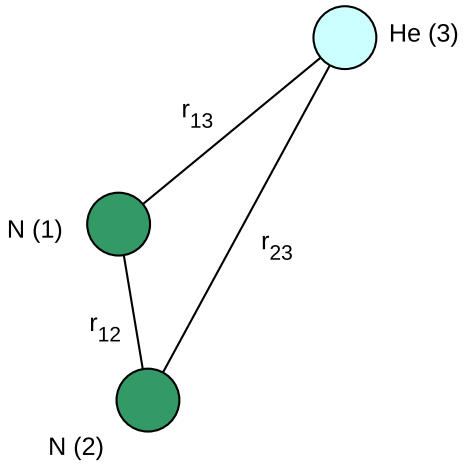

Figure 3.3: 3-body system described via only internuclear distances

$$V\left(\overrightarrow{r}\right) = V_0(\overrightarrow{r}) + V_1(\overrightarrow{r}) + \ldots + V_M(\overrightarrow{r}) \tag{3.16}$$

$$V_m(\overrightarrow{r}) = D_{abc}\, y_{12}^a \left(y_{13}^b y_{23}^c + y_{13}^c y_{23}^b \right) \tag{3.17}$$

$$m = a + b + c \tag{3.18}$$

$$m \in 0, 1, \ldots, M, \tag{3.19}$$

with coefficients $D \in \mathbb{R}$ to-be-fitted via least squares, in the same manner as given by Equation (3.7).

In this thesis, fully-connected FFANNs were used. The architecture consisted of four

	Theoretical Peak [TFlops/s]	Storage Capacity [TB]	Interconnect Throughput [Gb/s]
Salomon	2011	2138	56
Barbora	849	339	100
Karolina	15700	1400	200

Table 3.3: Technical overview of utilized computational clusters.

layers including an input layer with three neurons representing coordinates of the N_2^+/He collision complex, two hidden layers containing twenty and five neurons, respectively, and an output layer providing the interaction energy of the complex. Standard logistic activation functions given by Equation (3.5) were assigned to the neurons in hidden layers while the linear activation function

$$f(x) = ax + b,\ a, b \in \mathbb{R} \tag{3.20}$$

is used both in the input and the output neurons. The training data sets were created via MDSs performed in the on-the-fly regime.

Separate ANNs were trained for each initial rotational-vibrational state of the N_2^+ ion and each collision energy, with training utilizing Kalman filter approach [269]. That way, a set of $[j, v, E_{\text{coll}}]$ specific ANNs was obtained with j and v denoting rotational and vibrational state, respectively. PIPs of reciprocal values of distances between atomic nuclei in the N_2^+/He complex was used as the input to the ANNs.

The size of training sets was not equal for all the cases – the number of training points depended on the collision energy E_{coll}, the number decreasing with the increasing E_{coll}. That said, the numbers range from 10^5 to 4×10^6 of elements, order-wise.

3.3 Computational Resources

All the computations were realized utilizing the computational infrastructure of National Supercomputing Center IT4Innovations[3]. Namely, the utilized clusters were Salomon[4], Barbora[5] and Karolina[6] with their specifications listed in Table 3.3. Also, some of the auxiliary results were computed on Curie cluster, provided by LCPQ institute[7].

[3] https://www.it4i.cz
[4] https://www.it4i.cz/en/infrastructure/salomon
[5] https://www.it4i.cz/en/infrastructure/barbora
[6] https://www.it4i.cz/en/infrastructure/karolina
[7] https://www.lcpq.ups-tlse.fr

Chapter 4

Results

This section is an overview of the results achieved in the course of the dissertation project. It starts with thoroughly described results of molecular interactions, followed by the molecular dynamics and the computations of the transport properties.

The molecular interactions part comprises the all achieved results, as it was the main focus of this project and the work mainly done by the author. The other two parts are present to put all the results in context, while the presentation is briefer, as these results were mostly achieved by other colleagues, and the author's participation in the computations themselves was marginal.

From now on it will be strictly specified, when the results were not achieved directly by the author to prevent any possible confusion and diminishing of someone's intellectual involvement.

4.1 Electronic Structure

This part describes ab initio computations of molecular interactions in great detail. It starts with standalone N_2^+ cation as the major part of the whole collision complex N_2^+/He , after the expected charge transfer

$$N_2 + He^+ \rightarrow N_2^+ + He, \tag{4.1}$$

due to the significant difference in the ionization potentials of He and N_2. Thus, electronically excited states of the resulting N_2^+ ion will play a significant role due to the excess energy released by the charge hop. Supposedly, N_2^+ is determining a predominant part of physical (and numerical) properties of the complex, which is fully investigated and described afterward.

That said, a thorough numerical analysis was performed (and published in [270]) with respect to different orbital spaces and basis sets, not only to determine an optimal configuration but also to obtain a sufficient MCSCF configuration for MDSs, as the computational demands make on-the-fly MRCI usage infeasible.

To further reduce the computational costs and to simplify the computations, the core correlation is not taken into account in our calculations, leading to an expected underestimation of the dissociation energy of ~ 0.05 eV and an overestimation of the bond length and harmonic frequency of respectively 0.001 Å and ~ 10 wavenumbers [271].

4.1.1 Dinitrogen Cation N_2^+

Accurate calculation of correlation effects for N_2^+ -ion is known to be a very difficult problem. In general, the larger the basis set and the larger the active space for MRCI, the better the results. But for N_2^+, as shown by Liu and colleagues [272], this is not a systematic situation. This is also confirmed in this work as shown in Table 4.1 which shows the ground state dissociation energy for different basis sets and active sites. In fact, at the MRCI level, the separation energy for all active spaces increases on a fixed basis, while for a given basis set, increasing the orbital spaces leads to a decrease in the binding energy. Compared to the last experimental value of $D_e = 8.71\,\text{eV}$, [273] AVQZ′/OS2 appears to be a reasonable choice, moreover at a relatively low computational cost. In this case, the difference between MCSCF and MRCI is only 3.7% with an absolute error of 0.321 eV. With this combination, r_e for MCSCF and MRCI are 112.1 pm and 112.0 pm, respectively, and the corresponding ω_e, 2193 and 2185 cm^{-1}, compared to the experimental values $r_e = 111.6\,\text{pm}$ and $\omega_e = 2207\,\text{cm}^{-1}$ [274].

In general, the variations with basis sets and active spaces are smoother, and we only report the differences between MCSCF and MRCI calculations. Figure 4.9 shows the evolution of the difference between the spectroscopic constants MCSCF and MRCI. As can be seen, the trend with different basis sets is almost the same, no matter what active space is considered. Except for the smallest case, OS1, all active spaces with an increasing basis give better results. Also AVQZ′/OS2 seems to be a good compromise with very little variation in the MCSCF results compared to the reference AV6Z/OS4 MRCI.

The difference between MCSCF and MRCI potential energy for the ground state is shown in Figure 4.8 for the full range of r. Even when increasing the fixed threshold or active space (inset), quite bad behavior is seen due to the subtle interaction of static and dynamic correlation, as well as an approximation of the consistency size. All previous comparisons show that MCSCF and MRCI PEC show a similar shape around the minimum. This similarity in PECs is also reflected in the differences in vibrational levels in Figure 4.9. The differences are very small for the lowest five levels when using the OS2 space and the AVQZ basis set or larger. This difference gradually increases with v but remains low until $v = 15$. The difference

in larger v is related to the error in D_e already commented above. Although the absolute errors seem large in some cases ($\sim$500 cm^{-1}), the overall difference between the MRCI and MCSCF results remains less than $2-3\%$ for vibrational of G_v levels.

In Table 4.2 we give the dissociation energy of the $A\,^2\Pi_u$ state for different basis sets and sizes of the active space. The same trend for the baseline can be seen here. Increasing the basis set deepens the potential well, while the effect on the active space is less systematic, for example, the deviations of MCSCF vs MRCI are larger for OS3 than for OS2. After that, AVQZ′/OS2 also seems to be a good compromise for this condition.

The global behavior for r_e, ω_e and D_e shown in Figure 4.11 is generally the same as obtained for basic state. The results are again in favor of the AVQZ′/OS2 combination, which compares well to the best estimate with AV6Z/OS4.

In Figure 4.12 it is seen that the energy difference between MCSCF and MRCI decreases globally with increasing basis sets and does not show the same behavior with r with a small increase near $r = 2.5$ Å and around the minimum. As in the ground state, the green curve corresponding to the calculation set AVQZ′/OS2 gives the overall best match between the MCSCF and MRCI energies for all r.

Figure 4.13 shows the monotonic change in the difference of vibration levels MCSCF and MRCI with v. Again, the best agreement with reference calculations (AV6Z/glsos4, MRCI) is obtained for the combination AVQZ′/OS2. Based on a detailed examination of the various basis sets and active sites for the ground state and the first excited state of the N_2^+ ion, AVQZ′/OS2 appears to be a good candidate for a balanced description of all fundamental spectroscopic data at a reasonable computational cost. This is further illustrated by the figures 4.14 and 4.15, where AVQZ′/OS2, AVQZ′/OS2 and AV6Z/OS4 potential curves for the two lowest states are plotted. The global behavior is good and the curves are quite similar, although the binding energy is slightly underestimated for the ground state ($X\,^2\Sigma_g^+$) and slightly overestimated for the excited state ($A\,^2\Pi_u$) at the MCSCF AVQZ′/OS2 level. It is noteworthy that for both states the results for MCSCF AVQZ′/OS2 almost match those for MRCI AV6Z/OS4. Thus, this reasonable choice will be used to perform dynamic calculations for the N_2^+/He complex using on-the-fly MCSCF or neural network-based potentials. In the figures 4.8 and 4.12 we show the difference between the potential energies MCSCF and MRCI for the ground state $X\,^2\Sigma_g^+$ and the lowest excited state $A\,^2\Pi_u$, relative to the dissociation. From these graphs it is clear that the spaces OS1 and OS2 (brown and blue curve) lead to larger deviations than the active space OS3 with the same basis set AV6Z (red curve). Regardless of the basis set, OS3 leads to close potential curves over a large range of interatomic distances, with a maximum difference of $\lesssim 0.2$ eV for the ground state and less than 0.3 eV for the excited state. This is true for the mean set AVQZ′ at the expected reasonable computational cost for the complex N_2^+/He . The similarity of the potential curves can also be seen in the differences in the vibrational levels of the two states shown in figures 4.9 and 4.13 are signed

off. In both cases, the differences are very small for the lowest five levels when using the OS3 space and the AVQZ basis set or larger. For the ground state, the difference grows slowly with v but remains very low up to $v = 15$, indicating that usually the dissociation part of the potential is affected by the missing dynamical electron correlation. The same trend applies to the excited state, but slightly worse. Although the absolute errors seem large in some cases ($\sim$1000 cm^{-1}), the overall difference between the MRCI and MCSCF results remains less than 2–3 % for levels vibrations G_v. The effect of increasing the active area on the spectroscopic constants r_e, D_e and ω_e is very small, as can be seen in Figures 4.10 and 4.11. At the MRCI level, the ground state dissociation energy obtained with the AVQZ basis set and the OS3 active space, 8.75 eV (see Table 4.1), compares very well with the recent experimental value, $D_\mathrm{e} = 8.71\,\mathrm{eV}$ [273], for example $r_\mathrm{e} = 111.6\,\mathrm{pm}$ and $\omega_\mathrm{e} = 2207\,\mathrm{cm}^{-1}$ spectroscopic constants [274]. The same goes for the $\mathrm{A}\,^2\Pi_u$ state. An important point here is the size of the basis set, as evidenced by the significant differences between AVTZ and other extended basis sets.

With all that said, all the research efforts were focused on reactions described by Equations (2.72) and (2.73), while the uncommon processes

$$\mathrm{N_2^+ + He \rightarrow [NHe]^+ + \mathit{N}} \tag{4.2}$$

$$\mathrm{N_2^+ + He \rightarrow NHe + \mathit{N}^+} \tag{4.3}$$

were omitted in the current phase of the project both due to the very large collision energies necessary and due to an impractically low probability of happening. Similarly, the charge-transfer channel

$$\mathrm{N_2^+ + He \rightarrow N_2 + He^+} \tag{4.4}$$

was only briefly considered, as the reaction would also require very high collision energy, but also the dinitrogen cation $\mathrm{N_2^+}$ in a highly excited state, notoriously hard to obtain via ab initio methods. That said, the preliminary computations were performed both for $\mathrm{N_2^+}$ itself and the whole $\mathrm{N_2^+/He}$ complex, as described in this section and Section 4.1.2, respectively.

The assumed relevant states are illustrated in Figure 4.1. Their computations exhibited, as expected, a number of numerical problems, which have been dealt with only partially, so far. The first attempt is visualized at Figure 4.2, demonstrating convergence problems on the eleven lowest a_g states, with 5 lowest ones being significantly better converged than the rest, although every single one except the two lowest states is "contaminated" by one or multiple avoided crossings, the phenomenon occurring more often with higher excitation as the states do cross each other frequently. With rather "robust" numerical configuration, adopting aug-cc-pV5Z basis set, OS2 and a subsequent usage of HF, MCSCF and MRCI,

the computations obviously need more even more careful treatment. For that, it is vital to compute possibly more states than necessary to interpret avoided crossings correctly, while the highest states tend to be always the ones with the most severe convergence problems. Eventually, the greatest improvement with respect to the convergence issues was adopting an approach, where the wavefunction gets stored after every computed point in MCSCF method and so the 1-D cuts of MCSCF grid are computed in a continuous manner, using the previous point's wavefunction as an initial point for the current one. In the subsequent step, MRCI is run point-wise, as with the first computations, because of its significant runtime, but it is also using the wavefunctions of the corresponding MCSCF points as an initial state for the optimizer. This approach is described in Section 3.1.2.

To broaden our initial understanding of the doublet, higher excited states of N_2^+ , there were computed eleven states of Σ_u^+, Σ_u^-, Σ_g^+, Σ_g^-, Π_g, and Π_u irreducible representations and the dissociation limits specified by separated atom term symbols, were also determined. These results are illustrated in Figures A.1 to A.6 in Appendix A.

Finally, higher collision energies were also partially computed, mostly for testing the ANN-based approach of PES representation, to evaluate its usefulness even for these models. The preliminary results for the collision energy $E_{\text{coll}} = 25\,eV$ seem very promising, with the absolute residual (energies obtained via MCSCF - energies obtained via ANN) mean of $0.00018\,H$ and maximum residual mean of $0.00525\,H$. Both the sample-wise and cumulative residual distribution can be seen in Figures 4.3 and 4.4. The ANN here consisted of 2 hidden layers containing 20 and 5 neurons, respectively. All the hidden neurons were equipped with logistic activation functions, described by Equation (3.5).

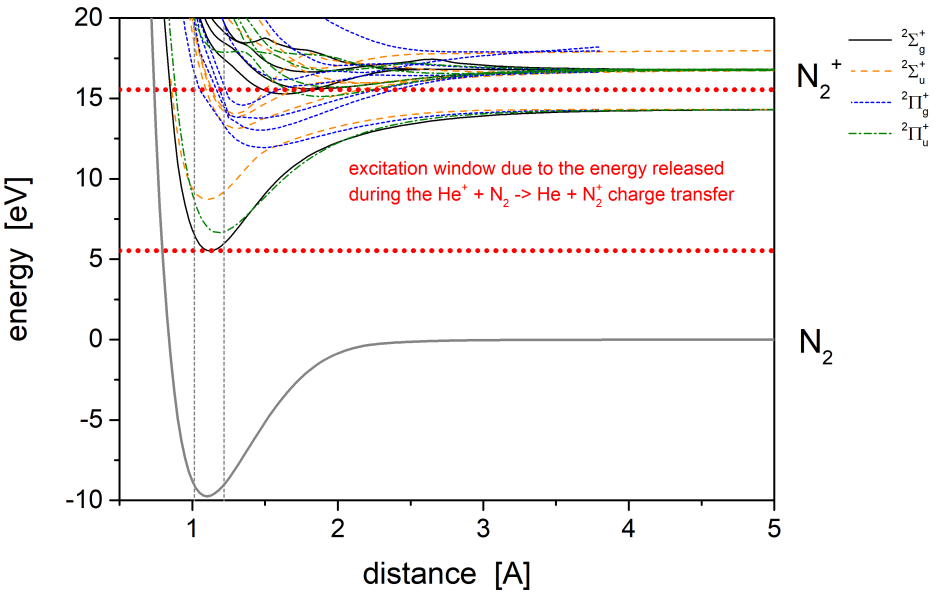

Figure 4.1: PECs of different doublet N_2^+ states with a relevant excitation window visualized.

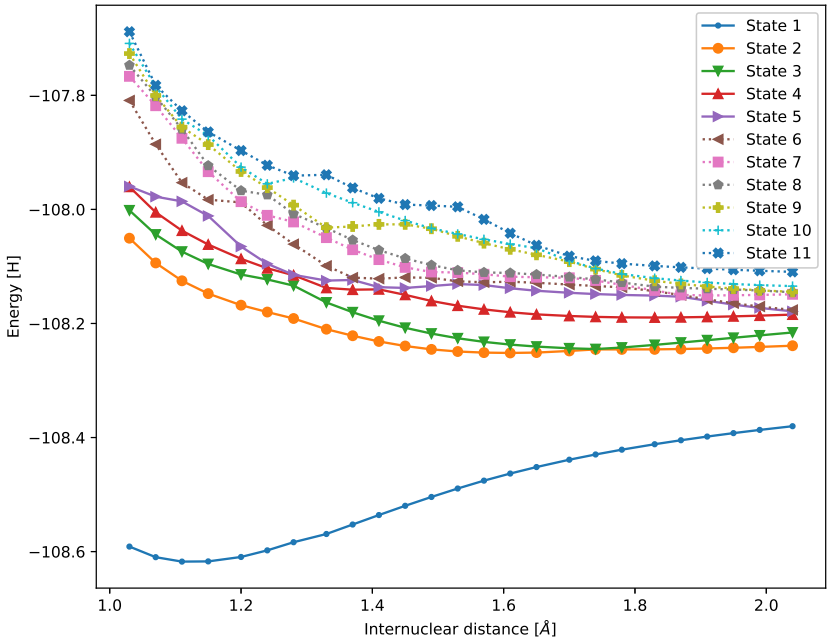

Figure 4.2: PECs of different doublet N_2^+ A_g states

4.1.2 Collision Complex $[N_2/He]^+$

Extending the N_2^+ calculations presented in the previous subsection, we also performed similar calculations for the N_2^+/He complex with the main goal of verifying the accuracy of the MCSCF and MRCI methods in this, more complex, case. To save computational time, only an approach similar to AVQZ′/OS2, which proves the quality of the N_2^+ calculations in the previous subsection, is used, so the detailed convergence analysis is not performed again for N_2^+/He .

In Figure 4.16 we show MRCI and MCSCF PESs for selected slices of the potential energy surface for different approximation angles. In any case, the MRCI curve at short He−N_2^+ distances is less repulsive than the MCSCF curve because the dynamical correlation between He and N_2^+ electrons. In Table 4.4 we list the minimum of the potential ground state curve for the MCSCF and MRCI calculations. For comparison with previous calculations, we also report the He−N_2^+ distance and the corresponding dissociation energy for a typical T-shaped geometry and $\theta = 45°$. In all cases, the distance N_2^+ is kept equal to its equilibrium value ($r_e = 2.11$ a.u. ≈ 1.117 Å). We see that our results MRCI are very close to the previous calculations [275, 30, 27]. As seen in Table 4.4, our calculation found a minimum for geometries close to the 45° angle of attack, as was the case in Miller's MCSCF-CI study *et al.* [26] but

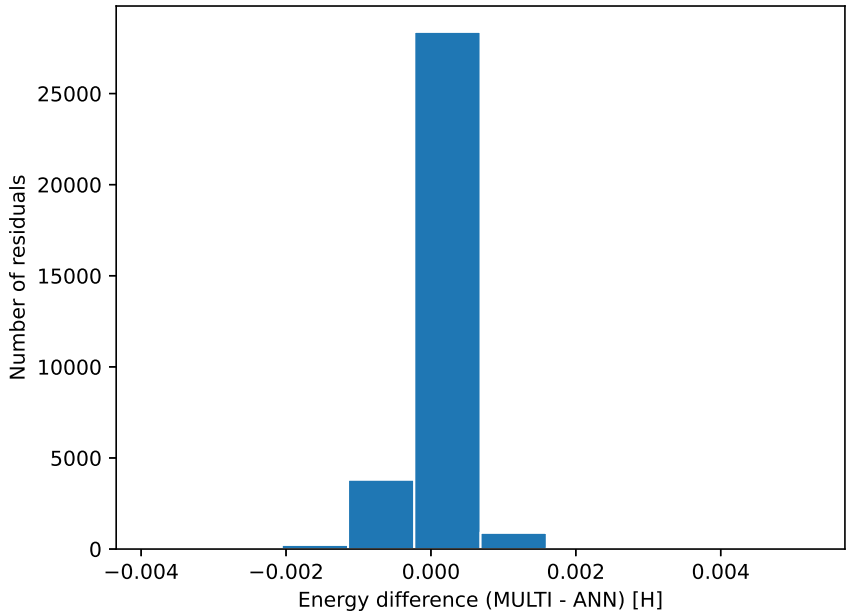

Figure 4.3: Distribution of residuals MCSCF - ANN for $E_{\text{coll}} = 25\,eV$.

differs from the calculation of Guillon and Stoecklin [27] who found the T-shaped form to be the most stable structure. We can also note that for 90° the second one gets a shallower potential. Unfortunately, these authors did not provide sufficient computational detail to investigate the origin of this discrepancy. The well depths are so close together that this sensitivity may result from different multireference treatments or different basis sets. For both excited states of A' and A'' symmetry, we found a minimum at 90° as reference [30] with very similar characteristics.

More than all previous studies, we have explored PES not only at the smallest but also at a larger scale to gain insight into its global behavior and test its sensitivity to the most interesting of *ab initio* methods previously considered for N_2^+. Some representative sections of the PESs ground state of the N_2^+/He ion at a fixed angle corresponding to the N_2^+/He equilibrium geometry (θ_e) are shown in figures 4.17 and 4.18 for MCSCF and MRCI, respectively. In both images, the minimum area in the inset has been enlarged. Along the distance He$-N_2^+$ (R) the behavior is relatively flat, but at very high energies around 8000 meV we see the beginning of the exit recombination channel $HeN^+ + N$. The global shape is the same for the MCSCF and MRCI potentials, although the HeN^+ MRCI minimum valley appears to be slightly shifted to smaller R distances. This agrees with our comment about Figure 4.16. For both excited states, as shown in Figures 4.19 to 4.22, the global behavior is very similar between MCSCF and MRCI again with a shallow minimum in R. The main difference is that for both excited

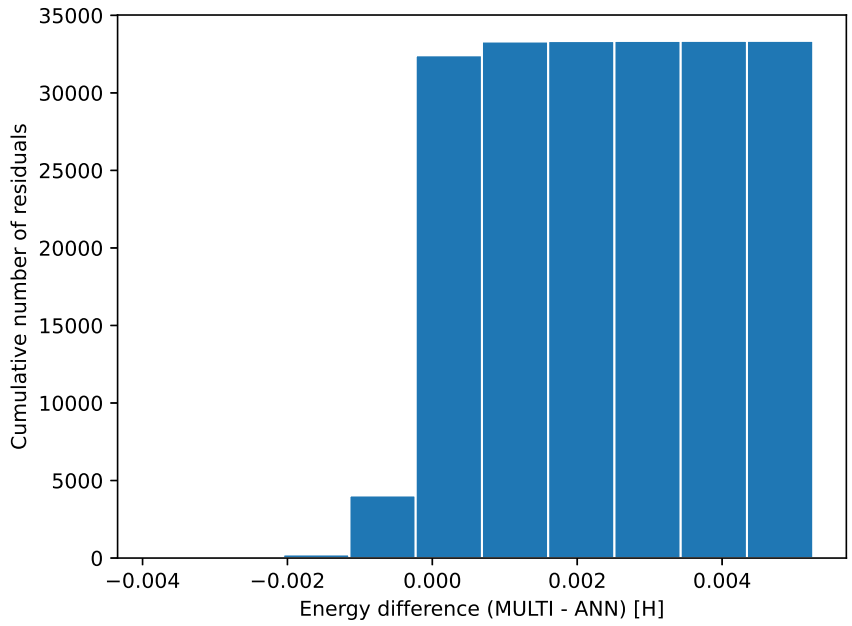

Figure 4.4: Cumulative distribution of residuals MCSCF - ANN for $E_{\text{coll}} = 25\,eV$.

states MRCI leads to a slightly deeper well, to a slightly shorter R.

With all this in mind, we conclude that the MCSCF/AVQZ′/OS2 approach represents an acceptable compromise between computational requirements and accuracy from the point of view of subsequent dynamic calculations. To further support this choice, we carefully examine the computational costs of the MCSCF and MRCI methods (used at the AVQZ′/OS2 level). This analysis shows that for the version of MOLPRO used in this work and for the computers where the calculations were performed (equipped with 2.6 GHz AMD 7H12 processors with fully 128 CPU cores and 256 GB RAM per compute node), typically about 45 seconds are needed to evaluate the interaction energy N_2^+/He and its gradients in the ion configuration when MOLPRO runs in serial mode (i.e. without parallelization). From the perspective of future dynamic computations, where typically thousands of trajectories are needed, each containing (depending on the collision energy) hundreds to thousands of integration steps, a total of tens of thousands of core clocks are required for integration. collision data (cross sections) for certain collision energy, an acceptable requirement when using modern supercomputers. When using the MRCI method, on the other hand, the situation is less favorable. At the same level of accuracy (AVQZ′/OS2), a single-point calculation (performed in serial mode) requires about 90–100 hours for low collision energies ($E_{\text{coll}} \approx 0.01$ eV) and this number decreases approximately to 5–10 hours in the region of high collision energy ($E_{\text{coll}} \approx 50$–$100$ eV). The resulting requirements of dynamical calculations thus reach the level of several million

to several tens of millions of core hours for collision energy. While such requirements are still acceptable for today's available supercomputers, the associated wall times of up to tens or even hundreds of days are not.

Eventually, an interesting question that deserves a thorough consideration is the effect electronic excitations have on the dynamics of N_2^+/He collisions. Calculations focused on this problem are being presently prepared in our group. An approximately diabatic interaction model including the lowest electronic states of the N_2^+/He ion ($2 \times A' + A''$) proposed in [30] and asymptotically correlating to the $X\,^2\Sigma_g^+$ and $A\,^2\Pi_u$ states of the N_2^+ ions will be used and build up on the results obtained within the present work.

The chosen preliminary results containing a demonstration of basis set and orbital space effects on N_2^+/He PECs are visualized in Figures 4.5 to 4.7. The computations were performed utilizing only MCSCF due to its speed and with the primary goal of obtaining knowledge of the specific numerical behavior and the problems present. The points group is, again, C_s and there are 7 states being computed together in the state-averaged regime, with 5 of them belonging to A' irreducible representation and the two remaining states to A''. The computations were performed with aug-cc-pVTZ, aug-cc-pVQZ, aug-cc-pV5Z, and aug-cc-pV6Z basis sets together with both abovementioned orbital spaces, i.e. $11A'$, $2A''$ and $12A'$, $3A''$. Finally, the nitrogen distance was fixed as $r = 1.12$Å and the energy was computed as dependent on R with the internal angle $\theta = 0°, 45°, 90°$. All the configurations computed so far can be seen in Figures B.1 to B.24.

4.2 Molecular Dynamics

This part focuses on the description of the results achieved with MDSs using the knowledge gained from this work, i.e. information on molecular interactions. This and the following section will not describe the problems in depth, but only present the results, as the main goal is to put the results of this work into the perspective of the wider project.

The author claims that the following results were done with his colleague S. Paláček (co-author of [270, 276, 277]) who did the calculations.

Since, to the best of the author's knowledge, no direct measurements have been reported in the literature for NRS cross sections of N_2^+/He or CID cross sections, an indirect comparison of experiments can be made with pseudo-experimental MTCS1 values obtained from measurements mobilities of N_2^+/He using the inverse method described in [275]. An overview of the most extensive experimental data on mobility N_2^+/He [278, 279, 280] is given in Appendix Figure 4.23, corresponding to MTCS1s obtained from *inverse method* (IM) is shown in the main panel of the figure. A summary of the data obtained for MTCSs, especially for MTCS1, is given immediately in Figure 4.24, with the most important observations obtained in Figure 4.24 following. First, very good agreement was found between theoretical data and

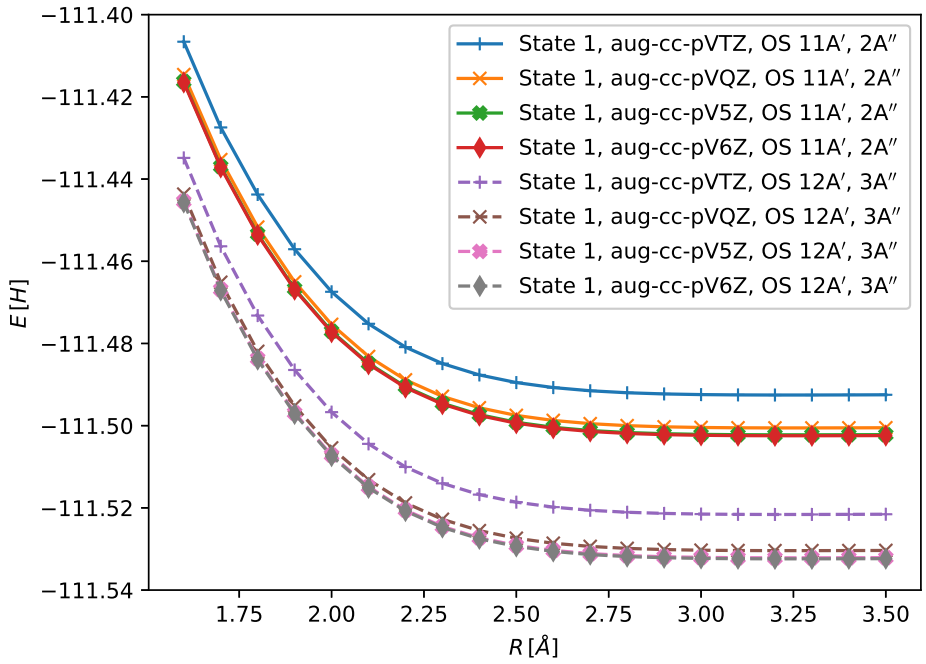

Figure 4.5: Convergence of N_2^+/He PECs for the 1st state.

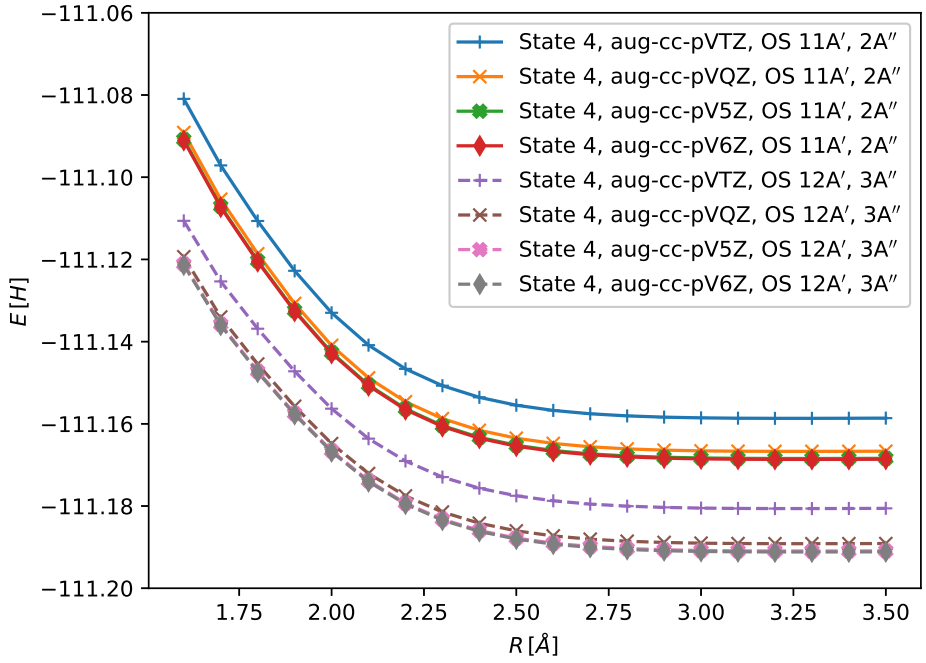

Figure 4.6: Convergence of N_2^+/He PECs for the 4th state.

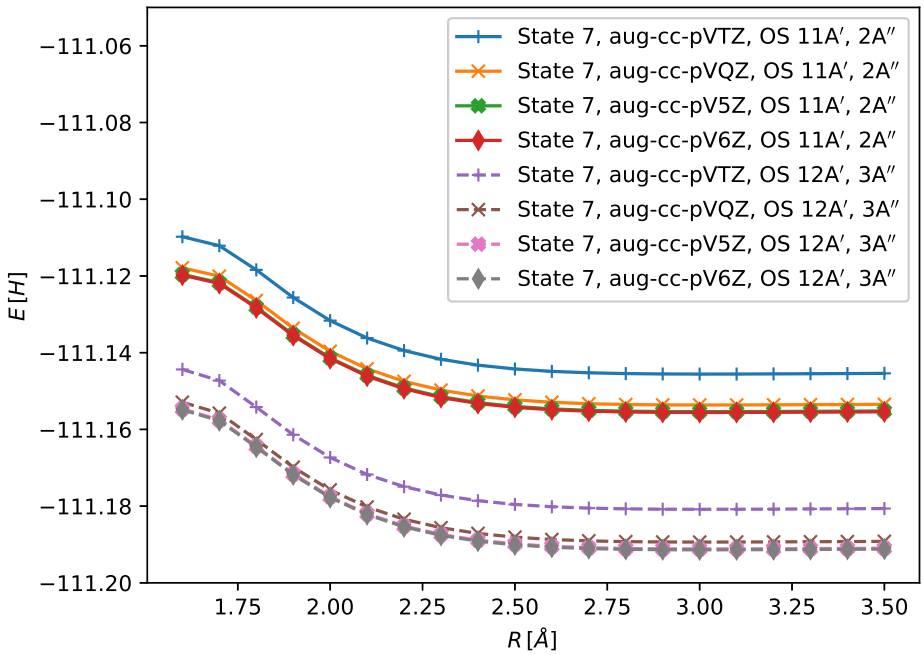

Figure 4.7: Convergence of N_2^+/He PECs for the 7th state.

IM calculations for $E_{\text{coll}} \approx 0.05 - 1.0\,\text{eV}$. This is particularly evident when theoretical data are compared with IM values obtained from recent experiments [280]. Second, for low collision energies (here represented by $E_{\text{coll}} = 0.01\,\text{eV}$), a clear deviation between theory and IM is seen. The theory underestimates the average IM by about 4–5 times, probably because the MCSCF method underestimates the high polarization forces acting between the N_2^+ ion and the He atom for a long time it does not describe. distances with sufficient accuracy. And these long distances are often significant at very low collision energies such as $E_{\text{coll}} = 0.01\,\text{eV}$ as described in Figure 4.25 where the MTCS1s contributions are described for j=0,v=0 and selected collision energy.

Another important issue that is the difference between the data obtained with MTCS1s (Equation (2.74)) and MTCS2s (Equation (2.75)) is analysed in Figure 4.26. The data shown in this figure clearly show that both methods of MTCS calculations give similar results, the deviations are (mostly) below $0.6\,\text{Å}^2$, even for the largest N_2^+ rotational-vibration excitation and the highest collision energy, where inelastic processes can be expected to play a role.

Furthermore, not much can be said about the N_2^+/He CID cross-section, except that it is very small at all collision energies and for all N_2^+ rotational-vibrational excitations, as is evident from what is seen from Figure 4.27. Interestingly, even at the highest N_2^+ vibrational excitation (j=0,v=10), the CID cross section is always below about $0.8\,\text{Å}^2$ when there are two lower excitations. is also considered here for the rotational-vibrational ground state of the ion N_2^+ .

As discussed before, FFANNs were constructed specifically for each N_2^+ initial rotational-vibrational excitation and for each collision energy considered. In this way, highly accurate representations of specific domains of the N_2^+/He potential energy surface which are relevant at particular collision conditions have been obtained. As an illustration of achieved accuracy, we provide a comparison between cross-sections obtained for $N_2^+(j{=}0,v{=}0)$ from the on-the-fly calculations and from alternative calculations using the optimized ANNs in Figure 4.28. The agreement between the two calculations is excellent and the accuracy of the ANNs is thus fully warranted. The quality of the developed ANNs is further guaranteed by insignificant deviations between the training energies and the estimates returned by the ANNs. Typically, the deviations are well below 1 meV for $E_{\mathrm{coll}} \lesssim 1\,\mathrm{eV}$, up to 5 meV for $E_{\mathrm{coll}} \lesssim 50\,\mathrm{eV}$ and reach only about 13 meV for the highest collision energy considered in this work ($E_{\mathrm{coll}} = 100\,\mathrm{eV}$).

And finally, the effect of angular momentum (J) alignment N_2^+ on collisions N_2^+/He is described for the particular case $j{=}0,v{=}0$ by Figure 4.29, where the cross sections are calculated for parallel (PAR) and perpendicular (PER) aligned J are compared with data obtained for unaligned J (NA). As can be seen from Figure 4.36, the MTCSs values obtained for PAR, PER, and NA of J are relatively close to each other, which means that the alignment effect of J from MTCS is generally small, considering the collision energy. The only exception is the lowest collision energy, $E_{\mathrm{coll}} = 0.01\,\mathrm{eV}$, where the difference between PAR/NA and PER/NA data is approximate $\pm 5\,\text{Å}^2$ is (but still less than 10 % of the NA value). For the CID cross-sections, the differences appear to be more pronounced when the relative deviations are taken into account, but the absolute magnitude of the differences is small. Importantly, the CID cross-sections are small for both N_2^+ both with aligned and non-aligned J.

4.3 Transport Properties

In this section, the transport properties of N_2^+ in He and He^+ in N2 are briefly described, because this is the last development of the whole project at the moment.

These results were produced using the results of MDSs as input and the author of this work did *not* participate directly, as the computations themselves were performed by colleagues from the laboratory LAPLACE[1].

First, considering the available results in the literature, selected mobility measurements of N_2^+/He (K_0N) [278, 281, 279, 280, 282] published in the last five decades are summarized in Figure 4.30 . It is clear that the recent results [278, 281, 279, 280] are in good agreement and their reliability can be considered established. However, [282]'s oldest measurement is significantly different from the most recent and will therefore not be considered in the current analysis.

[1] www.laplace.univ-tlse.fr

A comparison of our transport property estimates calculated for the rotational-vibrational ground state N_2^+ (j=0,v=0) with pseudo-experimental IM benchmarks is illustrated in Figure 4.31. In the top panel of the figure, N_2^+/He mobility is considered the most important finding that the agreement between our theoretical data and the IM data is very good. In the bottom panel of Figure 4.31 our theoretical and pseudo-experimental IM estimates of the longitudinal (D_L) and transverse (D_T) diffusion coefficients N_2^+ of ions in helium are compared. Note that, for simplicity, only IM values obtained from cross sections obtained from the latest experimental mobility data [280] are given, since the two residues that the IM data come from experiments [278, 279] almost matches the description. As with the N_2^+ motion, a perfect agreement was found between theoretical and pseudo-experimental IM data for weak and moderate electric fields.

Next, for the most recent experimental data [280], we found [276], which resulted in IM cross sections (MTCSs) in agreement very close to our theoretical estimates only in a limited range of collision energies (varying between $E_{coll} \approx 0.05\,eV$ and $E_{coll} \approx 2\,eV$). Outside this region the agreement is worse, the differences between the theoretical and IM data are very clear. On the other hand, an excellent agreement can be seen with the motion data in almost the entire range of electric field reduction considered Figure 4.31, at least up to $E/N \approx 200$–$250\,Td$.

The roots of this apparent difference can be revealed from Figure 4.32, where the collision energy distributions at the N_2^+/He center of gravity are described for selected values of electric field reduction. These distributions reach their maxima around $E_{coll} \approx 0.04\,eV$ for $E/N = 10\,Td$ and around $E_{coll} \approx 1.9\,eV$ for $E/N = 100\,Td$. This means that the average collision energy at which collisions occur in electric fields where perfect agreement is found between theoretical and experimental mobility values falls within the region where a similar agreement is found for cross sections.

In [276], we have found that the effect of initial rotational and (or) vibrational excitations in the N_2^+ ion (prior to its collision with a helium atom) is only marginal in the NRS process (Equation (2.72)), even for quite high excitations (j=0,v=10). Somewhat better pronounced changes upon considering rotationally and/or vibrationally excited N_2^+ ions have been observed for the CID (Equation (2.73)) cross-sections. Here, we analyze how the N_2^+ rotational-vibrational excitations influence the transport properties of the ion and its CID rate. A comprehensive picture is provided in Figure 4.33 where the same rotational and vibrational excitations of the N_2^+ ion are included as those considered in cross-section calculations [276].

To illustrate expected uncertainties of transport data due to the use of either type 1 or type 2 MTCSs (Equation (2.74) and Equation (2.75), respectively), differences in the N_2^+ mobility calculated using the two types of MTCS are depicted in Figure 4.34. This figure leads to a similar conclusion as for the cross-sections [276], the differences are generally insignificant (up to 1 %) for all N_2^+ rotational and vibrational excitations and in the entire range of electric

field reduction.

Finally, for the N_2^+ mobility in He , the effect of J alignment can be seen in Figure 4.36 considering perpendicular (PES), parallel (PAR), and unaligned (NA) configurations. Here, the values obtained for the PER J alignment are at most 8 % above the NA values, and the values resulting from the PAR alignment are almost the same (relative) deviations reduced with respect to the NA value. Fairly significant PER/PAR/NA differences can be seen in the D_L/D_T curves shown in the middle panel Figure 4.36. While a marginal difference (up to 1 %) is obtained in the weak field region ($E/N \approx 1$–10 Td), it gradually increases with increasing electric field strength.

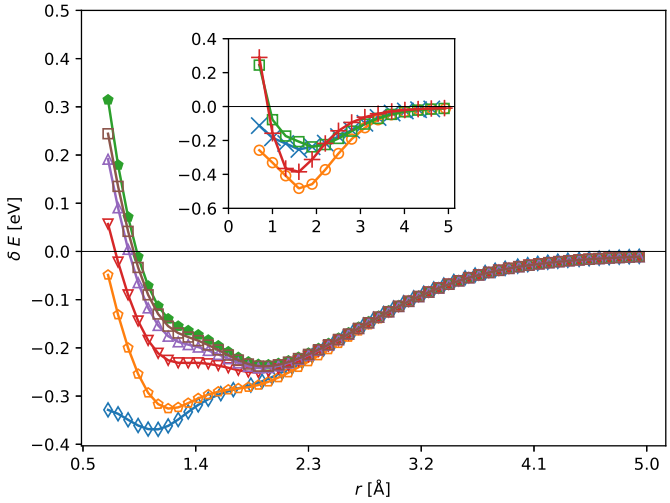

Figure 4.8: Differences between MCSCF and MRCI calculations (MCSCF −MRCI) performed for the $X\,^2\Sigma_g^+$ state of the N_2^+ ion at the OS2 level: diamonds/blue AVTZ, down triangles/red AVQZ, up triangles/violet AV5Z, and squares/brown AV6Z. Values obtained for the AVQZ′ basis set (empty pentagons/orange)and difference with MRCI/AV6Z (full pentagons/green) are also shown for comparison. In the inset, the evolution of calculated differences with the orbital space is shown as obtained for the largest basis set used in this work (AV6Z): pluses OS1, squares OS2, circles OS3, and times OS4. All the energies are set to zero as r approaches infinity.

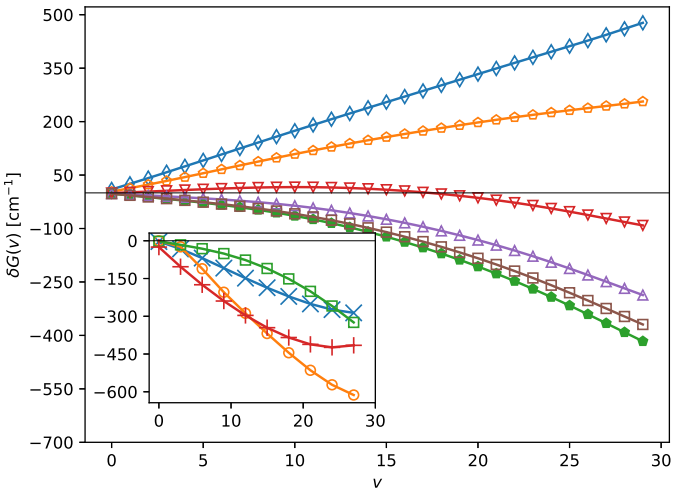

Figure 4.9: Differences between MCSCF and MRCI calculations (MCSCF −MRCI) of the lowest vibrational levels of N_2^+ performed for the $X\,^2\Sigma_g^+$ state of the ion. The symbols used are the same as in Figure 4.8; the main panel: diamonds AVTZ, down triangles AVQZ, up triangles AV5Z, and squares AV6Z, empty pentagons AVQZ′, and full pentagons differences between MCSCF /AVQZ′ and MRCI/AV6Z (with all the calculations performed for the OS2 orbital space); the inset: pluses OS1, squares OS2, circles OS3, and times OS4 (with all the calculations performed for the AV6Z basis set).

Table 4.1: Dissociation energies for the $X\,^2\Sigma_g^+$ state of the N_2^+ ion as obtained from MCSCF (D_e^{MCSCF}) and MRCI (D_e^{CI}) calculations and absolute ($\delta D_e \equiv D_e^{MCSCF} - D_e^{CI}$) and relative ($\delta_r D_e \equiv \delta D_e / D_e^{CI}$) differences between them. The last line (denoted by "T-6") in each section contains the differences between the cheapest, MCSCF /AVTZ, and the most accurate, MRCI/AV6Z, results. For OS2, the difference between MCSCF /AVQZ′ and MRCI/AV6Z is also added (line "Q′-6") for comparison. All the energies are given in eV.

basis	D_e^{MCSCF}	D_e^{CI}	δD_e	$\delta_r D_e$
orbital space 1 (OS1)				
AVTZ	9.153	8.656	0.497	+5.7 %
AVQZ	9.208	8.860	0.348	+3.9 %
AV5Z	9.213	8.920	0.293	+3.3 %
AV6Z	9.214	8.944	0.270	+3.0 %
T-6			0.209	+2.3 %
orbital space 2 (OS2)				
AVTZ	8.976	8.608	0.368	+4.3 %
AVQZ′	9.023	8.702	0.321	+3.7 %
AVQZ	9.033	8.817	0.216	+2.5 %
AV5Z	9.038	8.877	0.16	+1.8 %
AV6Z	9.039	8.901	0.137	+1.5 %
Q′-6			0.122	+1.2 %
T-6			0.075	+0.8 %
orbital space 3 (OS3)				
AVTZ	9.169	8.599	0.570	+6.6 %
AVQZ	9.247	8.811	0.436	+5.0 %
AV5Z	9.254	8.872	0.382	+4.3 %
AV6Z	9.255	8.896	0.359	+4.0 %
T-6			0.273	+3.1 %
orbital space 4 (OS4)				
AVTZ	8.960	8.543	0.418	+4.9 %
AVQZ	9.026	8.754	0.273	+3.1 %
AV5Z	9.031	8.815	0.217	+2.5 %
AV6Z	9.033	8.839	0.195	+2.2 %
T-6			0.121	+1.4 %

Table 4.2: The same as in Table 4.1 but for the the $A\,^2\Pi_u$ electronic state of the N_2^+ ion.

basis	D_e^{MCSCF}	D_e^{CI}	δD_e	$\delta_r D_e$
orbital space 1 (OS1)				
AVTZ	8.037	7.554	0.483	+6.4 %
AVQZ	8.085	7.747	0.337	+4.4 %
AV5Z	8.089	7.805	0.284	+3.6 %
AV6Z	8.090	7.829	0.261	+3.3 %
T-6			0.208	+2.6 %
orbital space 2 (OS2)				
AVTZ	7.953	7.519	0.435	+5.8 %
AVQZ′	7.996	7.601	0.395	+5.2 %
AVQZ	8.004	7.712	0.292	+3.8 %
AV5Z	8.008	7.77	0.238	+3.1 %
AV6Z	8.009	7.793	0.216	+2.8 %
Q′-6			0.203	+2.6 %
T-6			0.160	+2.0 %
orbital space 3 (OS3)				
AVTZ	8.255	7.519	0.736	+9.8 %
AVQZ	8.316	7.715	0.601	+7.8 %
AV5Z	8.314	7.778	0.536	+6.9 %
AV6Z	8.315	7.802	0.513	+6.6 %
T-6			0.453	+5.8 %
orbital space 4 (OS4)				
AVTZ	7.939	7.466	0.473	+6.3 %
AVQZ	8.000	7.661	0.340	+4.4 %
AV5Z	8.005	7.720	0.285	+3.7 %
AV6Z	8.006	7.744	0.262	+3.4 %
T-6			0.195	+2.5 %

Table 4.3: Comparison of dissociation energy (ΔD_e) and equilibrium distance between the center-of-mass of the N_2^+ ion and the He atom (R_e) calculated for the electronic ground state ($1A'$) of N_2^+/He and for selected Jacobi angles (θ) and using different levels of *ab initio* calculations. The distance of atoms in N_2^+ has been fixed in all calculations at $r = 2.11$ Bohr (≈ 1.117 Å). If not specified otherwise, data obtained within the present work are presented. The data reported for reference [283] have been extracted from figure 1 of that reference. Distances and binding energies are given in Å and meV, respectively.

	$\theta = 0°$		$\theta = 45°$		$\theta = 90°$	
method	R_e	ΔD_e	R_e	ΔD_e	R_e	ΔD_e
MCSCF	3.400	11.8	3.226	12.2	3.088	11.4
MRCI	3.227	19.3	3.034	20.1	2.879	19.2
MRCI [26]	3.280	16.5	3.090	17.3	2.799	16.7
MRCI [30][1]	3.265	17.2	–	–	2.910	17.2
MRCI [30][2]	3.291	17.4	–	–	2.948	15.8
MRCI [283]	3.262	18.6	3.069	19.3	2.899	18.3
MRCI [27]	–	–	–	–	3.217	10.5

[1] diabatic potential, equation (13) of reference [30]

[2] vibrationally adiabatic potential, equation (14) of reference [30]

Table 4.4: Comparison of the N_2^+/He $\rightarrow$ N_2^++He dissociation energy (ΔD_e) and corresponding equilibrium values of internal coordinates of the N_2^+/He ion obtained from different *ab initio* calculations. If not specified otherwise, the values obtained within the present work using the MCSCF/AVQZ′ method are presented. The values given for reference [30], ground state, have been extracted from figure 2 of that reference and ΔD_e represents a lower estimate of the true value, the values provided for the same reference for the two excited states have been taken from reference [29]. The IM value of ΔD_e corresponds to the depth of an effective N_2^+/He interaction potential derived from measured mobility of the N_2^+ ion in helium [281] in reference [275]. Angles, distances, and binding energies are given in degrees, Å, and meV, respectively.

method	θ_e	R_e	r_e	ΔD_e
ground state (1A′)				
MCSCF	49	3.209	1.122	12.1
MRCI	52	2.999	1.120	20.3
MRCI [30]	51	3.064	1.117[1]	$\gtrsim$ 17.9
MRCI [27]	90	3.217	1.117[1]	10.5
IM [275]				17.3
excited state (2A′)				
MCSCF	90	2.724	1.180	21.7
MRCI	90	2.476	1.178	38.9
MRCI [30]	90	2.500	1.117[1]	36.9
excited state (1A″)				
MCSCF	90	3.144	1.179	11.2
MRCI	90	3.009	1.178	18.0
MRCI [30]	90	2.949	1.117[1]	17.0

[1] fixed at $r_e = 2.11$ bohr

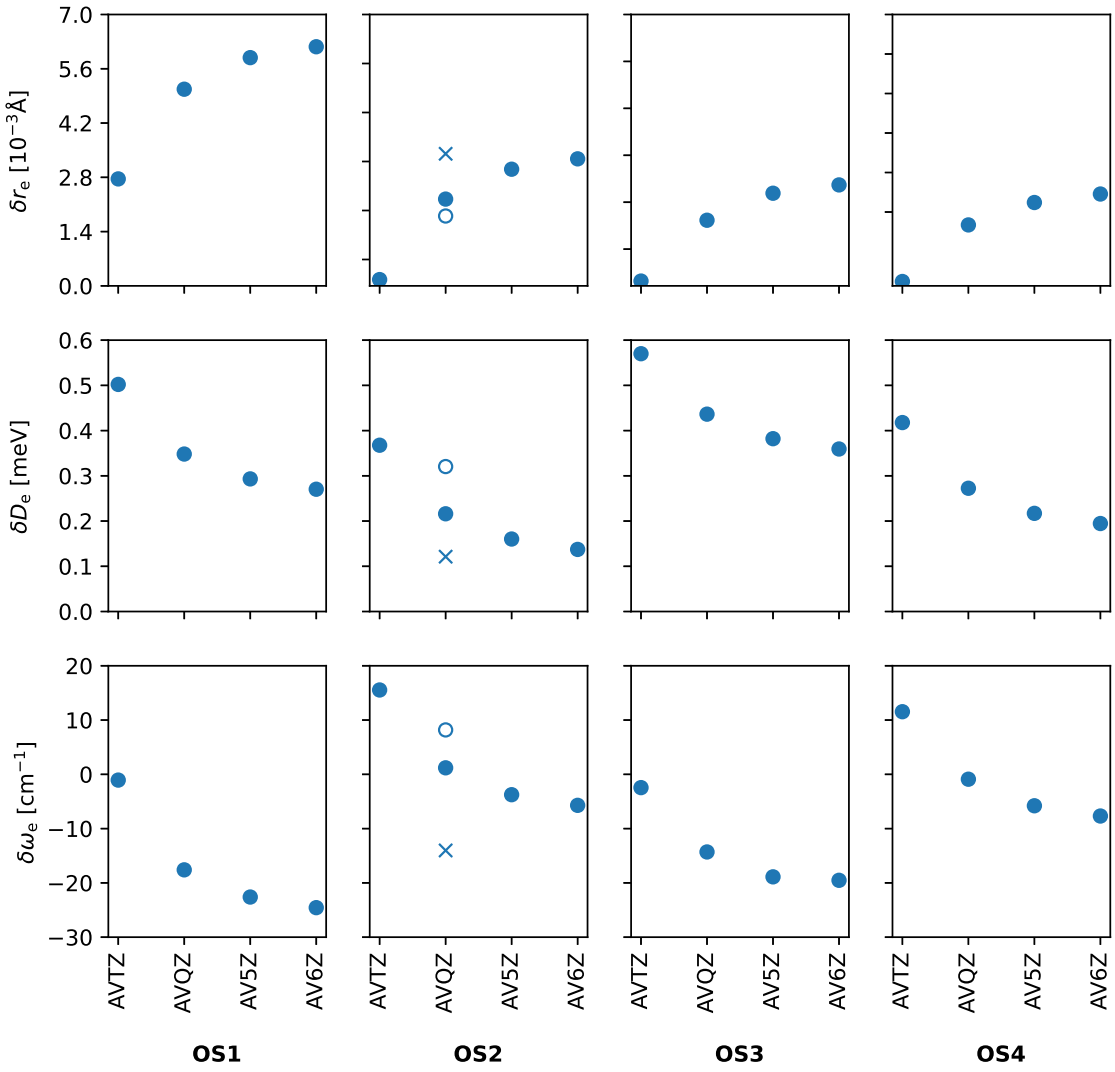

Figure 4.10: Differences of the N_2^+ binding energy, D_e, bond length, r_e, and harmonic vibrational frequency, ω_e as obtained for the $X\,^2\Sigma_g^+$ state of the ion from MCSCF and MRCI calculations (MCSCF −MRCI). Full dots correspond to calculations performed using the same basis set for both MCSCF and MRCI, open dots in the OS2 panels represent, for comparison, differences obtained for the AVQZ′ basis set, and crosses are used to show differences of MCSCF /AVQZ′−MRCI/AV6Z.

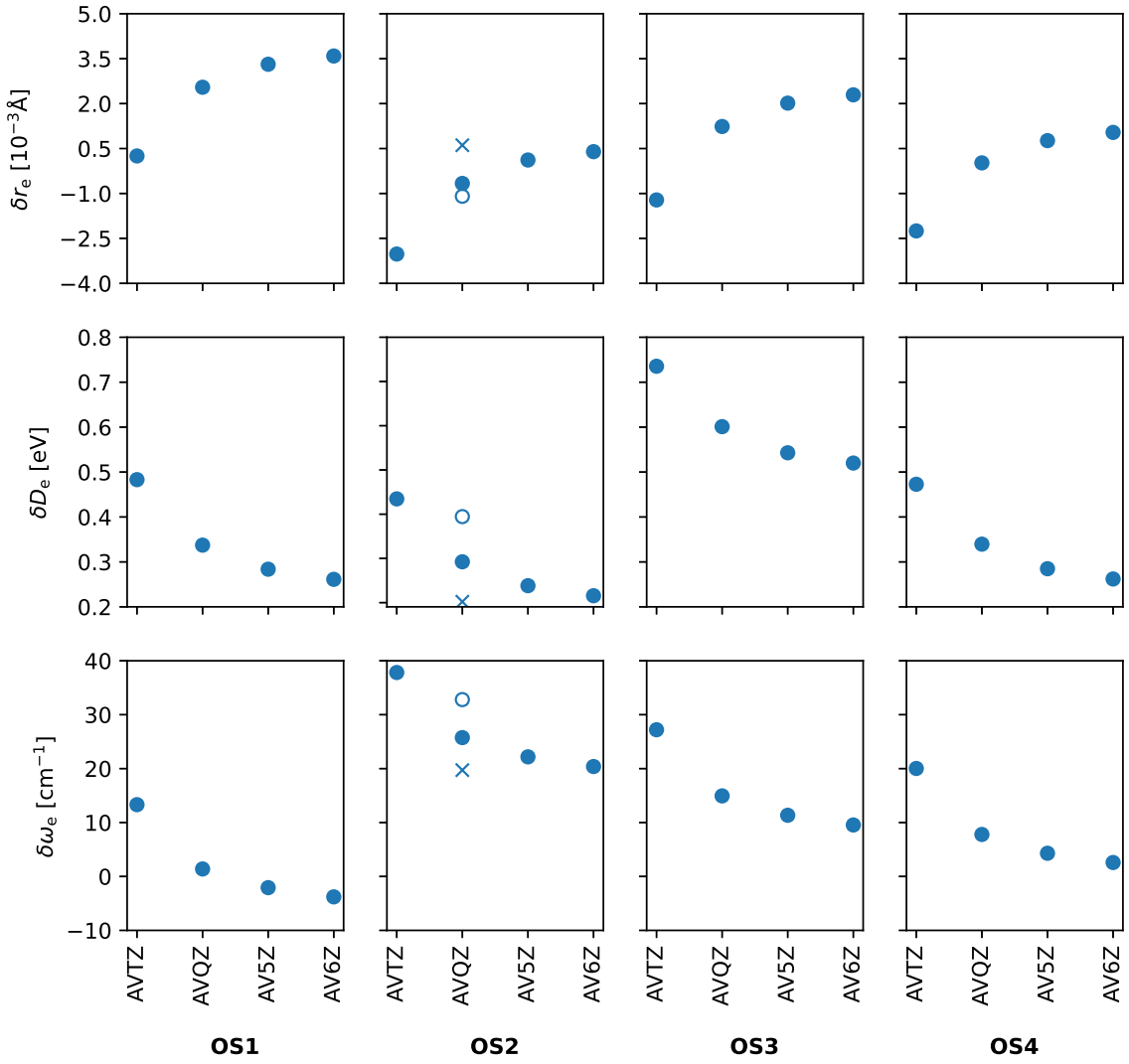

Figure 4.11: The same as in Figure 4.10, but for the A $^2\Pi_u$ state of the N_2^+ ion.

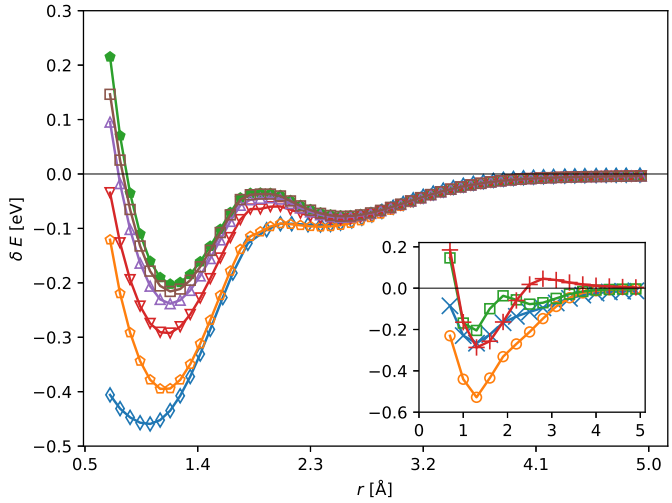

Figure 4.12: The same as in Figure 4.8, but for the A $^2\Pi_u$ state of the N_2^+ ion.

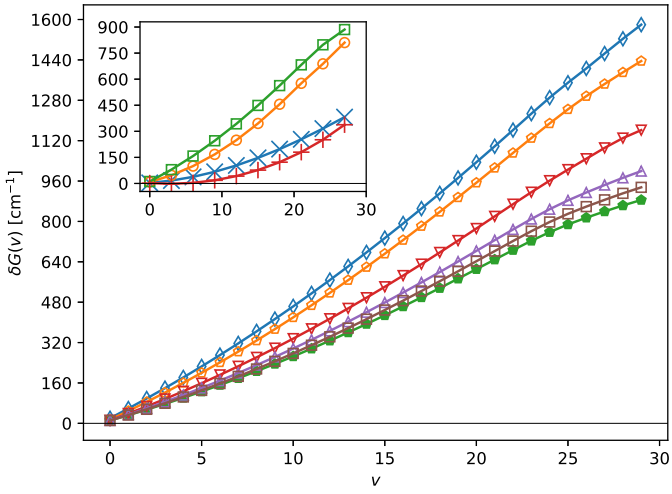

Figure 4.13: The same as in Figure 4.9, but for the A $^2\Pi_u$ state of the N_2^+ ion.

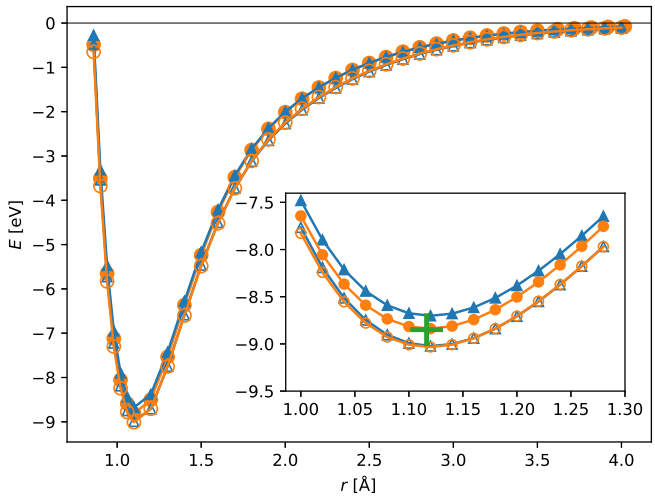

Figure 4.14: Comparison of MCSCF (empty symbols) and MRCI (full symbols) PECs calculated for the $X\,^2\Sigma_g^+$ state of the N_2^+ ion using AVQZ′/OS2 (blue triangles) and AV6Z/OS4 (orange circles). In the inset, a magnified view of the vicinity of the PEC minimum is depicted. The experimental value of the potential energy minimum (green plus) is taken from reference [274].

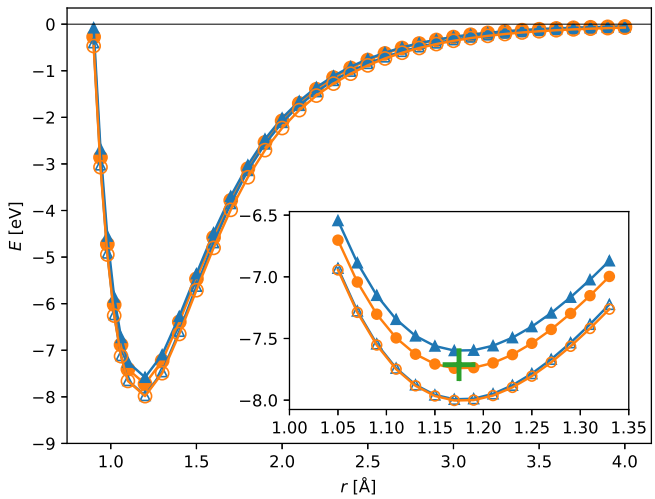

Figure 4.15: The same as in Figure 4.14, but for the $A\,^2\Pi_u$ state of the N_2^+ ion.

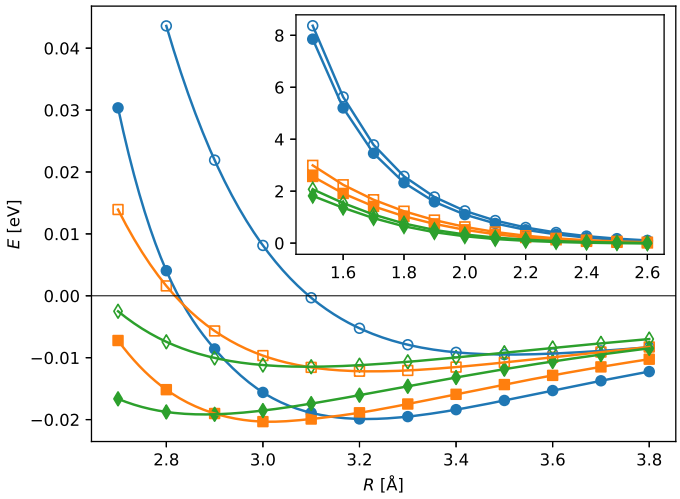

Figure 4.16: 1D cuts of the MCSCF (empty symbols) and MRCI (full symbols) PESs computed for the electronic ground state ($1A'$) of the N_2^+/He ion with the distance of nitrogen atoms fixed at $r = 1.1166$Å and for selected Jacobi angles, $\theta = 1°$ (blue circles), $\theta = 45°$ (orange squares), and $\theta = 90°$ (green diamonds). In the inset, the short-distance, repulsive walls of the calculated curves are depicted.

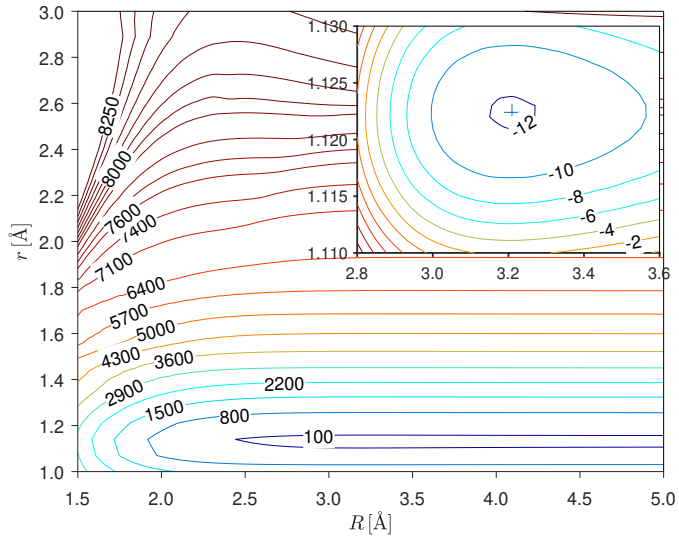

Figure 4.17: Contour plot of the N_2^+/He ground state PES ($1A'$) as obtained for the MC-SCF/AVQZ′ method around its global minimum. Energies are given in meV and the asymptote corresponds to the N_2^+(equ) + He dissociated state (where "equ" indicates that the equilibrium distance of nitrogen atoms is considered as obtained at the same level of theory for the $N_2^+(X\,^2\Sigma_g^+)$ ion). A magnified view of the PES minimum is shown in the inset.

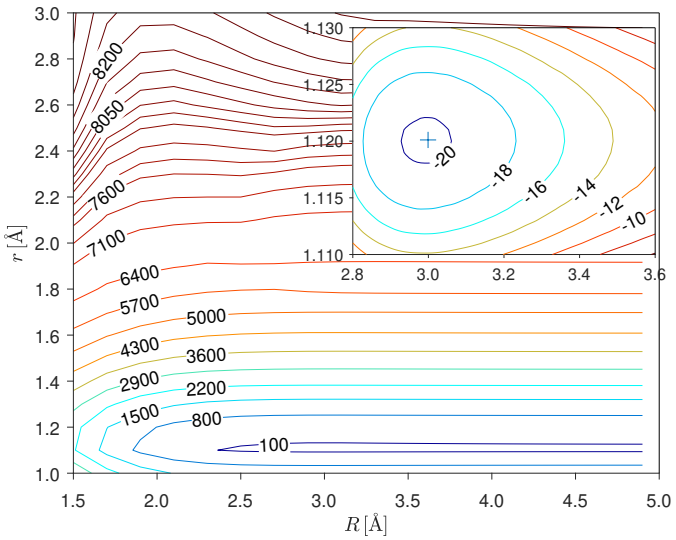

Figure 4.18: The same as in Figure 4.17, but calculated at the MRCI/AVQZ′ level.

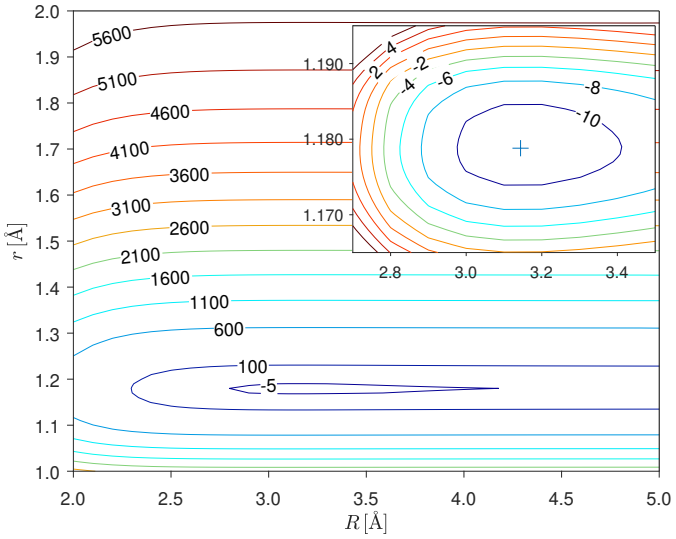

Figure 4.19: Contour plot of the N_2^+/He lowest PES of the $1A''$ symmetry as obtained for the MCSCF/AVQZ′ method. Like in Figure 4.17, energies are given in meV and the asymptote corresponds to the $N_2^+(\text{equ}) + \text{He}$ dissociated state.

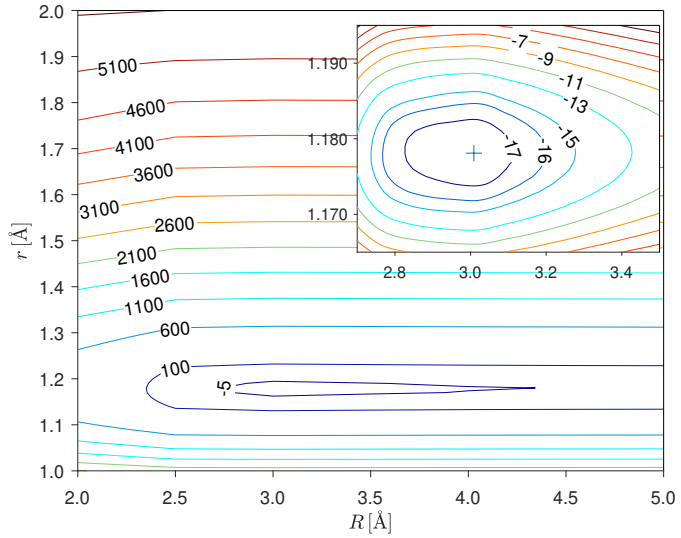

Figure 4.20: The same as in Figure 4.19, but calculated at the MRCI/AVQZ′ level.

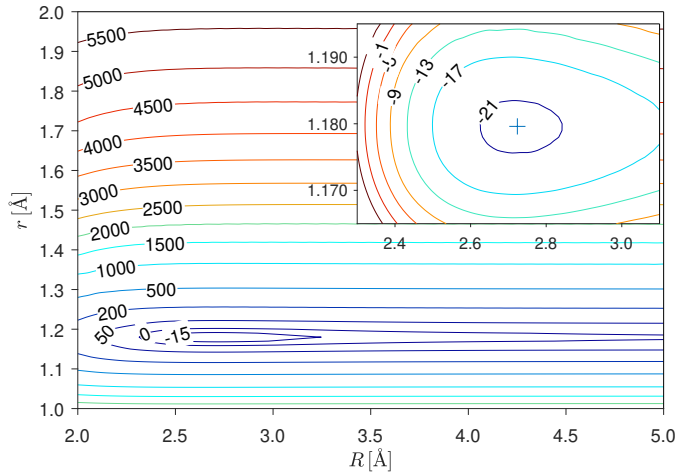

Figure 4.21: Contour plot of the lowest excited PES of the N_2^+/He ion in the A' symmetry ($2A'$) as obtained for the MCSCF/AVQZ′ method. Energies are given in meV, the asymptote corresponds to the N_2^+(equ) + He dissociated state.

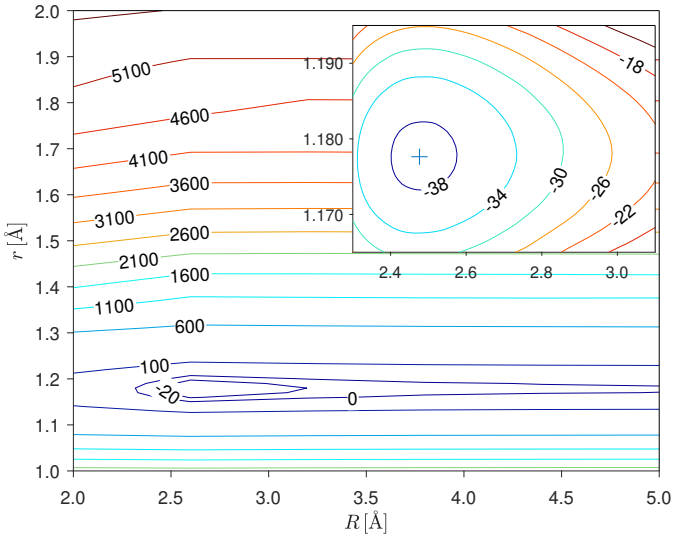

Figure 4.22: The same as in Figure 4.21, but calculated at the MRCI/AVQZ′ level.

Figure 4.23: Type 1 momentum-transfer cross-sections calculated from selected experimental mobility data via the inverse-method (IM) approach: full line – IM cross-sections obtained from mobility data given in [278] (as reported in [281]), dashed line – IM cross-sections based on the mobilities of [279], and dash-dotted line – IM cross-sections based on [280]. In the inset, related experimental mobilities are provided for comparison (circles [278], up triangles [279], and down triangles [280]) together with their IM representations (using the same line patterns as in the main panel.)

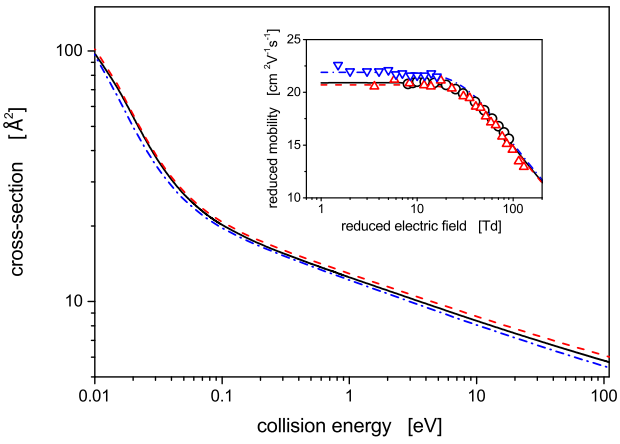

Figure 4.24: Type 1 momentum-transfer cross-sections of $N_2^+(j,v) + He \rightarrow N_2^+ + He$ collisions as calculated for selected rotational-vibrational states of the N_2^+ ion at the MCSCF/AVQZ′ level: full circles j=0,v=0, upper half-filled circles j=0,v=1, lower half-filled circles j=0,v=10, and open circles j=36,v=0. Inverse-method values derived from selected experimental data are also included as gray lines in the background (with the line patterns used as in Figure 4.23). In the inset, differences from values obtained for j=0,v=0 are depicted.

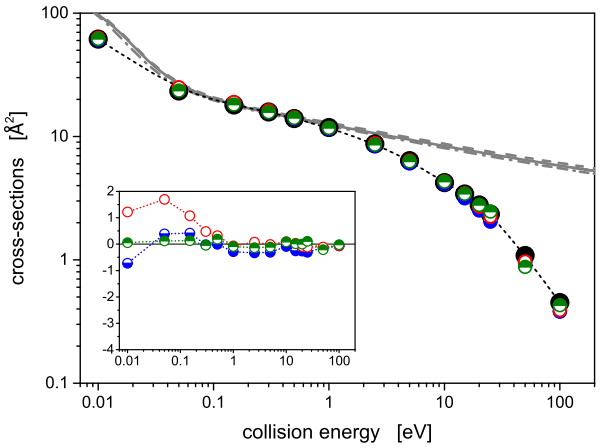

Figure 4.25: Contributions of particular impact-parameters to type 1 momentum-transfer cross-sections, $2\pi b \Delta\sigma_{\mathrm{NRS}}^{(\mathrm{MT1})}(b)$, of $N_2^+(j=0, v=0) + He \rightarrow N_2^+ + He$ collisions as calculated at the MCSCF/AVQZ′ level for selected collision energies: full line $E_{\mathrm{coll}} = 0.01\,\mathrm{eV}$, dashed line $E_{\mathrm{coll}} = 0.05\,\mathrm{eV}$, and dash-dotted line $E_{\mathrm{coll}} = 0.15\,\mathrm{eV}$.

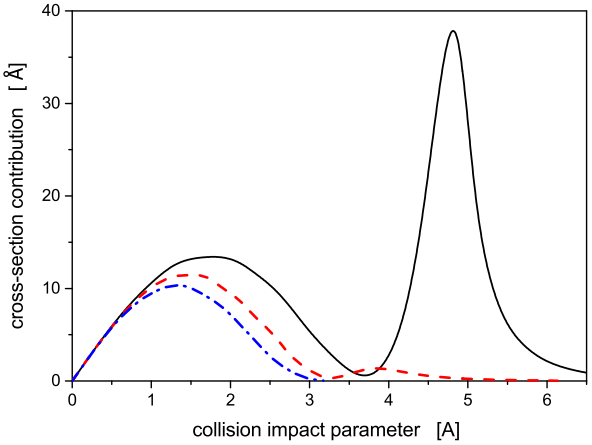

Figure 4.26: Deviations between type 2 and type 1 momentum-transfer cross-sections of the NRS channel (Equation (2.72)) as calculated at the MCSCF/AVQZ(spdf) level for selected rotational-vibrational states of the N_2^+ ion. The symbols used are the same as in Figure 4.24, the connecting lines are added to guide eyes.

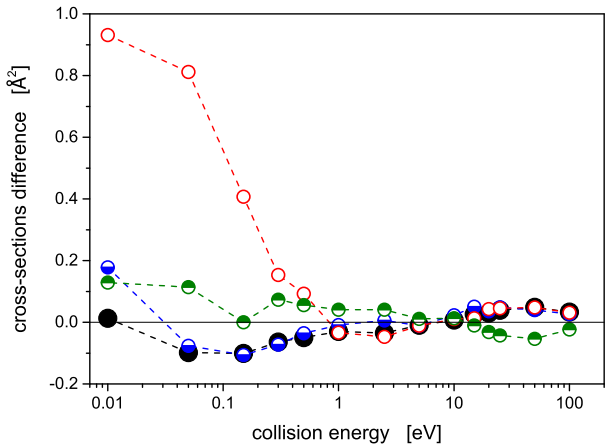

Figure 4.27: The same as in Figure 4.24, but for the collision-induced dissociation cross-sections (Equation (2.73)).

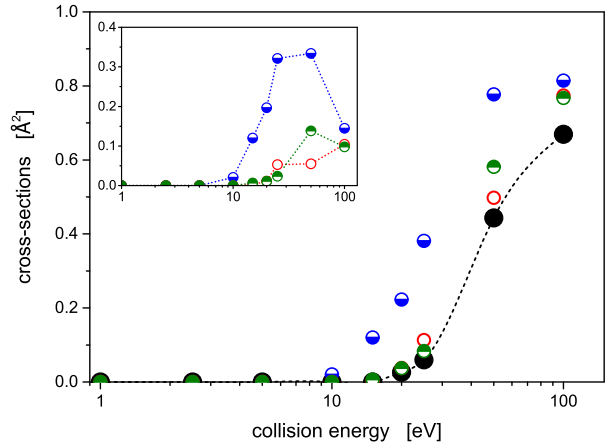

Figure 4.28: Comparison of type 1 momentum-transfer cross-sections and dissociation cross-sections as obtained for $N_2^+(j{=}0,v{=}0)$/He collisions via the MCSCF/AVQZ(spdf) method (full and open circles, respectively) and using artificial neural network (ANN) representations of the N_2^+/He potential energy surface (pluses and crosses, respectively). In the inset, deviations between the ANN and MCSCF/AVQZ(spdf) data are depicted.

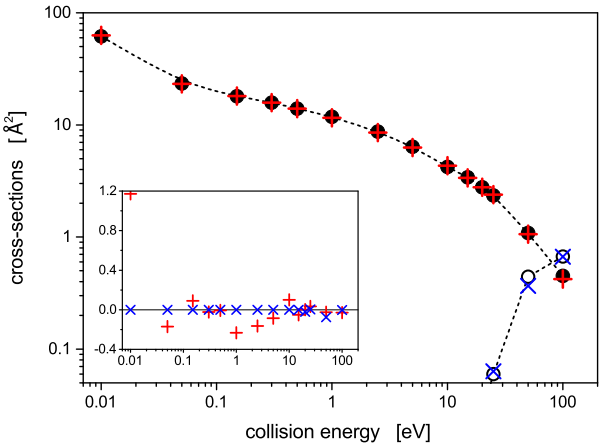

Figure 4.29: Comparison of type 1 momentum-transfer cross-sections (circles) and collision-induced dissociation cross-sections (diamonds) as obtained for $N_2^+(j{=}0,v{=}0)$/He collisions assuming angular momentum of N_2^+ perpendicularly (PER) and/or parallelly (PAR) aligned to the collision axis (open symbols), and non-aligned (full symbols). For comparison, inverse-method cross-sections are also depicted as grey lines in the background. In the inset, deviations of the PER/PAR cross-sections from the cross-sections calculated for non-aligned N_2^+ are depicted.

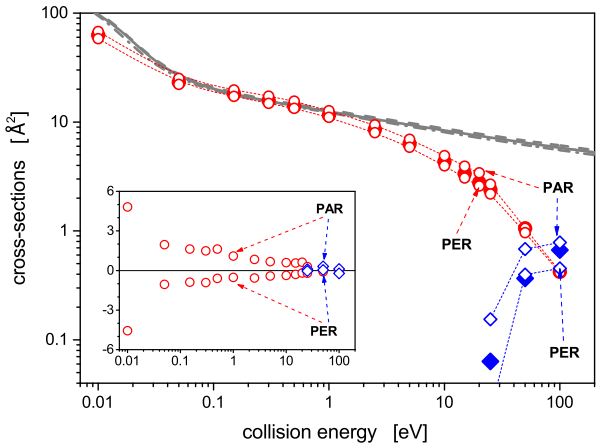

Figure 4.30: Selected experimental data on the mobility of N_2^+ in He: diamonds [282], circles [278] (as reported in [281]), up triangles [279], and down triangles [280]. For comparison, inverse-method representations of selected experimental data are also included: full line [278], dashed line [279], and dash-dotted line [280].

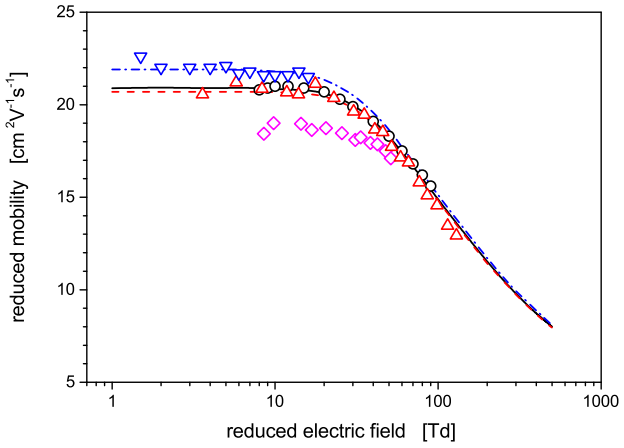

Figure 4.31: Reduced mobilities (upper panel) and longitudinal and transversal characteristic diffusion energies (lower panel, circles and triangles, respectively) of the N_2^+ ion in helium gas as calculated for the rotational-vibrational ground state of the ion (j=0,v=0) at the MCSCF/AVQZ(spdf) level of theory (full symbols). Inverse-method (IM) values derived from selected experimental data are also included as gray lines in the background with the line patterns used as in Fig. 4.30. For comparison, data resulting from an independent mobility calculation reported in the literature [284] are also shown in the upper panel (pluses). In the inset of the lower panel, a detailed view of the weak-field region is shown.

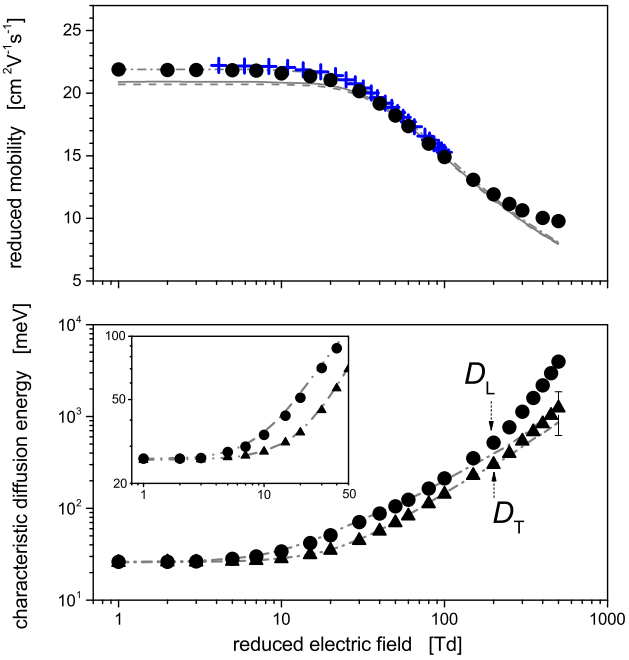

Figure 4.32: Distributions of center-of-mass collision energies of $N_2^+(j{=}0,v{=}0)$/He as calculated for selected values of the reduced electric field using type 1 momentum-transfer cross-sections. The distributions have been normalized so that they have the same heights in their maxima.

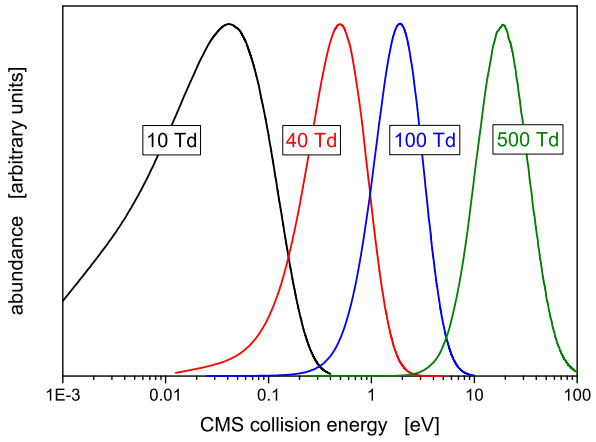

Figure 4.33: Reduced mobility (upper panel), longitudinal and transversal characteristic diffusion energies (middle panel, circles and triangles, respectively), and CID rate constants of N_2^+ ions in helium gas as calculated for selected rotational-vibrational states of the ion at the MCSCF/AVQZ(spdf) level: full symbols j=0,v=0, upper half-filled symbols j=0,v=1, lower half-filled symbols j=0,v=10, and open symbols j=36,v=0. Inverse-method values derived from the most recent mobility measurements [280] are also included as dash-dotted gray lines for comparison. In the insets, deviations from the j=0,v=0 data are depicted to better see the effect of rotational-vibrational excitations in the N_2^+ ion. Note that different scales are used on the horizontal axes in the two upper panels and the lower panel.

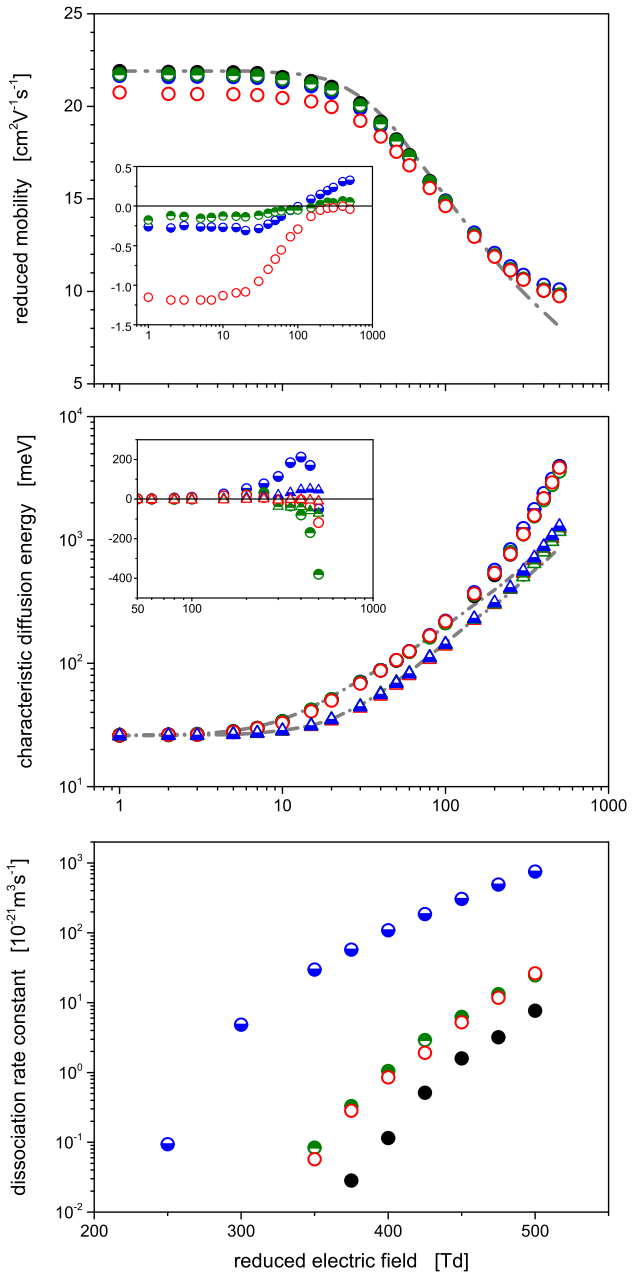

Figure 4.34: Deviations of N_2^+/He mobilities calculated using type 2 momentum-transfer cross-sections from the values obtained from type 1 cross-sections, both calculated for selected rotational-vibrational states of the N_2^+ ion at the MCSCF/AVQZ(spdf) level. The symbols used are the same as in Fig. 4.33, the connecting lines are added to guide eyes.

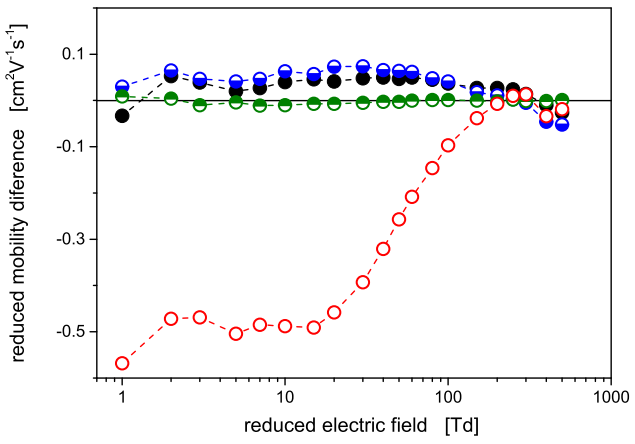

Figure 4.35: Comparison of N_2^+/He mobilities calculated using type 1 momentum-transfer cross-sections (and dissociation cross-sections) as obtained from MCSCF/AVQZ(spdf) calculations (full circles) and using an artificial neural network (ANN) representation of the N_2^+/He PES (pluses). In the inset, deviations between the ANN and MCSCF/AVQZ(spdf) data are depicted.

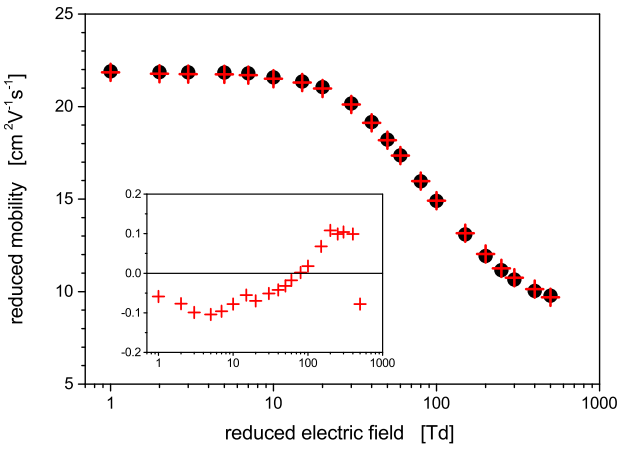

Figure 4.36: Comparison of N_2^+/He mobilities (upper panel), longitudinal and transversal characteristic diffusion energies (middle panel, circles, and triangles, respectively), and CID rate constants of N_2^+ ions in helium gas calculated for rotationally-vibrationally ground-state N_2^+ ion using cross-sections obtained at the ANN level and assuming the angular momentum of the N_2^+ ion aligned perpendicularly (open circles with vertical bars, PER) and/or parallel (open circles with horizontal bars, PAR) to the collision axis, and non-aligned (full symbols). For comparison, inverse-method mobilities derived from experimental data are also depicted as grey lines in the background (with the same line patterns used as in Fig. 4.30). In the inset, deviations of the aligned angular momentum cross-sections from non-aligned cross-sections are depicted. Note that, like in Fig 4.33, different scales are used on the horizontal axes in the two upper panels and the lower panel.

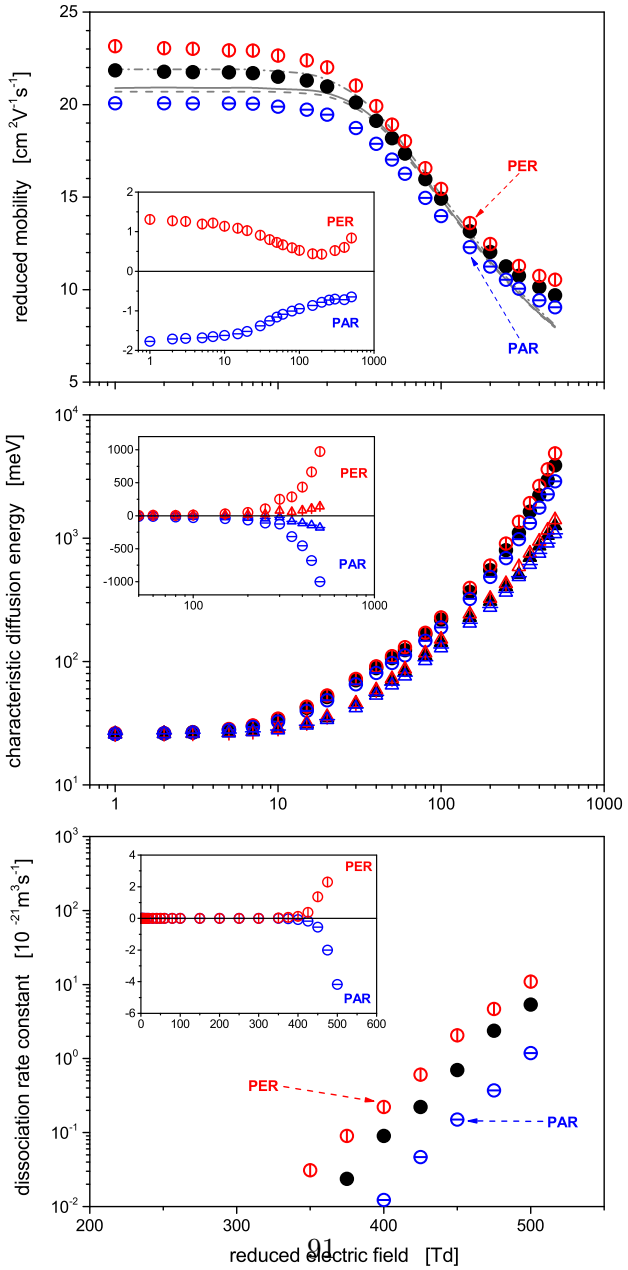

Chapter 5

Summary and Outlooks

Ab initio computations of both the N_2^+ ion and N_2^+/He collision complex have been performed,with MCSCF data further utilized for as the input for dynamical calculations [276], exhibiting a very good agreement with N_2^+/He mobility measurements. Furthermore, the results were excellent, well reproducing available experimental results, even in the follow-up phase, i.e. Monte Carlo mesoscopic modeling of N_2^+/He complex [277].

Thus, it seems, that the effects not taken into account in the adopted *ab initio* approach based on the MCSCF method do not influence the N_2^+/He collision dynamics too much, with the exception of low collision energies [276], approximately 0.01 eV. For them, on the other hand, the missing dynamical electronic correlation in the MCSCF method is important and maybe it will be a cause of significant differences between theoretical and experimental estimates of N_2^+/He collision cross-sections [276]. While such low collision energies are not typically recognized at standard experimental conditions (T = 300 K), they may prove to be important, thus it is one of the continuing research interests. Without sufficiently-deep investigation we assume so far, that a multi-reference perturbative method, like MRPT2 [285] may be useful in on-the-fly simulations, thus aiming for direct comparison of its results with ANN-represented MRCI PES.

With that said, the absence of dynamical electronic correlation is not the only issue, connected to N_2^+/He complex, necessary to investigate in deeper detail. The question of the exact effect of electronic excitations and non-adiabatic processes on collision dynamics is one of them. In this direction, we aim to utilize an approximately diabatic interaction model invented in [30], for the description of the behavior of the lowest N_2^+/He electronic states $2 \times A' + A''$. Similarly, the relaxation of initial rotational-vibrational excitations of N_2^+ cation and its influence on dynamical simulations is also not very clear for now. With that in mind, we aim to describe its effects in more detail in the following works, too, planning to research their presence in N_2^+ cation, as the first step.

As a direct continuation of the current results, we also aim to utilize ANNs to represent MRCI PESs, thus obtaining potential energy with higher precision. These will be created for not only the ground and the first excited states, but even for higher excited states, together with a description of the charge transfer $N_2 + He^+ \rightarrow N_2^+ + He$. In these efforts, the molecular ions He_2^+ and He_3^+ will not be omitted, modelling the collision complexes $[N_2/He_2]^+$ and $[N_2/He_3]^+$.

Finally, considering the practical problems (leakage, explosiveness...) with applications of He, it is vital to consider also heavier rare gases, most notably Ar, Kr and Xe. For these, the interactions of molecular ions are more prominent and the for the heavier elements it will be necessary to include relativistic effects in computations. Namely, we consider utilization of scalar relativistic corrections [286] and computations of spin-orbital coupling [287].

Bibliography

[1] Junggil Kim et al. “Discharge characteristics and plasma erosion of various dielectric materials in the dielectric barrier discharges”. In: *Applied Sciences* 8.8 (2018), p. 1294. DOI: 10.3390/app8081294.

[2] Brendan A Niemira. “Cold plasma decontamination of foods”. In: *Annual review of food science and technology* 3 (2012), pp. 125–142. DOI: 10.1146/annurev-food-022811-101132.

[3] Dana Ziuzina et al. “Atmospheric cold plasma inactivation of E scherichia coli in liquid media inside a sealed package”. In: *J. Appl. Microbiol* 114.3 (2013), pp. 778–787. DOI: 10.1111/jam.12087.

[4] Meral Selcuk, Lutfi Oksuz, and Pervin Basaran. “Decontamination of grains and legumes infected with Aspergillus spp. and Penicillum spp. by cold plasma treatment”. In: *Bioresour. Technol.* 99.11 (2008), pp. 5104–5109. DOI: 10.1016/j.biortech.2007.09.076.

[5] Sun Mujin et al. “The surface of carbon fibres continuously treated by cold plasma”. In: *Compos. Sci. Technol.* 34.4 (1989), pp. 353–364. DOI: 10.1016/0266-3538(89)90004-3.

[6] Luigi Carrino, Giovanni Moroni, and Wilma Polini. “Cold plasma treatment of polypropylene surface: a study on wettability and adhesion”. In: *J. Mater. Process. Technol.* 121.2-3 (2002), pp. 373–382. DOI: 10.1016/S0924-0136(01)01221-3.

[7] Alfred Grill. *Cold plasma in materials fabrication*. Vol. 151. IEEE Press, New York, 1994. DOI: 10.1109/9780470544273.

[8] K. D. Weltmann and Th Von Woedtke. “Plasma medicine—current state of research and medical application”. In: *Plasma Phys. Control. Fusion* 59.1 (2016), p. 014031. DOI: 10.1088/0741-3335/59/1/014031.

[9] Christoph V. Suschek and Christian Opländer. “The application of cold atmospheric plasma in medicine: the potential role of nitric oxide in plasma-induced effects”. In: *Clin. Plasma Med.* 4.1 (2016), pp. 1–8. DOI: 10.1016/j.cpme.2016.05.001.

[10] K.-D. Weltmann, H.-R. Metelmann, and Th von Woedtke. "Low temperature plasma applications in medicine". In: *Europhys. News* 47.5-6 (2016), pp. 39–42. DOI: 10.1051/epn/2016507.

[11] Adam M. Hirst et al. "Low temperature plasmas as emerging cancer therapeutics: the state of play and thoughts for the future". In: *Tumor Biol* 37.6 (2016), pp. 7021–7031. DOI: 10.1007/s13277-016-4911-7.

[12] GZ Yin, QW Tan, and ZA Wei. "Combined optimization model of rock-burst prediction based on chaos optimization and BP neural networks [J]". In: *Journal of China Coal Society* 33.8 (2008), pp. 871–875.

[13] Mohammed Yousfi et al. "Low-temperature plasmas at atmospheric pressure: toward new pharmaceutical treatments in medicine". In: *Fundamental & clinical pharmacology* 28.2 (2014), pp. 123–135.

[14] Shashi K. Pankaj and Kevin M. Keener. "Cold plasma: Background, applications and current trends". In: *Curr. Opin. Food Sci.* 16 (2017), pp. 49–52. DOI: 10.1016/j.cofs.2017.07.008.

[15] John Sealy Edward Townsend. "IV. The diffusion of ions into gases". In: *Philosophical Transactions of the Royal Society of London. Series A, Containing Papers of a Mathematical or Physical Character* 193 (1900), pp. 129–158.

[16] Urszula Czuba et al. "Atmospheric plasma deposition of methacrylate layers containing catechol/quinone groups: An alternative to polydopamine bioconjugation for biomedical applications". In: *Adv. Healthcare Mater.* 7.11 (2018), p. 1701059. DOI: 10.1002/adhm.201701059.

[17] Y Irani et al. "Noble gas (argon and xenon)-saturated cold storage solutions reduce ischemia-reperfusion injury in a rat model of renal transplantation". In: *Nephron Extra* 1.1 (2011), pp. 272–282. DOI: 10.1159/000335197.

[18] Cyril Van de Steen et al. "Calculations with experimental validations of cross-sections and transport coefficients of Xe+ colliding with Xe". In: *J. Phys. B: At. Mol. Opt. Phys.* 51.18 (2018), p. 185204. DOI: 10.1088/1361-6455/aad92a.

[19] Malika Benhenni et al. "Transport and dissociation of neon dimer cations in neon gas: a joint dynamical and Monte Carlo modeling". In: *Journal of Physics B: Atomic, Molecular and Optical Physics* 49.17 (2016), p. 175205. DOI: 10.1088/0953-4075/49/17/175205.

[20] Shuji Kato, Veronica M. Bierbaum, and Stephen R. Leone. "Laser fluorescence and mass spectrometric measurements of vibrational relaxation of N2+(v) with He, Ne, Ar, Kr, and Xe". In: *International Journal of Mass Spectrometry and Ion Processes* 149-150 (Nov. 1995), pp. 469–486. ISSN: 0168-1176. DOI: 10.1016/0168-1176(95)04283-Q. URL: https://linkinghub.elsevier.com/retrieve/pii/016811769504283Q (visited on 04/11/2020).

[21] M Gochitashvili et al. "Polarization measurements in He+-N2 collisions". In: *Georgian Electron. Sci. J.(GESF): Phys.* 1 (2004), pp. 151–161.

[22] William B Maier II. "Reactions of He+ with N2 and O2 in the upper atmosphere". In: *Planetary and Space Science* 16.4 (1968), pp. 477–493. DOI: 10.1016/0032-0633(68)90162-1.

[23] Andrey E Belikov. "Rotational and vibrational excitation of the (B) state in a He + N 2 electron-beam plasma". In: *Chemical Physics* (1997), p. 13.

[24] S De Benedictis, G Dilecce, and M Simek. "Vibrational excitation of N $_2$ $^+$ (B, nu) in He-N $_2$ pulsed RF discharges". In: *J. Phys. B: At. Mol. Opt. Phys.* 27.3 (Feb. 14, 1994), pp. 615–632. ISSN: 0953-4075, 1361-6455. DOI: 10.1088/0953-4075/27/3/025. URL: http://stacks.iop.org/0953-4075/27/i=3/a=025?key=crossref.5108ea26150202924abb1b4c0c7080a2 (visited on 04/03/2020).

[25] E. J. Bieske et al. "Spectroscopy and dynamics of ionic complexes: N2+-He and N2O+-Ar". In: OE/LASE'93: Optics, Electro-Optics, & Laser Applications in Science& Engineering. Ed. by Cheuk Yiu Ng. Los Angeles, CA, Apr. 22, 1993, pp. 83–91. DOI: 10.1117/12.143118. URL: http://proceedings.spiedigitallibrary.org/proceeding.aspx?articleid=1005886 (visited on 04/06/2020).

[26] Steven Miller et al. "Ab initio investigation of the bound rovibrational states in the electronic ground state of HeN_2^+". In: *J. Chem. Phys* 89.4 (1988), pp. 2178–2184. DOI: 10.1063/1.455062.

[27] G. Guillon and T. Stoecklin. "A comparative nearside-farside analysis of the $He - N_2^+$ and $He - N_2$ inelastic collisions". In: *Eur. Phys. J. D* 39.3 (Sept. 2006), pp. 359–371. ISSN: 1434-6060, 1434-6079. DOI: 10.1140/epjd/e2006-00120-5. (Visited on 04/03/2020).

[28] David F R Brown, Jonathon K Gregory, and David C Clary. "A method to calculate vibrational frequency shifts in heteroclusters: Application to N2 +-He," in: (), p. 5.

[29] T. Schmelz et al. "Bound rovibronic levels of the $HeN_2^+(A^2\Pi)$ complex". In: *Spectrochimica Acta Part A: Molecular and Biomolecular Spectroscopy.* Ab Initio and Ab Initio Derived Force Fields: State of the Science 53.8 (July 30, 1997), p. 1133. ISSN: 1386-1425. DOI: https://doi.org/10.1016/S1386-1425(97)00021-8. URL: http:

//www.sciencedirect.com/science/article/pii/S1386142597000218 (visited on 04/11/2020).

[30] Andreas Berning and Hans-Joachim Werner. "Quantum scattering studies of electronically inelastic collisions of $N_2^+(X^2\Sigma_g^+, A^2\Pi_u)$ with He". In: *The Journal of Chemical Physics* 100.3 (Feb. 1994), pp. 1953–1967. ISSN: 0021-9606, 1089-7690. DOI: 10.1063/1.466548. (Visited on 10/02/2019).

[31] M. Gerard-Aïn et al. "Theoretical study of the $He^+ + N_2 \rightarrow He + N_2^+(C)$ reaction". In: *International Journal of Mass Spectrometry and Ion Physics* 47 (Feb. 1983), pp. 167–170. ISSN: 0020-7381. DOI: 10.1016/0020-7381(83)87162-9. URL: https://linkinghub.elsevier.com/retrieve/pii/0020738183871629 (visited on 04/06/2020).

[32] Eric A. Gislason and Evelyn M. Goldfield. "Theoretical analysis of the vibrational population in the $N_2^+(B^2\Sigma_u^+)$ state produced in charge-transfer collisions of $He^+ + N_2(X^1\Sigma_g^+)$". In: *Phys. Rev. A* 25.4 (Apr. 1, 1982), pp. 2002–2005. ISSN: 0556-2791. DOI: 10.1103/PhysRevA.25.2002. (Visited on 04/11/2020).

[33] M. F. Falcetta and P. E. Siska. "Theoretical study of ion–molecule potentials for He+ and Li+ with N2". In: *The Journal of Chemical Physics* 109.16 (Oct. 22, 1998), pp. 6615–6625. ISSN: 0021-9606, 1089-7690. DOI: 10.1063/1.477312. (Visited on 04/11/2020).

[34] Cyril Van de Steen. "Modeling the transport properties of molecular ions of krypton and xenon for the optimization of cold plasma generators using rare gases". PhD thesis. 2018.

[35] Cyril Van de Steen et al. "Mobility and dissociation of electronically excited ions in cold krypton plasma". In: *Plasma Sources Science and Technology* 28.9 (2019), p. 095008.

[36] Cyril Van de Steen et al. "Relaxation of electronic excitations in ions in cold krypton plasma". In: *Plasma Sources Science and Technology* 29.2 (2020), p. 025004.

[37] Lubomír Skála and Česko Akademie věd České republiky Praha. *Úvod do kvantové mechaniky*. Karolinum, 2012. ISBN: 978-80-246-2022-0.

[38] Joshua A Rackers and Jay W Ponder. "Classical Pauli repulsion: An anisotropic, atomic multipole model". In: *The Journal of chemical physics* 150.8 (2019), p. 084104. DOI: 10.1063/1.5081060.

[39] William D Callister et al. *Fundamentals of materials science and engineering*. Vol. 471660817. Wiley London, 2000.

[40] Jean-Michel Combes, Pierre Duclos, and Ruedi Seiler. "The born-oppenheimer approximation". In: *Rigorous atomic and molecular physics*. Springer, 1981, pp. 185–213. DOI: 10.1007/978-1-4613-3350-0_5.

[41] Attila Szabo and Neil S Ostlund. *Modern quantum chemistry: introduction to advanced electronic structure theory*. Courier Corporation, 2012. ISBN: 978-0486691862.

[42] Hui Liu et al. "Theoretical spectroscopic calculations on the 25 Λ–S and 66 Ω states of N2+ cation in the gas phase including the spin–orbit coupling effect". In: *Journal of Quantitative Spectroscopy and Radiative Transfer* 147 (2014), pp. 207–223.

[43] Matúš Dubecký. "Quantum Monte Carlo for Noncovalent Interactions: A Tutorial Review". In: *Acta Phys. Slovaca* 64 (2014), pp. 501–575.

[44] Clemens Carel Johannes Roothaan. "New developments in molecular orbital theory". In: *Reviews of modern physics* 23.2 (1951), p. 69. DOI: 10.1103/revmodphys.23.69.

[45] Steven E Koonin. *Computational physics: Fortran version*. CRC Press, 2018. ISBN: 0201386232. DOI: 10.1201/9780429494024.

[46] Alexander A Klyachko. "The Pauli exclusion principle and beyond". In: *arXiv preprint arXiv:0904.2009* (2009).

[47] Ilya G Kaplan. *The Pauli exclusion principle: origin, verifications, and applications*. John Wiley & Sons, 2017.

[48] WMC Foulkes et al. "Quantum Monte Carlo simulations of solids". In: *Reviews of Modern Physics* 73.1 (2001), p. 33. DOI: 10.1103/revmodphys.73.33.

[49] Anthony Stone. *The theory of intermolecular forces*. oUP oxford, 2013. DOI: 10.1093/acprof:oso/9780199672394.001.0001.

[50] Robert K Nesbet. *Variational principles and methods in theoretical physics and chemistry*. Cambridge University Press, 2002. DOI: 10.1017/cbo9780511535161.

[51] Yifan Li et al. "Variational quantum simulation for quantum chemistry". In: *Advanced Theory and Simulations* 2.4 (2019), p. 1800182. DOI: 10.1002/adts.201800182.

[52] Per-Olov Löwdin. "Correlation Problem in Many-Electron Quantum Mechanics I. Review of Different Approaches and Discussion of Some Current Ideas". In: *Advances in chemical physics* (1958), pp. 207–322. DOI: 10.1002/9780470143483.ch7.

[53] JA Pople and JS Binkley. "Correlation energies for AH n molecules and cations". In: *Molecular Physics* 29.2 (1975), pp. 599–611.

[54] Joshua W Hollett and Peter MW Gill. "The two faces of static correlation". In: *The Journal of Chemical Physics* 134.11 (2011), p. 114111. DOI: 10.1063/1.3570574.

[55] Joshua W Hollett, Laura K McKemmish, and Peter MW Gill. "The nature of electron correlation in a dissociating bond". In: *The Journal of chemical physics* 134.22 (2011), p. 224103. DOI: 10.1063/1.3599937.

[56] William A Goddard III. "Improved quantum theory of many-electron systems. II. The basic method". In: *Physical Review* 157.1 (1967), p. 81. DOI: 10.1103/physrev.157.81.

[57] Wl/odzisl/aw Duch and Geerd HF Diercksen. "Size-extensivity corrections in configuration interaction methods". In: *The Journal of chemical physics* 101.4 (1994), pp. 3018–3030. DOI: 10.1063/1.467615.

[58] Rodney J Bartlett and BARTLETT RJ. "Many-body perturbation theory and coupled cluster theory for electron correlation in molecules". In: *Annual review of physical chemistry* 32.1 (1981), pp. 359–401. DOI: 10.1146/annurev.pc.32.100181.002043.

[59] PR Taylor. *European Summer School in Quantum Chemistry*. 1994.

[60] Marcel Nooijen, KR Shamasundar, and Debashis Mukherjee. "Reflections on size-extensivity, size-consistency and generalized extensivity in many-body theory". In: *Molecular Physics* 103.15-16 (2005), pp. 2277–2298. DOI: 10.1080/00268970500083952.

[61] Jaroslaw Meller, Jean-Paul Malrieu, and Jean-Louis Heully. "Size-consistent multireference configuration interaction method through the dressing of the norm of determinants". In: *Molecular Physics* 101.13 (2003), pp. 2029–2041. DOI: 10.1080/0026897031000109329.

[62] L. Meissner. "Size-consistency corrections for configuration interaction calculations". In: *Chem. Phys. Lett.* 146.3-4 (1988), pp. 204–210. DOI: 10.1016/0009-2614(88)87431-1.

[63] Ernest R Davidson and Donald W Silver. "Size consistency in the dilute helium gas electronic structure". In: *Chemical Physics Letters* 52.3 (1977), pp. 403–406. DOI: 10.1016/0009-2614(77)80475-2.

[64] K. Jankowski, L. Meissner, and J. Wasilewski. "Davidson-type corrections for quasidegenerate states". In: *Int. J. Quantum Chem.* 28.6 (1985), pp. 931–942. DOI: 10.1002/qua.560280622.

[65] Erkki J Brändas, Leon L Combs, and Nestor S Correia. "Size consistency corrections for configurational interaction calculations". In: *International Journal of Quantum Chemistry* 21.1 (1982), pp. 259–267. DOI: 10.1002/qua.560210124.

[66] Martin Head-Gordon et al. "A doubles correction to electronic excited states from configuration interaction in the space of single substitutions". In: *Chemical Physics Letters* 219.1-2 (1994), pp. 21–29. DOI: 10.1016/0009-2614(94)00070-0.

[67] Stephen R Langhoff and Ernest R Davidson. “Configuration interaction calculations on the nitrogen molecule”. In: *International Journal of Quantum Chemistry* 8.1 (1974), pp. 61–72. DOI: 10.1002/qua.560080106.

[68] John A Pople, Martin Head-Gordon, and Krishnan Raghavachari. “Quadratic configuration interaction. A general technique for determining electron correlation energies”. In: *The Journal of chemical physics* 87.10 (1987), pp. 5968–5975. DOI: 10.1063/1.453520.

[69] Stefan Grimme, Christian Diedrich, and Martin Korth. “The Importance of Inter- and Intramolecular van der Waals Interactions in Organic Reactions: the Dimerization of Anthracene Revisited”. In: *Angewandte Chemie* 118.4 (2006), pp. 641–645. DOI: 10.1002/ange.200502440.

[70] Laimutis Bytautas, Joseph Ivanic, and Klaus Ruedenberg. “Split-localized orbitals can yield stronger configuration interaction convergence than natural orbitals”. In: *The Journal of chemical physics* 119.16 (2003), pp. 8217–8224. DOI: 10.1063/1.1610434.

[71] JP Coe and MJ Paterson. “Development of Monte Carlo configuration interaction: Natural orbitals and second-order perturbation theory”. In: *The Journal of Chemical Physics* 137.20 (2012), p. 204108. DOI: 10.1063/1.4767436.

[72] Dennis P Carroll, Harris J Silverstone, and Robert Melville Metzger. “Piecewise polynomial configuration interaction natural orbital study of 1 s 2 helium”. In: *The Journal of Chemical Physics* 71.10 (1979), pp. 4142–4163.

[73] Joseph Ivanic and Klaus Ruedenberg. “Identification of deadwood in configuration spaces through general direct configuration interaction”. In: *Theoretical Chemistry Accounts* 106.5 (2001), pp. 339–351. DOI: 10.1007/s002140100285.

[74] Per-Olov Löwdin. “Quantum theory of many-particle systems. I. Physical interpretations by means of density matrices, natural spin-orbitals, and convergence problems in the method of configurational interaction”. In: *Physical Review* 97.6 (1955), p. 1474. DOI: 10.1103/physrev.97.1474.

[75] Roger S Grev and Henry F Schaefer III. “Natural orbitals from single and double excitation configuration interaction wave functions: their use in second-order configuration interaction and wave functions incorporating limited triple and quadruple excitations”. In: *The Journal of chemical physics* 96.9 (1992), pp. 6850–6856. DOI: 10.1063/1.462574.

[76] Per-Olov Löwdin. “Quantum theory of cohesive properties of solids”. In: *Advances in Physics* 5.17 (1956), pp. 1–171. DOI: 10.1080/00018730110102196.

[77] Per-Olov Löwdin and Harrison Shull. "Natural orbitals in the quantum theory of two-electron systems". In: *Physical Review* 101.6 (1956), p. 1730. DOI: 10.1103/physrev.101.1730.

[78] Ernest R Davidson. "Properties and uses of natural orbitals". In: *Reviews of Modern Physics* 44.3 (1972), p. 451. DOI: 10.1103/revmodphys.44.451.

[79] Björn O Roos. "The complete active space self-consistent field method and its applications in electronic structure calculations". In: *Advances in Chemical Physics: Ab Initio Methods in Quantum Chemistry Part 2* 69 (1987), pp. 399–445. DOI: 10.1002/9780470142943.ch7.

[80] Katharina Boguslawski, Konrad H Marti, and Markus Reiher. "Construction of CASCI-type wave functions for very large active spaces". In: *The journal of chemical physics* 134.22 (2011), p. 224101. DOI: 10.1063/1.3596482.

[81] Yuki Kurashige, Garnet Kin-Lic Chan, and Takeshi Yanai. "Entangled quantum electronic wavefunctions of the Mn 4 CaO 5 cluster in photosystem II". In: *Nature chemistry* 5.8 (2013), pp. 660–666. DOI: 10.1038/nchem.1677.

[82] Sandeep Sharma et al. "Low-energy spectrum of iron–sulfur clusters directly from many-particle quantum mechanics". In: *Nature chemistry* 6.10 (2014), pp. 927–933. DOI: 10.1038/nchem.2041.

[83] Sebastian Wouters and Dimitri Van Neck. "The density matrix renormalization group for ab initio quantum chemistry". In: *The European Physical Journal D* 68.9 (2014), pp. 1–20. DOI: 10.1140/epjd/e2014-50500-1.

[84] Chr Møller and Milton S Plesset. "Note on an approximation treatment for many-electron systems". In: *Physical review* 46.7 (1934), p. 618. DOI: 10.1103/physrev.46.618.

[85] Haruyuki Nakano. "Quasidegenerate perturbation theory with multiconfigurational self-consistent-field reference functions". In: *The Journal of chemical physics* 99.10 (1993), pp. 7983–7992. DOI: 10.1063/1.465674.

[86] Friedemann Schautz, Francesco Buda, and Claudia Filippi. "Excitations in photoactive molecules from quantum Monte Carlo". In: *The Journal of chemical physics* 121.12 (2004), pp. 5836–5844. DOI: 10.1063/1.1777212.

[87] Thomas Bouabça et al. "A study of the fixed-node error in quantum Monte Carlo calculations of electronic transitions: The case of the singlet $n \rightarrow \pi^*$ (CO) transition of the acrolein". In: *The Journal of chemical physics* 130.11 (2009), p. 114107.

[88] Felix Plasser and Hans Lischka. “Multi-Reference Configuration Interaction”. In: *Quantum Chemistry and Dynamics of Excited States: Methods and Applications* (2020), pp. 277–297.

[89] Peter G Szalay et al. “Multiconfiguration self-consistent field and multireference configuration interaction methods and applications”. In: *Chemical reviews* 112.1 (2012), pp. 108–181.

[90] C David Sherrill and Henry F Schaefer III. “The configuration interaction method: Advances in highly correlated approaches”. In: *Advances in quantum chemistry*. Vol. 34. Elsevier, 1999, pp. 143–269.

[91] Trygve Helgaker, Poul Jorgensen, and Jeppe Olsen. *Molecular electronic-structure theory*. John Wiley & Sons, 2014.

[92] Björn O Roos. “Multiconfigurational quantum chemistry”. In: *Theory and Applications of Computational Chemistry*. Elsevier, 2005, pp. 725–764.

[93] Hans Lischka et al. “Multireference approaches for excited states of molecules”. In: *Chemical reviews* 118.15 (2018), pp. 7293–7361.

[94] KR Shamasundar, Gerald Knizia, and Hans-Joachim Werner. “A new internally contracted multi-reference configuration interaction method”. In: *The Journal of chemical physics* 135.5 (2011), p. 054101.

[95] Yubin Wang et al. “New schemes for internally contracted multi-reference configuration interaction”. In: *The Journal of Chemical Physics* 141.16 (2014), p. 164114.

[96] Robert J Gdanitz and Reinhart Ahlrichs. “The averaged coupled-pair functional (ACPF): A size-extensive modification of MR CI (SD)”. In: *Chemical physics letters* 143.5 (1988), pp. 413–420.

[97] Christel M Marian, Adrian Heil, and Martin Kleinschmidt. “The Dft/Mrci Method”. In: *Wiley Interdisciplinary Reviews: Computational Molecular Science* 9.2 (2019), e1394.

[98] Igor Lyskov, Martin Kleinschmidt, and Christel M Marian. “Redesign of the DFT/MRCI Hamiltonian”. In: *The Journal of chemical physics* 144.3 (2016), p. 034104.

[99] Felix Plasser et al. “The multiradical character of one-and two-dimensional graphene nanoribbons”. In: *Angewandte Chemie International Edition* 52.9 (2013), pp. 2581–2584.

[100] Werner Heisenberg. *Encounters with Einstein: And other essays on people, places, and particles*. Vol. 4. Princeton University Press, 1989.

[101] Susi Lehtola. “A review on non-relativistic, fully numerical electronic structure calculations on atoms and diatomic molecules”. In: *International Journal of Quantum Chemistry* 119.19 (2019), e25968. DOI: 10.1002/qua.25968.

[102] Thom H Dunning Jr. “Gaussian basis sets for use in correlated molecular calculations. I. The atoms boron through neon and hydrogen”. In: *The Journal of chemical physics* 90.2 (1989), pp. 1007–1023. DOI: 10.1063/1.456153.

[103] Susi Lehtola. “Fully numerical Hartree-Fock and density functional calculations. II. Diatomic molecules”. In: *International Journal of Quantum Chemistry* 119.19 (2019), e25944. DOI: 10.1002/qua.25944.

[104] Robert S Mulliken. “Electronic population analysis on LCAO–MO molecular wave functions. I”. In: *The Journal of Chemical Physics* 23.10 (1955), pp. 1833–1840. DOI: 10.1063/1.1740588.

[105] Daniel G Trabada et al. “Mulliken-Dipole Population Analysis”. In: (2020). DOI: 10.26434/chemrxiv.12722072.

[106] Per-Olov Löwdin. “On the non-orthogonality problem connected with the use of atomic wave functions in the theory of molecules and crystals”. In: *The Journal of Chemical Physics* 18.3 (1950), pp. 365–375. DOI: 10.1063/1.1747632.

[107] Alan E Reed, Robert B Weinstock, and Frank Weinhold. “Natural population analysis”. In: *The Journal of chemical physics* 83.2 (1985), pp. 735–746. DOI: 10.1063/1.449486.

[108] Fred L Hirshfeld. “Bonded-atom fragments for describing molecular charge densities”. In: *Theoretica chimica acta* 44.2 (1977), pp. 129–138. DOI: 10.1007/bf00549096.

[109] Richard FW Bader. “Atoms in molecules”. In: *Accounts of Chemical Research* 18.1 (1985), pp. 9–15. DOI: 10.1002/0470845015.caa012.

[110] Richard FW Bader. “A quantum theory of molecular structure and its applications”. In: *Chemical Reviews* 91.5 (1991), pp. 893–928. DOI: 10.1021/cr00005a013.

[111] Martin Klessinger and Josef Michl. *Excited states and photochemistry of organic molecules*. VCH publishers, 1995.

[112] Wolfgang Demtŕoder. *Atoms, Molecules and Photons: An Introduction to Atomic-, Molecular-and Quantum Physics*. Springer-Verlag Berlin Heidelberg, 2010. DOI: 10.1007/978-3-662-55523-1.

[113] Jun John Sakurai. *Advanced quantum mechanics*. Pearson Education India, 2006.

[114] Péter Szabó and Magnus Gustafsson. “A surface-hopping method for semiclassical calculations of cross sections for radiative association with electronic transitions”. In: *The Journal of Chemical Physics* 147.9 (2017), p. 094308. DOI: 10.1063/1.5000573.

[115] Tohru Azumi and Kazuo Matsuzaki. "What does the term "vibronic coupling" mean?" In: *Photochemistry and photobiology* 25.3 (1977), pp. 315–326. DOI: 10.1111/j.1751-1097.1977.tb06918.x.

[116] David R Yarkony. "Nonadiabatic Derivative Couplings". In: *Encyclopedia of Computational Chemistry* 3 (2002). DOI: 10.1002/0470845015.cna007.

[117] Michael Baer. *Beyond Born-Oppenheimer: electronic nonadiabatic coupling terms and conical intersections*. John Wiley & Sons, 2006.

[118] M Desouter-Lecomte and Jean-Claude Lorquet. "Nonadiabatic interactions in unimolecular decay. IV. Transition probability as a function of the Massey parameter". In: *The Journal of Chemical Physics* 71.11 (1979), pp. 4391–4403. DOI: 10.1063/1.438244.

[119] Richard Lee Ellis, G Kuehnlenz, and HH Jaffe. "The use of the CNDO method in spectroscopy". In: *Theoretica chimica acta* 26.2 (1972), pp. 131–140.

[120] Mary J Wirth, Aaron Koskelo, and Matthew J Sanders. "Molecular symmetry and two-photon spectroscopy". In: *Applied Spectroscopy* 35.1 (1981), pp. 14–21.

[121] Leszek Fiedor, Joanna Fiedor, and Mariusz Pilch. "Effects of molecular symmetry on the electronic transitions in carotenoids". In: *The Journal of Physical Chemistry Letters* 7.10 (2016), pp. 1821–1829.

[122] W Li et al. "A homonuclear molecule with a permanent electric dipole moment". In: *Science* 334.6059 (2011), pp. 1110–1114.

[123] Andrei V Nikitin, Michael Rey, and Vladimir G Tyuterev. "New dipole moment surfaces of methane". In: *Chemical Physics Letters* 565 (2013), pp. 5–11.

[124] Ivan F Antipov and Anatoly I Ivanov. "Effect of Symmetry Breaking in Excited Quadrupole Molecules on Transition Dipole Moment". In: *The Journal of Physical Chemistry B* 125.50 (2021), pp. 13778–13788.

[125] Robert L Carter. *Molecular symmetry and group theory*. Wiley New York, 1998.

[126] Jialun Ping, Fan Wang, and Jin-Quan Chen. *Group representation theory for physicists*. World Scientific Publishing Company, 2002.

[127] David Willock. *Molecular symmetry*. John Wiley & Sons, 2009.

[128] Christopher Bradley and Arthur Cracknell. *The mathematical theory of symmetry in solids: representation theory for point groups and space groups*. Oxford University Press, 2010.

[129] BD Sharma. "Crystallographic and spectroscopic symmetry notations". In: *Journal of Chemical Education* 59.7 (1982), p. 554.

[130] GL Breneman. "Crystallographic symmetry point group notation flow chart". In: *Journal of Chemical Education* 64.3 (1987), p. 216.

[131] H Burzlaff and H Zimmermann. "Point-group symbols". In: (2006).

[132] M. Karplus, R. N. Porter, and R. D. Sharma. "Exchange Reactions with Activation Energy. I. Simple Barrier Potential for (H, H_2)". In: *J. Chem. Phys* 43.3259 (Nov. 1965), p. 19651. DOI: 10.1063/1.1697301.

[133] Richard N. Porter and Lionel M. Raff. "Classical Trajectory Methods in Molecular Collisions". In: *Dynamics of molecular collisions*. Springer US, 1976, pp. 1–52. DOI: 10.1007/978-1-4757-0644-4_1.

[134] R. N. Porter, L. M. Raff, and W. H. Miller. "Quasiclassical selection of initial coordinates and momenta for a rotating Morse oscillator". In: *J. Chem. Phys.* 63.5 (1975), pp. 2214–2218. DOI: 10.1063/1.431603.

[135] Daniel S Lambrecht et al. "Simulated photoelectron spectra of the cyanide-water anion via quasiclassical molecular dynamics". In: *The Journal of Physical Chemistry A* 115.23 (2011), pp. 5928–5935.

[136] Eloy Ramos-Cordoba, Daniel S Lambrecht, and Martin Head-Gordon. "Charge-transfer and the hydrogen bond: Spectroscopic and structural implications from electronic structure calculations". In: *Faraday discussions* 150 (2011), pp. 345–362.

[137] Gabor Czako, Alexey L Kaledin, and Joel M Bowman. "A practical method to avoid zero-point leak in molecular dynamics calculations: Application to the water dimer". In: *The Journal of chemical physics* 132.16 (2010), p. 164103.

[138] N Gauthier. "Simple quantum calculation of the Rutherford cross section". In: *European Journal of Physics* 21.2 (2000), p. L17.

[139] E Huttel et al. "Screening corrections to the Rutherford cross section". In: *Nuclear Instruments and Methods in Physics Research Section B: Beam Interactions with Materials and Atoms* 12.2 (1985), pp. 193–199.

[140] M. Child. *Molecular Collision Theory*. Mineola, N.Y: Dover Publications, 1996. ISBN: 0486694372. DOI: 10.1063/1.3023376.

[141] A. Chicheportiche et al. "First principles transport coefficients and reaction rates of Ar_2^+ ions in argon for cold plasma jet modeling". In: *J. Chem. Phys.* 141.13 (Oct. 2014), p. 134302. DOI: 10.1063/1.4896613.

[142] A. Chicheportiche et al. "Ab initio transport coefficients of Ar^+ ions in Ar for cold plasma jet modeling." In: *Phys. Rev. E* 89.6 (June 2014), p. 063102. DOI: 10.1103/PhysRevE.89.063102.

[143] A. Chicheportiche. “Basic data of atomic and molecular helium and argon ions for the optimization of low temperature plasma jets used in the biomedical field.” in French. PhD thesis. Université Toulouse III Paul Sabatier, 2014.

[144] C. Van de Steen. “Modeling of transport properties of ions of krypton and xenon for optimization of cold rare-gas plasmas generators.” PhD thesis. Université Toulouse III Paul Sabatier and VSB – Technical University of Ostrava, 2018.

[145] Paolo Ugo, Pietro Marafini, and Marta Meneghello. “Bioanalytical Chemistry”. In: *Bioanalytical Chemistry*. De Gruyter, 2021.

[146] Adolf Fick. “Annalen der Physik und Chemie, 94, 59 (1855)”. In: *Uber Diffusion* (1855).

[147] Adrian Klinkenberg and F Sjenitzer. “Holding-time distributions of the Gaussian type”. In: *Chemical Engineering Science* 5.6 (1956), pp. 258–270.

[148] Thomas Baron. “Generalized graphical method for the design of fixed bed catalytic reactors”. In: *Chemical Engineering Progress* 48.3 (1952), pp. 118–124.

[149] Robert G Parr. “Density functional theory”. In: *Electron Distributions and the Chemical Bond*. Springer, 1982, pp. 95–100.

[150] Paul Geerlings, Frank De Proft, and Wilfried Langenaeker. “Conceptual density functional theory”. In: *Chemical reviews* 103.5 (2003), pp. 1793–1874.

[151] Maylis Orio, Dimitrios A Pantazis, and Frank Neese. “Density functional theory”. In: *Photosynthesis research* 102.2 (2009), pp. 443–453.

[152] Aron J Cohen, Paula Mori-Sánchez, and Weitao Yang. “Challenges for density functional theory”. In: *Chemical reviews* 112.1 (2012), pp. 289–320.

[153] Francisco M Fernández. *Introduction to perturbation theory in quantum mechanics*. CRC press, 2000.

[154] Daniel Roca-Sanjuán, Francesco Aquilante, and Roland Lindh. “Multiconfiguration second-order perturbation theory approach to strong electron correlation in chemistry and photochemistry”. In: *Wiley Interdisciplinary Reviews: Computational Molecular Science* 2.4 (2012), pp. 585–603.

[155] Jochen Autschbach and Tom Ziegler. “Double perturbation theory: a powerful tool in computational coordination chemistry”. In: *Coordination chemistry reviews* 238 (2003), pp. 83–126.

[156] Kestutis Aidas et al. “The D alton quantum chemistry program system”. In: *Wiley Interdisciplinary Reviews: Computational Molecular Science* 4.3 (2014), pp. 269–284.

[157] DIRAC, a relativistic ab initio electronic structure program, Release DIRAC22 (2022), written by H. J. Aa. Jensen, R. Bast, A. S. P. Gomes, T. Saue and L. Visscher, with contributions from I. A. Aucar, V. Bakken, C. Chibueze, J. Creutzberg, K. G. Dyall, S. Dubillard, U. Ekström, E. Eliav, T. Enevoldsen, E. Faßhauer, T. Fleig, O. Fossgaard, L. Halbert, E. D. Hedegård, T. Helgaker, B. Helmich–Paris, J. Henriksson, M. van Horn, M. Iliaš, Ch. R. Jacob, S. Knecht, S. Komorovský, O. Kullie, J. K. Lærdahl, C. V. Larsen, Y. S. Lee, N. H. List, H. S. Nataraj, M. K. Nayak, P. Norman, G. Olejniczak, J. Olsen, J. M. H. Olsen, A. Papadopoulos, Y. C. Park, J. K. Pedersen, M. Pernpointner, J. V. Pototschnig, R. di Remigio, M. Repisky, K. Ruud, P. Sałek, B. Schimmelpfennig, B. Senjean, A. Shee, J. Sikkema, A. Sunaga, A. J. Thorvaldsen, J. Thyssen, J. van Stralen, M. L. Vidal, S. Villaume, O. Visser, T. Winther, S. Yamamoto and X. Yuan (available at `http://dx.doi.org/10.5281/zenodo.6010450`, see also `http://www.diracprogram.org`).

[158] Edoardo Apra et al. "NWChem: Past, present, and future". In: *The Journal of chemical physics* 152.18 (2020), p. 184102.

[159] Daniel GA Smith et al. "PSI4 1.4: Open-source software for high-throughput quantum chemistry". In: *The Journal of chemical physics* 152.18 (2020), p. 184108.

[160] MJ ea Frisch et al. *Gaussian 16*. 2016.

[161] Evgeny Epifanovsky et al. "Software for the frontiers of quantum chemistry: An overview of developments in the Q-Chem 5 package". In: *The Journal of chemical physics* 155.8 (2021), p. 084801.

[162] Sree Ganesh Balasubramani et al. "TURBOMOLE: Modular program suite for ab initio quantum-chemical and condensed-matter simulations". In: *The Journal of chemical physics* 152.18 (2020), p. 184107.

[163] Hans-Joachim Werner et al. "Molpro: a general-purpose quantum chemistry program package". In: *Wiley Interdisciplinary Reviews: Computational Molecular Science* 2.2 (2012), pp. 242–253.

[164] Hans-Joachim Werner et al. "The Molpro quantum chemistry package". In: *The Journal of Chemical Physics* 152.14 (2020), p. 144107. DOI: `10.1063/5.0005081`.

[165] HJ Werner et al. "MOLPRO, version 2022.2, a package of ab initio programs, 2022". In: (2022).

[166] David W Walker and Jack J Dongarra. "Mpi: A Standard Message Passing Interface". In: *Supercomputer*. Citeseer. 1996.

[167] Leonardo Dagum and Ramesh Menon. "OpenMP: an industry standard API for shared-memory programming". In: *IEEE computational science and engineering* 5.1 (1998), pp. 46–55.

[168] Hans-Joachim Werner and Wilfried Meyer. "A quadratically convergent multiconfiguration–self-consistent field method with simultaneous optimization of orbitals and CI coefficients". In: *The Journal of Chemical Physics* 73.5 (1980), pp. 2342–2356.

[169] Hans-Joachim Werner and Wilfried Meyer. "A quadratically convergent MCSCF method for the simultaneous optimization of several states". In: *The Journal of Chemical Physics* 74.10 (1981), pp. 5794–5801. DOI: 10.1063/1.440892.

[170] David A Kreplin, Peter J Knowles, and Hans-Joachim Werner. "MCSCF optimization revisited. II. Combined first-and second-order orbital optimization for large molecules". In: *The Journal of Chemical Physics* 152.7 (2020), p. 074102.

[171] Peter J Knowles and Hans-Joachim Werner. "Internally contracted multiconfiguration-reference configuration interaction calculations for excited states". In: *Theoretica chimica acta* 84.1 (1992), pp. 95–103. DOI: 10.1007/BF01117405.

[172] Peter J Knowles and Hans-Joachim Werner. "An efficient method for the evaluation of coupling coefficients in configuration interaction calculations". In: *Chemical physics letters* 145.6 (1988), pp. 514–522. DOI: 10.1016/0009-2614(88)87412-8.

[173] Hans-Joachim Werner and Peter J Knowles. "An efficient internally contracted multiconfiguration–reference configuration interaction method". In: *The Journal of chemical physics* 89.9 (1988), pp. 5803–5814. DOI: 10.1063/1.455556.

[174] Kirk A. Peterson and Thom H. Dunning Jr. "Accurate correlation consistent basis sets for molecular core–valence correlation effects: The second row atoms Al–Ar, and the first row atoms B–Ne revisited". In: *J. Chem. Phys.* 117.23 (2002), pp. 10548–10560. DOI: 10.1063/1.1520138.

[175] Deheng Shi et al. "Spectroscopic Constants and Molecular Properties of $X^2\Sigma_g^+$, $A^2\Pi_u$, $B^2\Sigma_u^+$ and $D^2\Pi_g$ Electronic States of the N_2^+ Ion". In: *Comp. Theor. Chem.* 966 (2011), p. 44. DOI: 10.1016/j.comptc.2011.02.011.

[176] Charlotte E Moore. *Selected Tables of Atomic Spectra, Atomic Energy Levels. Multiplet Tables N I, N II, N III.* Tech. rep. NATIONAL STANDARD REFERENCE DATA SYSTEM, 1975.

[177] Robert J. Le Roy. "LEVEL: A computer program for solving the radial Schrödinger equation for bound and quasibound levels". In: *J Quant Spectrosc Radiat Transf* 186 (Jan. 2017). Satellite Remote Sensing and Spectroscopy: Joint ACE-Odin Meeting, October 2015, pp. 167–178. ISSN: 0022-4073. DOI: 10.1016/j.jqsrt.2016.05.028.

[178] "MATLAB 9.9.0.1857802 (R2020b) Update 7". In: (2020).

[179] Michael P Allen and Dominic J Tildesley. "Computer simulation of liquids. 1987". In: *New York: Oxford* 385 (1989).

[180] David P Landau and Kurt Binder. *A Guide to Monte Carlo Simulations in Statistical Physics*. Cambridge: Cambridge University Press, 2000. DOI: 10.1017/9781108780346.

[181] Jens Peder Dahl and Michael Springborg. "The Morse oscillator in position space, momentum space, and phase space". In: *The Journal of chemical physics* 88.7 (1988), pp. 4535–4547. DOI: 10.1063/1.453761.

[182] Alexander D MacKerell Jr et al. "CHARMM: the energy function and its parameterization". In: *Encyclopedia of computational chemistry* 1 (2002). DOI: 10.1002/0470845015.cfa007.

[183] John E Lennard-Jones. "On the determination of molecular fields". In: *Proc. R. Soc. London* 106 (1924), pp. 441–477.

[184] Adri CT Van Duin et al. "ReaxFF: a reactive force field for hydrocarbons". In: *The Journal of Physical Chemistry A* 105.41 (2001), pp. 9396–9409. DOI: 10.1021/jp004368u.

[185] N Sathyamurthy and LM Raff. "Quasiclassical trajectory studies using 3D spline interpolation of abinitio surfaces". In: *The Journal of Chemical Physics* 63.1 (1975), pp. 464–473.

[186] AJC Varandas. "Intermolecular and intramolecular potentials". In: *Adv. Chem. Phys* 74 (1988), pp. 255–338.

[187] Michael A Collins. "Molecular potential-energy surfaces for chemical reaction dynamics". In: *Theoretical Chemistry Accounts* 108.6 (2002), pp. 313–324. DOI: 10.1002/chin.200319289.

[188] Timothy Hollebeek, Tak-San Ho, and Herschel Rabitz. "Constructing multidimensional molecular potential energy surfaces from ab initio data". In: *Annual review of physical chemistry* 50.1 (1999), pp. 537–570.

[189] Richard Dawes, Albert F Wagner, and Donald L Thompson. "Ab initio wavenumber accurate spectroscopy: 1CH2 and HCN vibrational levels on automatically generated IMLS potential energy surfaces". In: *The Journal of Physical Chemistry A* 113.16 (2009), pp. 4709–4721.

[190] Marvin Poul et al. "Systematic Structure Datasets for Machine Learning Potentials: Application to Moment Tensor Potentials of Magnesium and its Defects". In: *arXiv preprint arXiv:2207.04009* (2022).

[191] Alexander V Shapeev. "Moment tensor potentials: A class of systematically improvable interatomic potentials". In: *Multiscale Modeling & Simulation* 14.3 (2016), pp. 1153–1173.

[192] II Novoselov et al. “Moment tensor potentials as a promising tool to study diffusion processes”. In: *Computational Materials Science* 164 (2019), pp. 46–56.

[193] Aidan P Thompson et al. “Spectral neighbor analysis method for automated generation of quantum-accurate interatomic potentials”. In: *Journal of Computational Physics* 285 (2015), pp. 316–330.

[194] Zhi Deng et al. “An Electrostatic Spectral Neighbor Analysis Potential (eSNAP) for Lithium Nitride”. In: *arXiv preprint arXiv:1901.08749* (2019).

[195] Ralf Drautz. “Atomic cluster expansion for accurate and transferable interatomic potentials”. In: *Physical Review B* 99.1 (2019), p. 014104.

[196] Ralf Drautz. “Atomic cluster expansion of scalar, vectorial, and tensorial properties including magnetism and charge transfer”. In: *Physical Review B* 102.2 (2020), p. 024104.

[197] Genevieve Dusson et al. “Atomic cluster expansion: Completeness, efficiency and stability”. In: *arXiv preprint arXiv:1911.03550* (2019).

[198] Ovidiu Ivanciuc et al. “Applications of support vector machines in chemistry”. In: *Reviews in computational chemistry* 23 (2007), p. 291.

[199] Hongdong Li, Yizeng Liang, and Qingsong Xu. “Support vector machines and its applications in chemistry”. In: *Chemometrics and Intelligent Laboratory Systems* 95.2 (2009), pp. 188–198.

[200] Roman M Balabin and Ekaterina I Lomakina. “Support vector machine regression (LS-SVM)—an alternative to artificial neural networks (ANNs) for the analysis of quantum chemistry data?” In: *Physical Chemistry Chemical Physics* 13.24 (2011), pp. 11710–11718.

[201] Aditya Kamath et al. “Neural networks vs Gaussian process regression for representing potential energy surfaces: A comparative study of fit quality and vibrational spectrum accuracy”. In: *The Journal of chemical physics* 148.24 (2018), p. 241702.

[202] Volker L Deringer et al. “Gaussian process regression for materials and molecules”. In: *Chemical Reviews* 121.16 (2021), pp. 10073–10141.

[203] Jonathan P Alborzpour, David P Tew, and Scott Habershon. “Efficient and accurate evaluation of potential energy matrix elements for quantum dynamics using Gaussian process regression”. In: *The Journal of Chemical Physics* 145.17 (2016), p. 174112.

[204] Kristof Schütt et al. “Schnet: A continuous-filter convolutional neural network for modeling quantum interactions”. In: *Advances in neural information processing systems* 30 (2017).

[205] Connor W Coley et al. “A graph-convolutional neural network model for the prediction of chemical reactivity”. In: *Chemical science* 10.2 (2019), pp. 370–377.

[206] Jure Zupan, Marjana Novič, and Itziar Ruisánchez. "Kohonen and counterpropagation artificial neural networks in analytical chemistry". In: *Chemometrics and Intelligent Laboratory Systems* 38.1 (1997), pp. 1–23.

[207] WJ Melssen et al. "Using artificial neural networks for solving chemical problems: Part II. Kohonen self-organising feature maps and Hopfield networks". In: *Chemometrics and Intelligent Laboratory Systems* 23.2 (1994), pp. 267–291.

[208] DB Kirew et al. "Application of Kohonen Neural Networks in classification of biologically active compounds". In: *SAR and QSAR in Environmental Research* 8.1-2 (1998), pp. 93–107.

[209] Boris Hanin. "Which neural net architectures give rise to exploding and vanishing gradients?" In: *Advances in neural information processing systems* 31 (2018).

[210] Hong Hui Tan and King Hann Lim. "Vanishing gradient mitigation with deep learning neural network optimization". In: *2019 7th international conference on smart computing & communications (ICSCC)*. IEEE. 2019, pp. 1–4.

[211] Abien Fred Agarap. "Deep learning using rectified linear units (relu)". In: *arXiv preprint arXiv:1803.08375* (2018).

[212] Digvijay Boob, Santanu S Dey, and Guanghui Lan. "Complexity of training relu neural network". In: *Discrete Optimization* (2020), p. 100620.

[213] Philipp Petersen and Felix Voigtlaender. "Optimal approximation of piecewise smooth functions using deep ReLU neural networks". In: *Neural Networks* 108 (2018), pp. 296–330.

[214] Meiqi Wang et al. "A high-speed and low-complexity architecture for softmax function in deep learning". In: *2018 IEEE asia pacific conference on circuits and systems (APCCAS)*. IEEE. 2018, pp. 223–226.

[215] Weiwei Kong et al. "Rankmax: An adaptive projection alternative to the softmax function". In: *Advances in Neural Information Processing Systems* 33 (2020), pp. 633–643.

[216] Eric J Hartman, James D Keeler, and Jacek M Kowalski. "Layered neural networks with Gaussian hidden units as universal approximations". In: *Neural computation* 2.2 (1990), pp. 210–215.

[217] Chien-Cheng Lee et al. "Robust radial basis function neural networks". In: *IEEE Transactions on Systems, Man, and Cybernetics, Part B (Cybernetics)* 29.6 (1999), pp. 674–685.

[218] Arnaud De Myttenaere et al. "Mean absolute percentage error for regression models". In: *Neurocomputing* 192 (2016), pp. 38–48.

[219] Chris Tofallis. “A better measure of relative prediction accuracy for model selection and model estimation”. In: *Journal of the Operational Research Society* 66.8 (2015), pp. 1352–1362.

[220] J Scott Armstrong and Long-Range Forecasting. “From crystal ball to computer”. In: *New York ua* 348 (1985).

[221] Benito E Flores. “A pragmatic view of accuracy measurement in forecasting”. In: *Omega* 14.2 (1986), pp. 93–98.

[222] Norman R Draper and Harry Smith. *Applied regression analysis*. Vol. 326. John Wiley & Sons, 1998.

[223] Cort J Willmott and Kenji Matsuura. “On the use of dimensioned measures of error to evaluate the performance of spatial interpolators”. In: *International Journal of Geographical Information Science* 20.1 (2006), pp. 89–102.

[224] Marco Gori and Alberto Tesi. “On the problem of local minima in backpropagation”. In: *IEEE Transactions on Pattern Analysis and Machine Intelligence* 14.1 (1992), pp. 76–86.

[225] YQ Chen, T Yin, and HA Babri. “A stochastic backpropagation algorithm for training neural networks”. In: *Proceedings of ICICS, 1997 International Conference on Information, Communications and Signal Processing. Theme: Trends in Information Systems Engineering and Wireless Multimedia Communications (Cat.* Vol. 2. IEEE. 1997, pp. 703–707.

[226] Bedri C Cetin, Joel W Burdick, and Jacob Barhen. “Global descent replaces gradient descent to avoid local minima problem in learning with artificial neural networks”. In: *IEEE International Conference on Neural Networks*. IEEE. 1993, pp. 836–842.

[227] Monica Bianchini, Paolo Frasconi, and Marco Gori. “Learning without local minima in radial basis function networks”. In: *IEEE transactions on neural networks* 6.3 (1995), pp. 749–756.

[228] Seyedali Mirjalili. “Evolutionary algorithms and neural networks”. In: *Studies in computational intelligence*. Vol. 780. Springer, 2019.

[229] NG Pavlidis et al. “Spiking neural network training using evolutionary algorithms”. In: *Proceedings. 2005 IEEE International Joint Conference on Neural Networks, 2005.* Vol. 4. IEEE. 2005, pp. 2190–2194.

[230] Adam Slowik and Michal Bialko. “Training of artificial neural networks using differential evolution algorithm”. In: *2008 conference on human system interactions*. IEEE. 2008, pp. 60–65.

[231] Venu G Gudise and Ganesh K Venayagamoorthy. “Comparison of particle swarm optimization and backpropagation as training algorithms for neural networks”. In: *Proceedings of the 2003 IEEE Swarm Intelligence Symposium. SIS'03 (Cat. No. 03EX706)*. IEEE. 2003, pp. 110–117.

[232] Michael Meissner, Michael Schmuker, and Gisbert Schneider. “Optimized Particle Swarm Optimization (OPSO) and its application to artificial neural network training”. In: *BMC bioinformatics* 7.1 (2006), pp. 1–11.

[233] Argha Roy, Diptam Dutta, and Kaustav Choudhury. “Training artificial neural network using particle swarm optimization algorithm”. In: *International Journal of Advanced Research in Computer Science and Software Engineering* 3.3 (2013).

[234] Buthainah Al-kazemi and Chilukuri K Mohan. “Training feedforward neural networks using multi-phase particle swarm optimization”. In: *Proceedings of the 9th International Conference on Neural Information Processing, 2002. ICONIP'02.* Vol. 5. IEEE. 2002, pp. 2615–2619.

[235] Rui Mendes et al. “Particle swarms for feedforward neural network training”. In: *Proceedings of the 2002 International Joint Conference on Neural Networks. IJCNN'02 (Cat. No. 02CH37290)*. Vol. 2. IEEE. 2002, pp. 1895–1899.

[236] Anthony Triche, Anthony S Maida, and Ashok Kumar. “Exploration in neo-Hebbian reinforcement learning: Computational approaches to the exploration-exploitation balance with bio-inspired neural networks”. In: *Neural Networks* (2022).

[237] Linnan Wang et al. “Alphax: exploring neural architectures with deep neural networks and monte carlo tree search”. In: *arXiv preprint arXiv:1903.11059* (2019).

[238] Hedy Attouch, Xavier Goudou, and Patrick Redont. “The heavy ball with friction method, I. The continuous dynamical system: global exploration of the local minima of a real-valued function by asymptotic analysis of a dissipative dynamical system”. In: *Communications in Contemporary Mathematics* 2.01 (2000), pp. 1–34.

[239] Mohammad Javad Mahmoodabadi, Z Salahshoor Mottaghi, and Ahmad Bagheri. “HEPSO: high exploration particle swarm optimization”. In: *Information Sciences* 273 (2014), pp. 101–111.

[240] RK Agrawal, Baljeet Kaur, and Parul Agarwal. “Quantum inspired Particle Swarm Optimization with guided exploration for function optimization”. In: *Applied Soft Computing* 102 (2021), p. 107122.

[241] Islam A ElShaarawy et al. “An exploration-enhanced elephant herding optimization”. In: *Engineering Computations* (2019).

[242] Naman Agarwal et al. “Finding approximate local minima faster than gradient descent”. In: *Proceedings of the 49th Annual ACM SIGACT Symposium on Theory of Computing*. 2017, pp. 1195–1199.

[243] Grzegorz Swirszcz, Wojciech Marian Czarnecki, and Razvan Pascanu. “Local minima in training of neural networks”. In: *arXiv preprint arXiv:1611.06310* (2016).

[244] Monica Bianchini, Marco Gori, and Marco Maggini. “On the problem of local minima in recurrent neural networks”. In: *IEEE Transactions on Neural Networks* 5.2 (1994), pp. 167–177.

[245] Mathew M Noel. “A new gradient based particle swarm optimization algorithm for accurate computation of global minimum”. In: *Applied Soft Computing* 12.1 (2012), pp. 353–359.

[246] Shahrouz Ryan Alimo, Pooriya Beyhaghi, and Thomas R Bewley. “Optimization combining derivative-free global exploration with derivative-based local refinement”. In: *2017 IEEE 56th Annual Conference on Decision and Control (CDC)*. IEEE. 2017, pp. 2531–2538.

[247] Matthias Feurer and Frank Hutter. “Hyperparameter optimization”. In: *Automated machine learning*. Springer, Cham, 2019, pp. 3–33.

[248] James Bergstra et al. “Algorithms for hyper-parameter optimization”. In: *Advances in neural information processing systems* 24 (2011).

[249] Tong Yu and Hong Zhu. “Hyper-parameter optimization: A review of algorithms and applications”. In: *arXiv preprint arXiv:2003.05689* (2020).

[250] Gonzalo I Diaz et al. “An effective algorithm for hyperparameter optimization of neural networks”. In: *IBM Journal of Research and Development* 61.4/5 (2017), pp. 9–1.

[251] Dougal Maclaurin, David Duvenaud, and Ryan Adams. “Gradient-based hyperparameter optimization through reversible learning”. In: *International conference on machine learning*. PMLR. 2015, pp. 2113–2122.

[252] Mohammad Reza Keshtkaran and Chethan Pandarinath. “Enabling hyperparameter optimization in sequential autoencoders for spiking neural data”. In: *Advances in Neural Information Processing Systems* 32 (2019).

[253] Saeid Parvandeh et al. “Consensus features nested cross-validation”. In: *Bioinformatics* 36.10 (2020), pp. 3093–3098.

[254] Ali S Hadi, AHM Rahmatullah Imon, and Mark Werner. “Detection of outliers”. In: *Wiley Interdisciplinary Reviews: Computational Statistics* 1.1 (2009), pp. 57–70.

[255] Fabrizio Angiulli, Stefano Basta, and Clara Pizzuti. "Distance-based detection and prediction of outliers". In: *IEEE transactions on knowledge and data engineering* 18.2 (2005), pp. 145–160.

[256] Mark Last and Abraham Kandel. "Automated detection of outliers in real-world data". In: *Proceedings of the second international conference on intelligent technologies*. In-Tech. 2001, pp. 292–301.

[257] Andrzej S Kosinski. "A procedure for the detection of multivariate outliers". In: *Computational statistics & data analysis* 29.2 (1998), pp. 145–161.

[258] Denis Cousineau and Sylvain Chartier. "Outliers detection and treatment: a review." In: *International Journal of Psychological Research* 3.1 (2010), pp. 58–67.

[259] Jörg Behler. "Neural network potential-energy surfaces in chemistry: a tool for large-scale simulations". en. In: *Phys. Chem. Chem. Phys.* 13.40 (2011), p. 17930. ISSN: 1463-9076, 1463-9084. DOI: 10.1039/c1cp21668f. URL: http://xlink.rsc.org/?DOI=c1cp21668f (visited on 09/15/2019).

[260] Jörg Behler. "Constructing high-dimensional neural network potentials: A tutorial review". en. In: *Int. J. Quantum Chem.* 115.16 (Aug. 15, 2015), pp. 1032–1050. ISSN: 0020-7608. DOI: 10.1002/qua.24890. (Visited on 09/15/2019).

[261] Emir Kocer, Jeremy K Mason, and Hakan Erturk. "A novel approach to describe chemical environments in high-dimensional neural network potentials". In: *The Journal of chemical physics* 150.15 (2019), p. 154102.

[262] Mingjie Liu and John R Kitchin. "SingleNN: modified behler–Parrinello neural network with shared weights for atomistic simulations with transferability". In: *The Journal of Physical Chemistry C* 124.32 (2020), pp. 17811–17818.

[263] Bin Jiang and Hua Guo. "Permutation invariant polynomial neural network approach to fitting potential energy surfaces". In: *The Journal of chemical physics* 139.5 (2013), p. 054112. DOI: 10.1063/1.4817187.

[264] Jun Li, Bin Jiang, and Hua Guo. "Permutation invariant polynomial neural network approach to fitting potential energy surfaces. II. Four-atom systems". In: *The Journal of chemical physics* 139.20 (2013), p. 204103. DOI: 10.1063/1.4832697.

[265] Bin Jiang, Jun Li, and Hua Guo. "Potential energy surfaces from high fidelity fitting of ab initio points: the permutation invariant polynomial-neural network approach". In: *International Reviews in Physical Chemistry* 35.3 (2016), pp. 479–506.

[266] Bastiaan J Braams and Joel M Bowman. "Permutationally invariant potential energy surfaces in high dimensionality". In: *International Reviews in Physical Chemistry* 28.4 (2009), pp. 577–606.

[267] Zhen Xie and Joel M Bowman. "Permutationally invariant polynomial basis for molecular energy surface fitting via monomial symmetrization". In: *Journal of Chemical Theory and Computation* 6.1 (2010), pp. 26–34.

[268] Joel M Bowman, Gabor Czako, and Bina Fu. "High-dimensional ab initio potential energy surfaces for reaction dynamics calculations". In: *Physical Chemistry Chemical Physics* 13.18 (2011), pp. 8094–8111.

[269] Thomas B. Blank and Steven D. Brown. "Adaptive, global, extended Kalman filters for training feedforward neural networks". In: *J. Chemom.* 8.6 (1994), pp. 391–407. DOI: 10.1002/cem.1180080605.

[270] M. Beseda et al. "Modeling of the N_2^+ ion in cold helium plasma I. *Ab initio* approaches for N_2^+ and N_2^+/He ions." The immediately preceding paper.

[271] A. G. Császár and W. D. Allen. "The effect of 1s correlation on D_e, r_e , and ω_e of first-row diatomics". In: *J. Chem. Phys.* 104 (1996), pp. 2746–2748. DOI: 10.1063/1.471008.

[272] Hiu Liu et al. "Theoretical spectroscopic calculations on the 25 Λ–S and 66 Ω states of N_2^+ cation in the gas phase including the spin–orbit coupling effect". In: *J Quant Spectrosc Radiat Transf* 147 (2014), p. 207. DOI: 10.1016/j.jqsrt.2014.05.031.

[273] Xiaonan Tang et al. "Pulsed field-ionization photoelectron-photoion coincidence study of the process $N_2 + h\nu \rightarrow N^+ + N + e^-$: Bond dissociation energies of N_2 and N_2^+". en. In: *J. Chem. Phys* 123.7 (Aug. 2005), p. 074330. ISSN: 0021-9606, 1089-7690. DOI: 10.1063/1.1995699. (Visited on 10/14/2021).

[274] K. P. Huber and G. Herzberg. *Molecular Spectra and Molecular Structure IV. Constants of Diatomic Molecules*. New York: Litton Educational Publishing Inc., 1979. DOI: 10.1007/978-1-4757-0961-2.

[275] M. Yousfi et al. "Basic data of ions in He-air mixtures for fluid modeling of low temperature plasma jets". In: *J. Appl. Phys.* 112.4 (Aug. 2012), p. 043301. DOI: 10.1063/1.4747936.

[276] S. Paláček et al. "Modeling of the N_2^+ ion in cold helium plasma: dynamics of N_2^+/He collisions and cross-sections." Submitted to Plasma Source Sci. Tech.

[277] S. Paláček et al. "Modeling of the N_2^+ ion in cold helium plasma II: transport properties of N_2^+ in helium." under preparation.

[278] M. McFarland et al. "Flow-drift technique for ion mobility and ion-molecule reaction rate constant measurements. II. Positive ion reactions of N^+, O^+, and H_2^+ with O_2 and O^+ with N_2 from thermal to $\approx 2\,\mathrm{eV}$". In: *J. Chem. Phys.* 59.12 (Dec. 1973), pp. 6620–6628. DOI: 10.1063/1.1680042.

[279] Y. Kaneko, T. Koizumi, and N. Kobayashi. "Mobilities of Various Ions in Non-Parent Gases; Compilation of the Mobility Data Measured with the Injected-Ion Drift Tube Mass Spectrometer in Tokyo Metropolitan University." In: *J. Mass. Spec. Soc. Japan* 26.1 (1978), pp. 35–52. DOI: 10.5702/massspec1953.26.35.

[280] E. B. Anthony et al. "Laser probing of rotational-state-dependent velocity distributions of $N_2^+(v'' = 0, J)$ drifted in He". In: *The Journal of Chemical Physics* 112.23 (June 15, 2000), p. 10269. ISSN: 0021-9606, 1089-7690. DOI: 10.1063/1.481667. (Visited on 04/11/2020).

[281] H. W. Ellis et al. "Transport properties of gaseous ions over a wide energy range". In: *At. Data Nucl. Data Tables* 17.3 (Mar. 1976), p. 177. DOI: 10.1016/0092-640X(76)90001-2.

[282] R. Johnsen, H. L. Brown, and M. A. Biondi. "Ion–Molecule Reactions Involving N_2^+, N^+, O_2^+, and O^+ Ions from 300° K to $\approx 1\,\mathrm{eV}$". In: *J. Chem. Phys.* 52.10 (May 1970), p. 5080. DOI: 10.1063/1.1672745.

[283] K. Ohtsuki, M. Hananoe, and M. Matsuzawa. "Anomalous Decline of Molecular Ion Mobility in Cooled Helium Gas". In: *Phys. Rev. Letters* 95 (2005), p. 213201. DOI: 10.1103/PhysRevLett.95.213201.

[284] R. Baranowski, B. Wagner, and M. Thachuk. "Molecular dynamics study of the collision-induced rotational alignment of N_2^+ drifting in helium". In: *The Journal of Chemical Physics* 114.15 (Apr. 15, 2001), p. 6662. ISSN: 0021-9606, 1089-7690. DOI: 10.1063/1.1354177. (Visited on 04/11/2020).

[285] Paolo Celani and Hans-Joachim Werner. "Multireference perturbation theory for large restricted and selected active space reference wave functions". In: *The Journal of Chemical Physics* 112.13 (2000), pp. 5546–5557.

[286] Abril Carolina Castro et al. "Scalar and Spin- Orbit Relativistic Corrections to the NICS and the Induced Magnetic Field: The case of the E122- Spherenes (E= Ge, Sn, Pb)". In: *Journal of Chemical Theory and Computation* 6.9 (2010), pp. 2701–2705.

[287] Victor Galitski and Ian B Spielman. "Spin–orbit coupling in quantum gases". In: *Nature* 494.7435 (2013), pp. 49–54.

Appendix A

Excited states of N_2^+

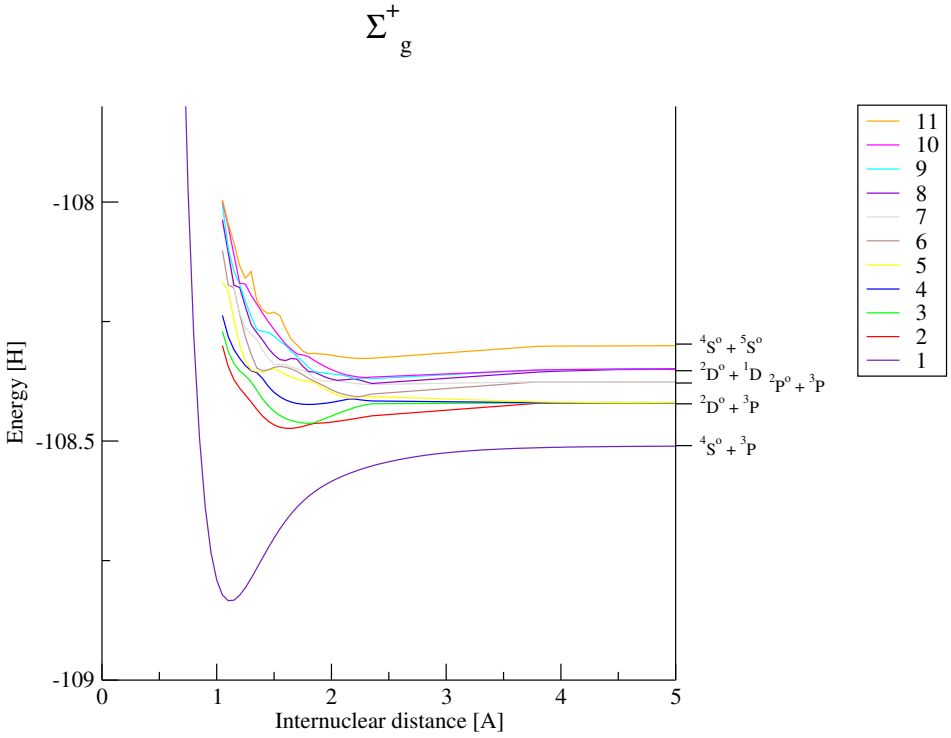

Figure A.1: PECs of eleven lowest N_2^+ Σ_g^+ states

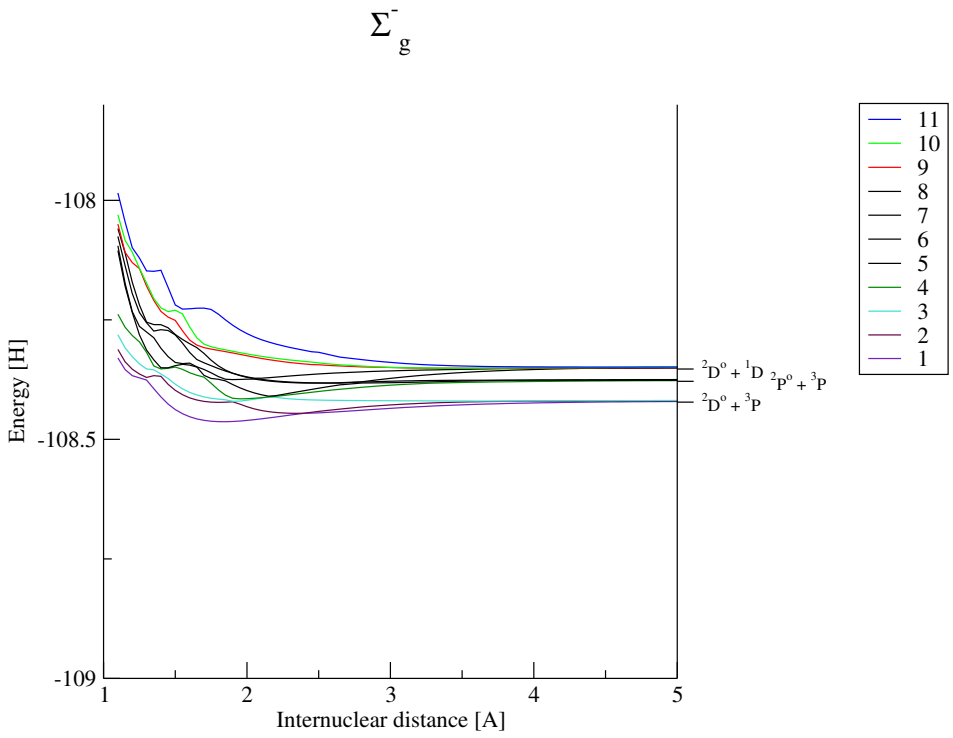

Figure A.2: PECs of eleven lowest N_2^+ Σ_g^- states

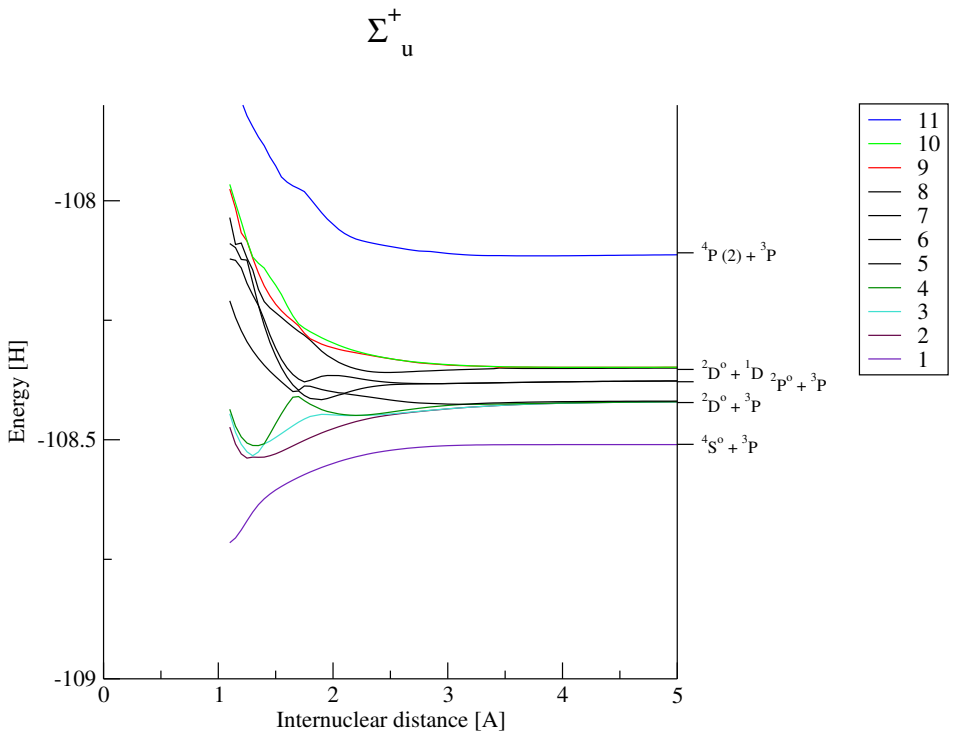

Figure A.3: PECs of eleven lowest N_2^+ Σ_u^+ states

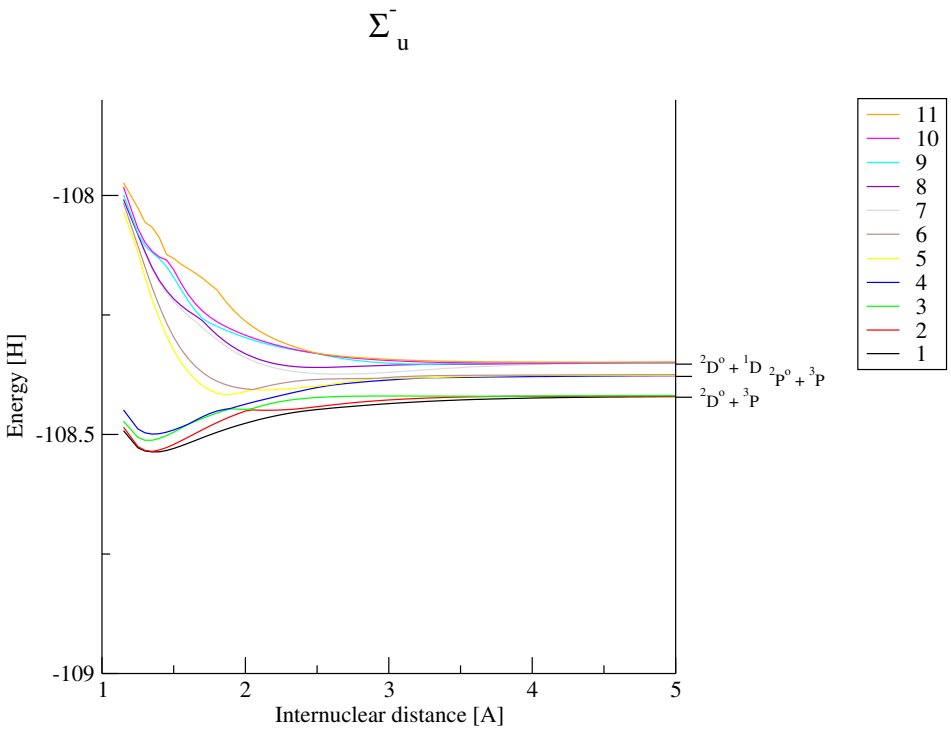

Figure A.4: PECs of eleven lowest N_2^+ Σ_u^- states

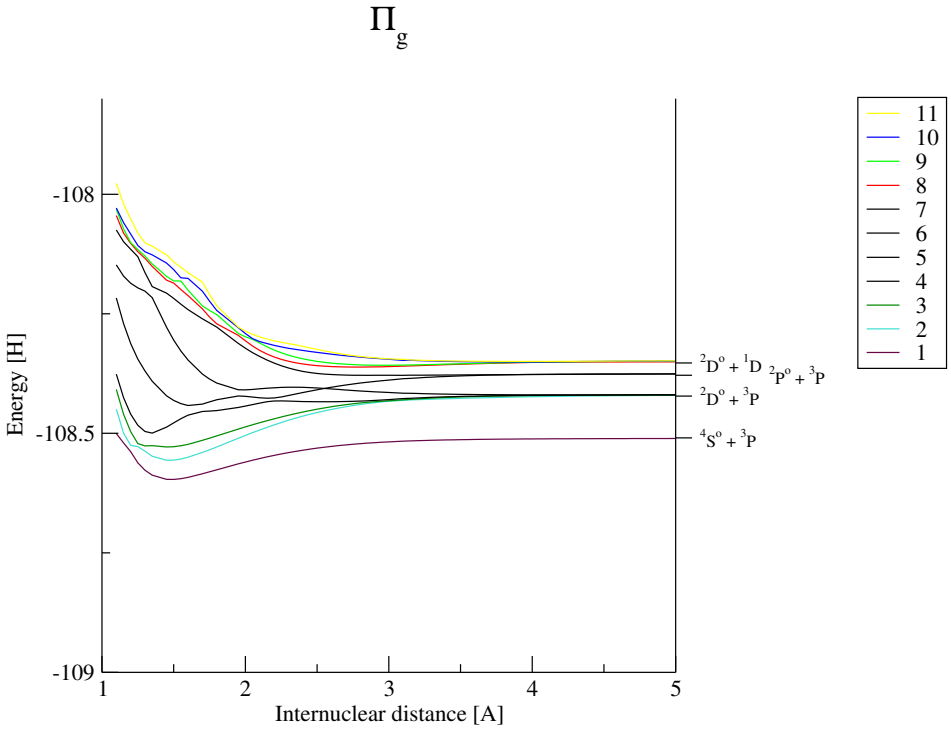

Figure A.5: PECs of eleven lowest N_2^+ Π_g states

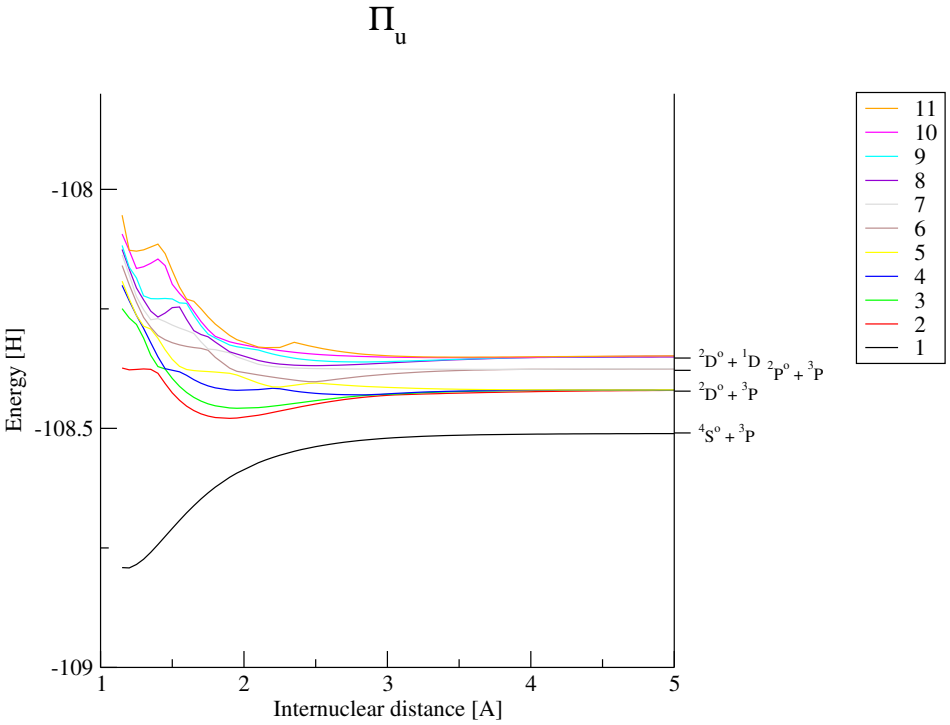

Figure A.6: PECs of eleven lowest N_2^+ Π_u states

Appendix B

Excited States of N_2^+/He

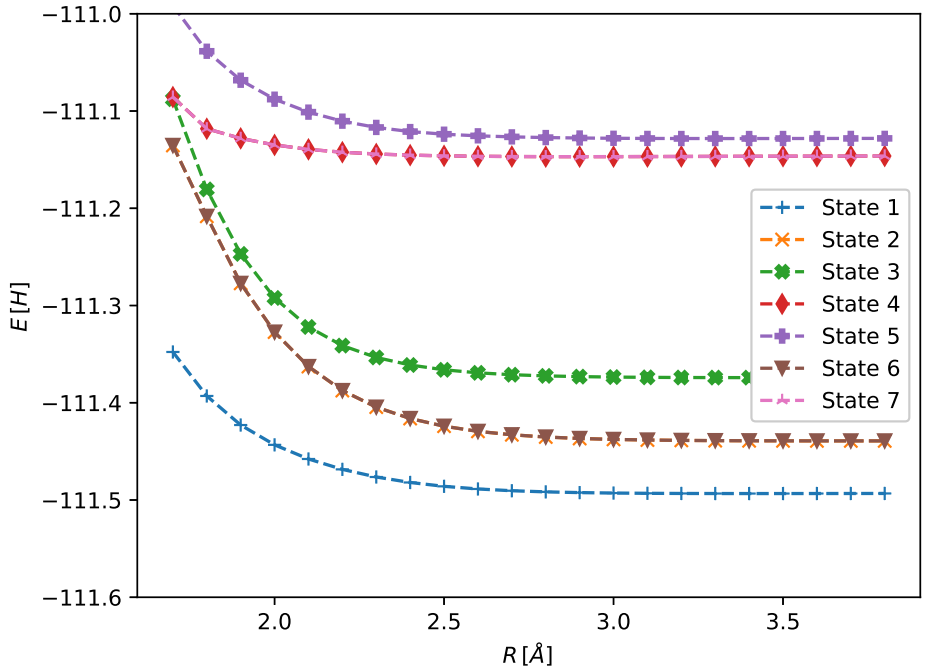

Figure B.1: PEC of the seven lowest MCSCF states computed for $\theta = 0°$, with $11A'$, $2A''$ orbital space and aug-cc-pVTZ basis set with $r = 1.12\,Å$.

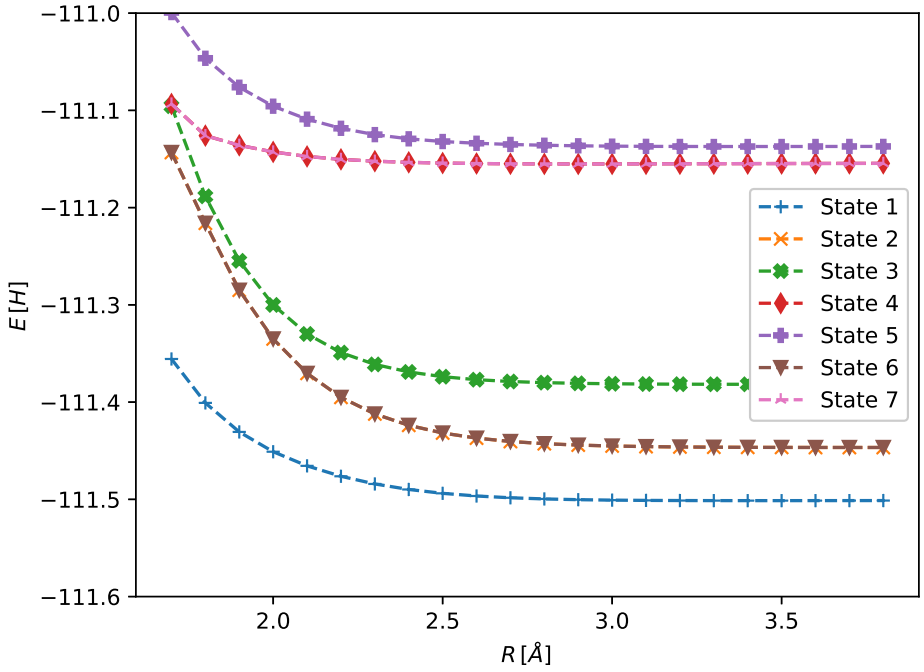

Figure B.2: PEC of the seven lowest MCSCF states computed for $\theta = 0°$, with 11A′, 2A″ orbital space and aug-cc-pVQZ basis set with $r = 1.12$ Å.

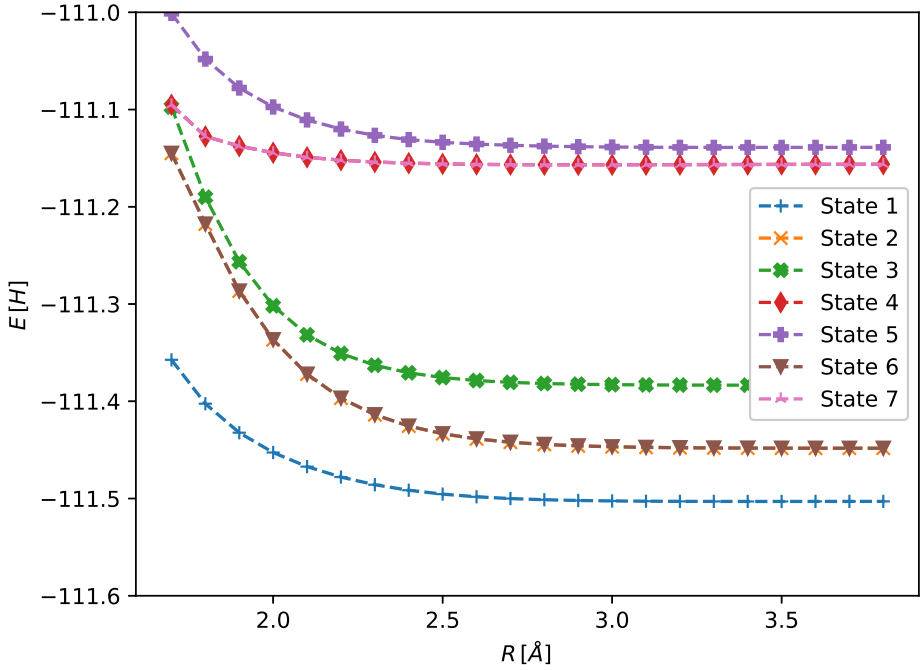

Figure B.3: PEC of the seven lowest MCSCF states computed for $\theta = 0°$, with 11A′, 2A″ orbital space and aug-cc-pV5Z basis set with $r = 1.12$ Å.

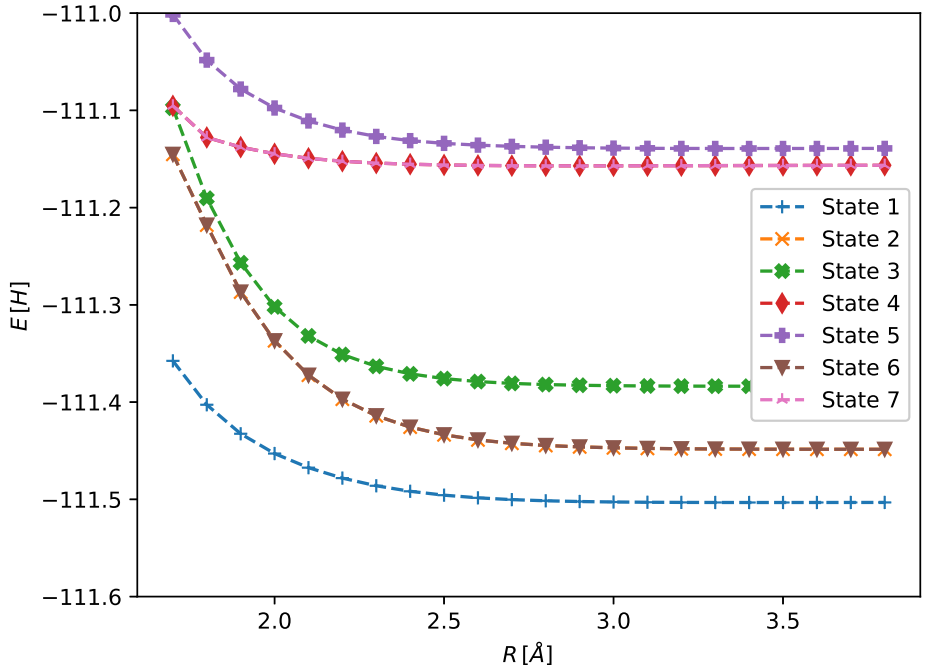

Figure B.4: PEC of the seven lowest MCSCF states computed for $\theta = 0°$, with 11A′, 2A″ orbital space and aug-cc-pV6Z basis set with $r = 1.12$ Å.

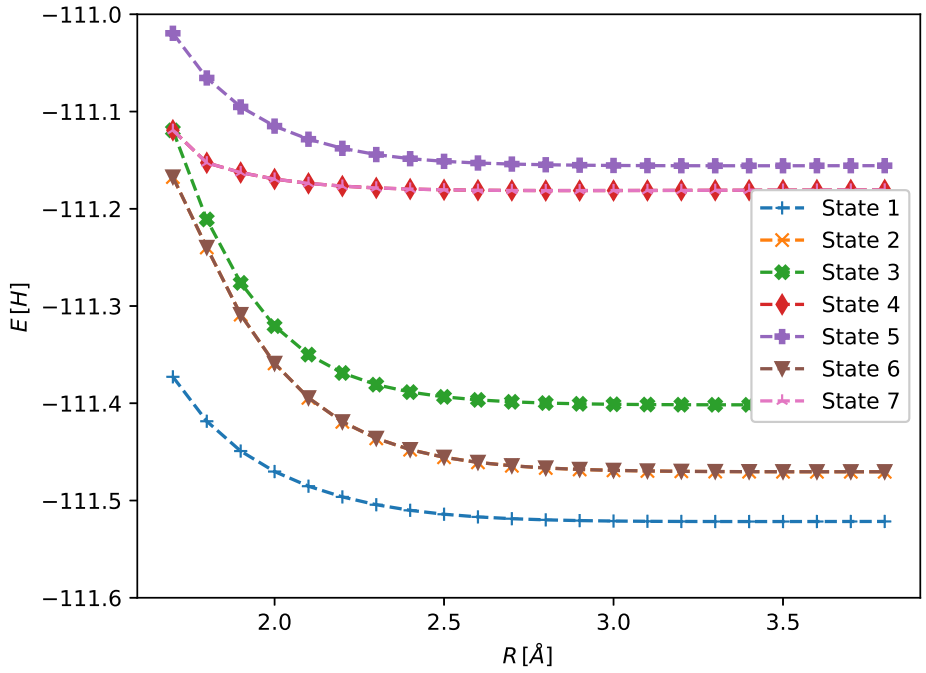

Figure B.5: PEC of the seven lowest MCSCF states computed for $\theta = 0°$, with 12A′, 3A″ orbital space and aug-cc-pVTZ basis set with $r = 1.12$ Å.

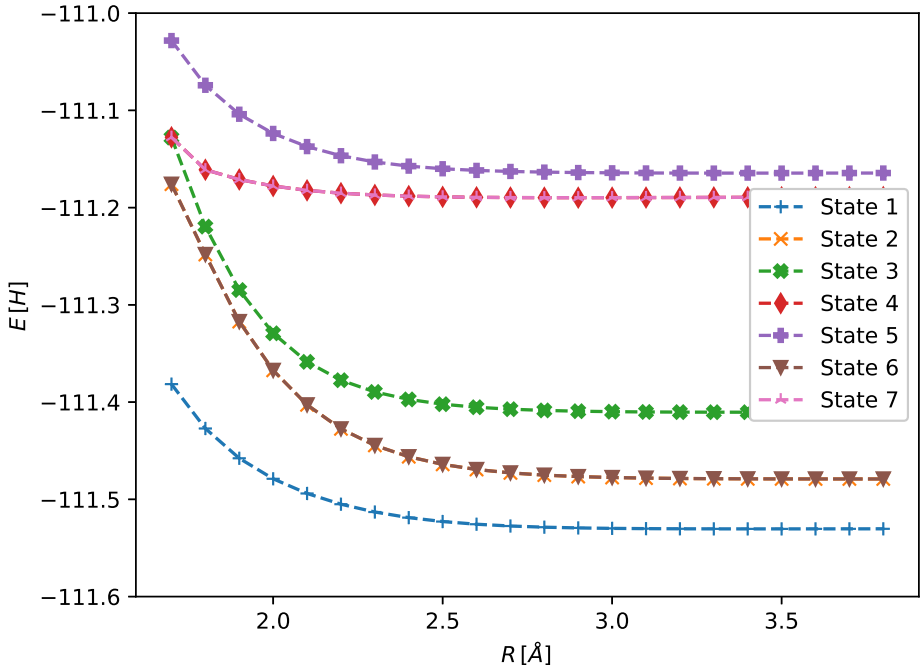

Figure B.6: PEC of the seven lowest MCSCF states computed for $\theta = 0°$, with 12A′, 3A″ orbital space and aug-cc-pVQZ basis set with $r = 1.12\,\text{Å}$.

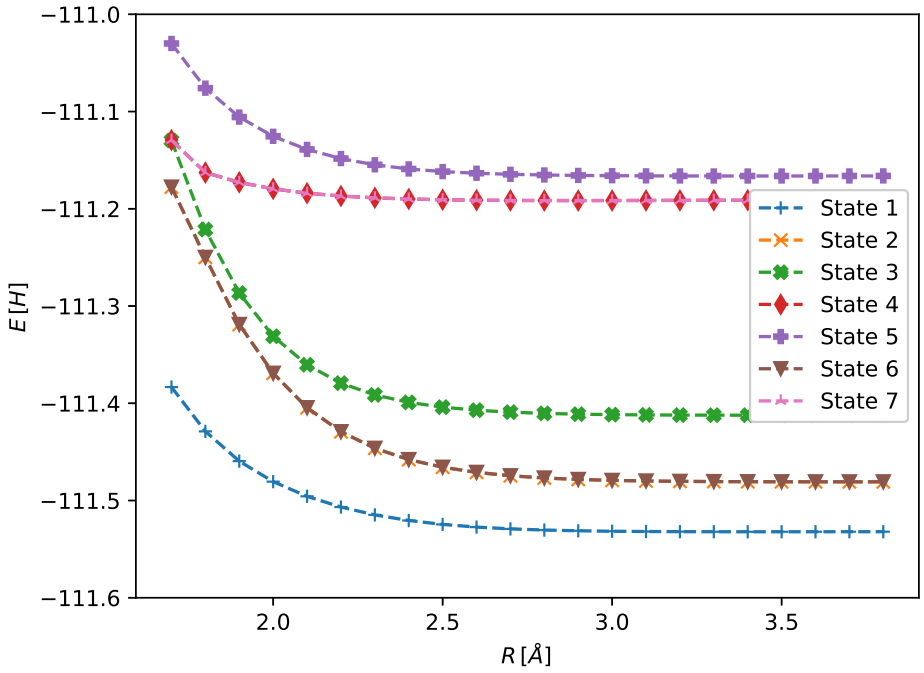

Figure B.7: PEC of the seven lowest MCSCF states computed for $\theta = 0°$, with 12A′, 3A″ orbital space and aug-cc-pV5Z basis set with $r = 1.12\,\text{Å}$.

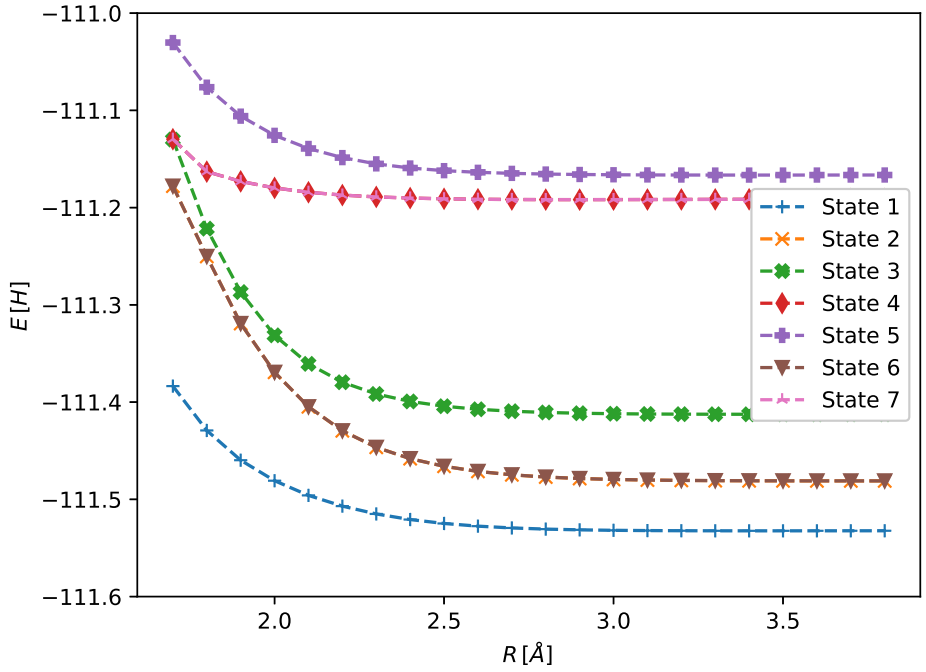

Figure B.8: PEC of the seven lowest MCSCF states computed for $\theta = 0°$, with 12A′, 3A″ orbital space and aug-cc-pV6Z basis set with $r = 1.12$ Å.

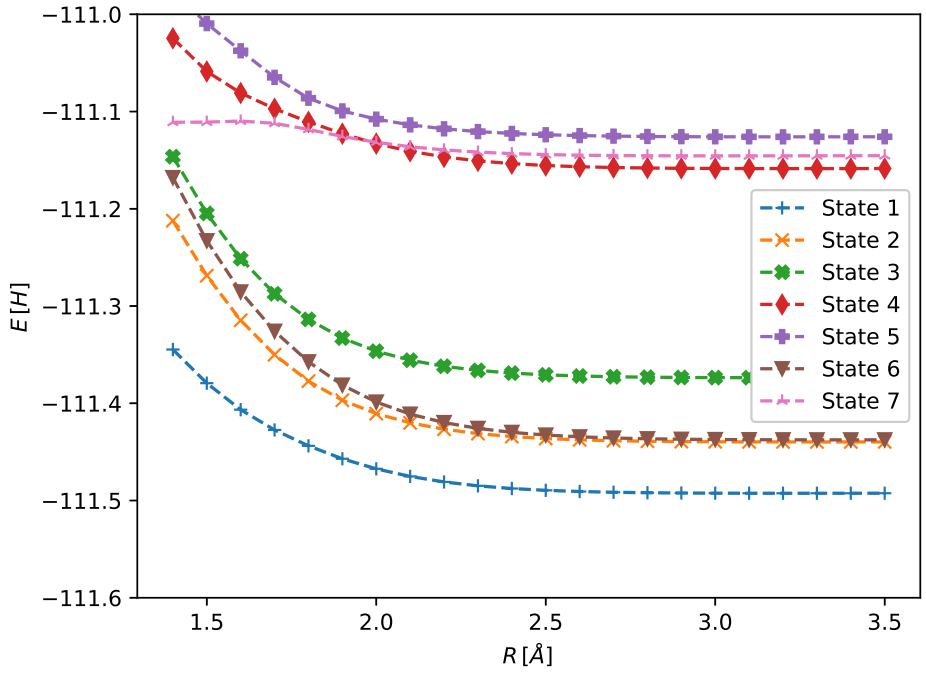

Figure B.9: PEC of the seven lowest MCSCF states computed for $\theta = 45°$, with 11A′, 2A″ orbital space and aug-cc-pVTZ basis set with $r = 1.12$ Å.

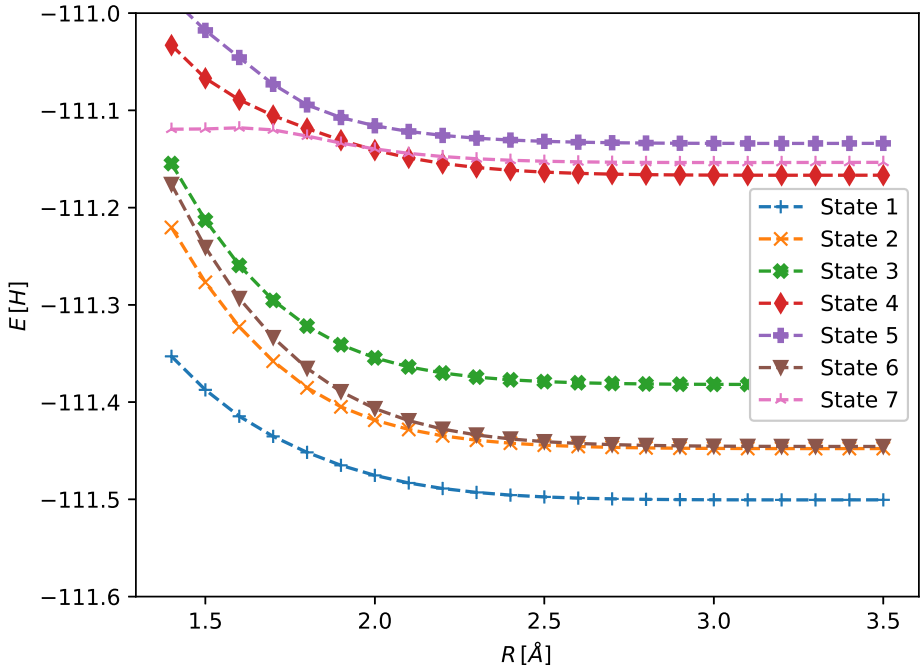

Figure B.10: PEC of the seven lowest MCSCF states computed for $\theta = 45°$, with 11A′, 2A″ orbital space and aug-cc-pVQZ basis set with $r = 1.12\,\text{Å}$.

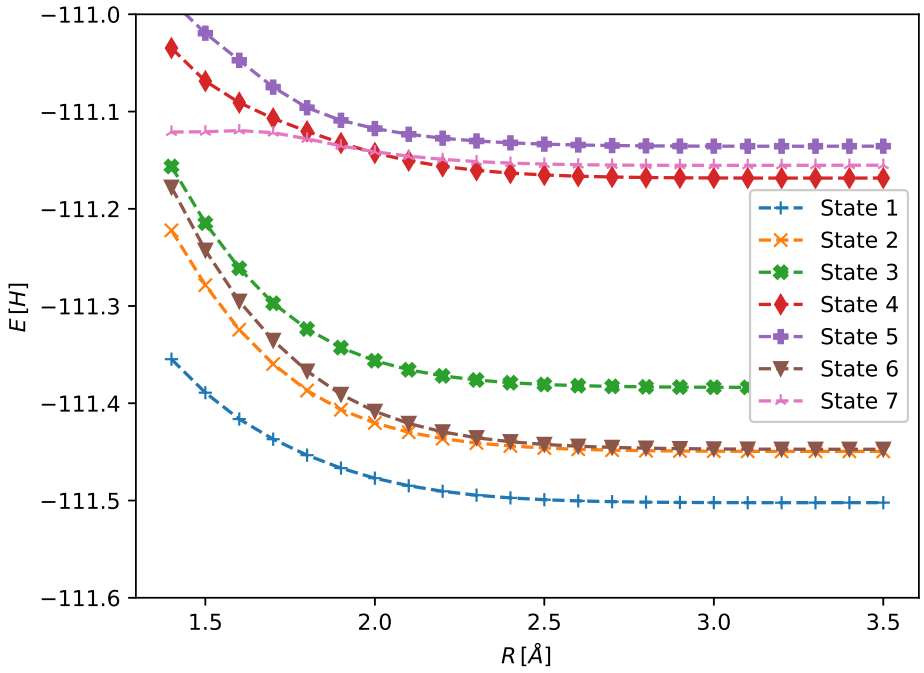

Figure B.11: PEC of the seven lowest MCSCF states computed for $\theta = 45°$, with 11A′, 2A″ orbital space and aug-cc-pV5Z basis set with $r = 1.12\,\text{Å}$.

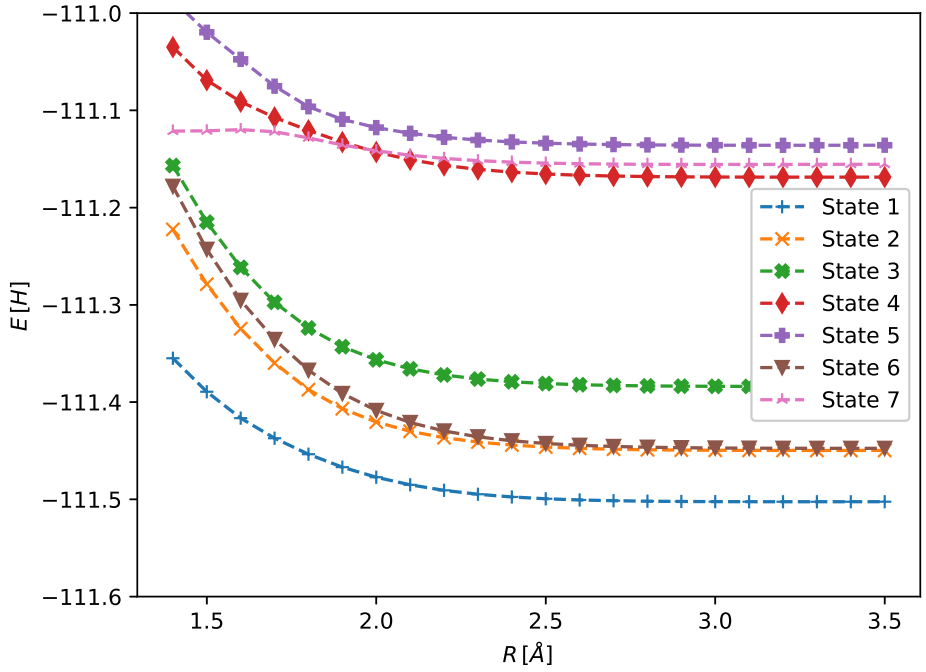

Figure B.12: PEC of the seven lowest MCSCF states computed for $\theta = 45°$, with 11A′, 2A″ orbital space and aug-cc-pV6Z basis set with $r = 1.12$ Å.

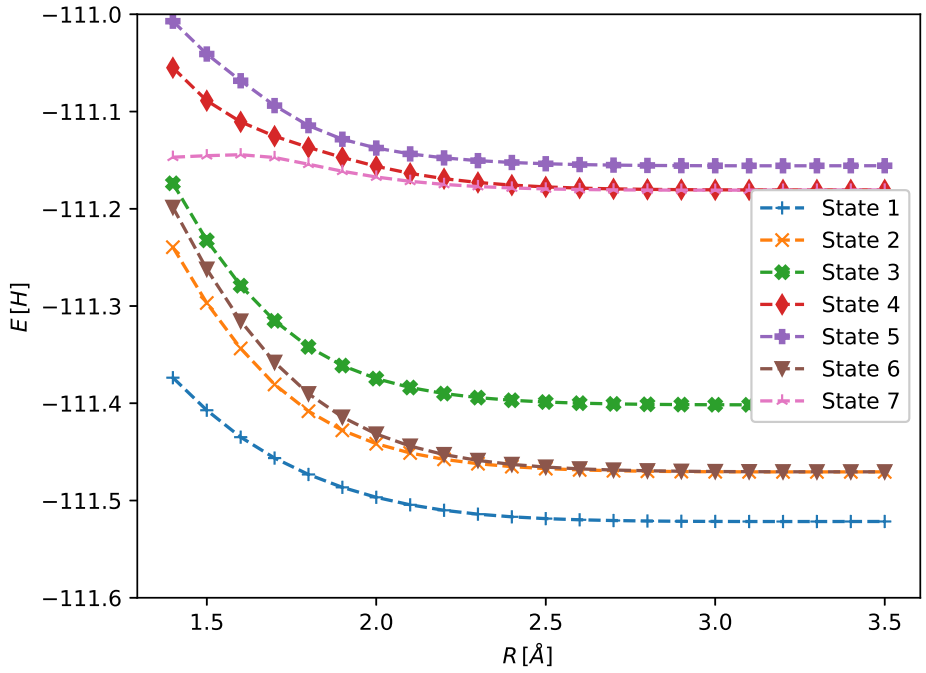

Figure B.13: PEC of the seven lowest MCSCF states computed for $\theta = 45°$, with 12A′, 3A″ orbital space and aug-cc-pVTZ basis set with $r = 1.12$ Å.

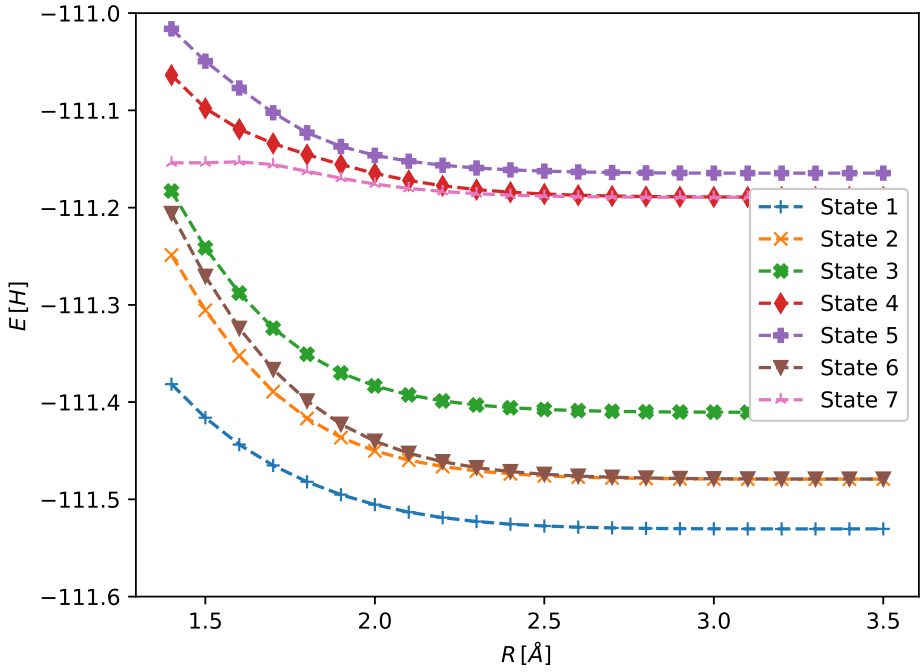

Figure B.14: PEC of the seven lowest MCSCF states computed for $\theta = 45°$, with 12A′, 3A″ orbital space and aug-cc-pVQZ basis set with $r = 1.12\,\text{Å}$.

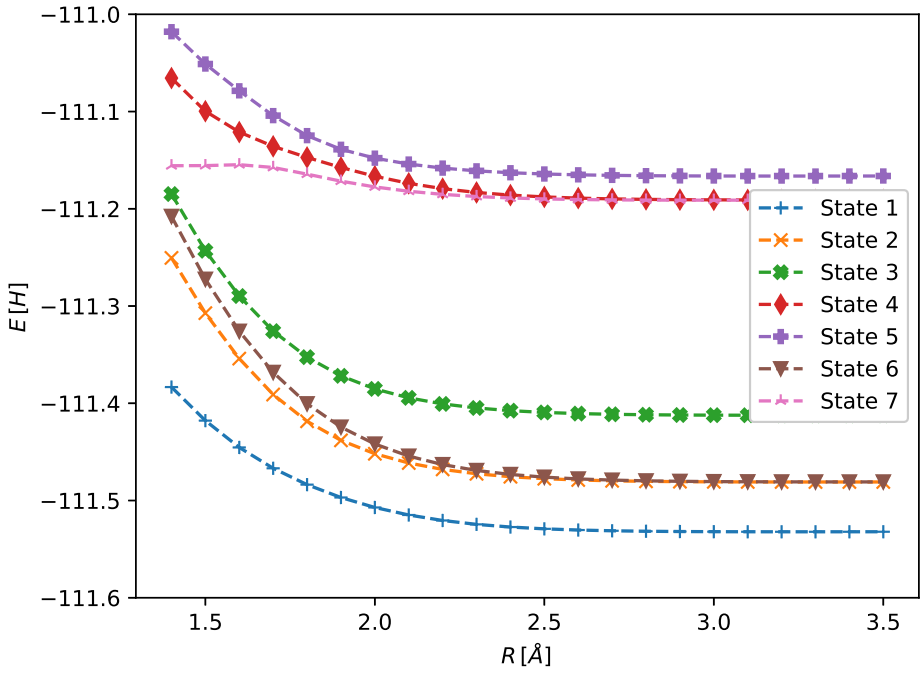

Figure B.15: PEC of the seven lowest MCSCF states computed for $\theta = 45°$, with 12A′, 3A″ orbital space and aug-cc-pV5Z basis set with $r = 1.12\,\text{Å}$.

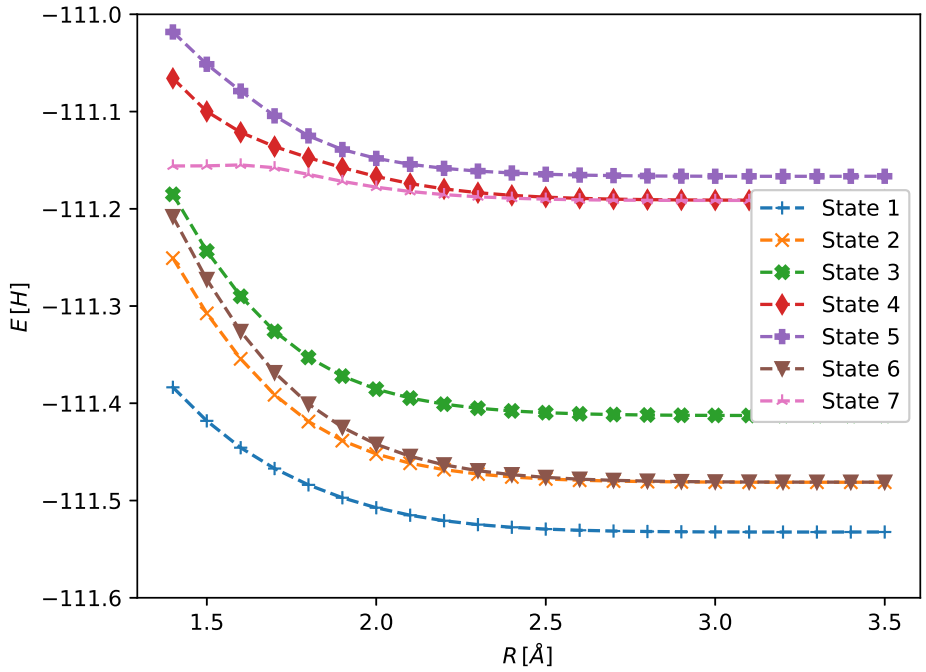

Figure B.16: PEC of the seven lowest MCSCF states computed for $\theta = 45°$, with 12A′, 3A″ orbital space and aug-cc-pV6Z basis set with $r = 1.12$ Å.

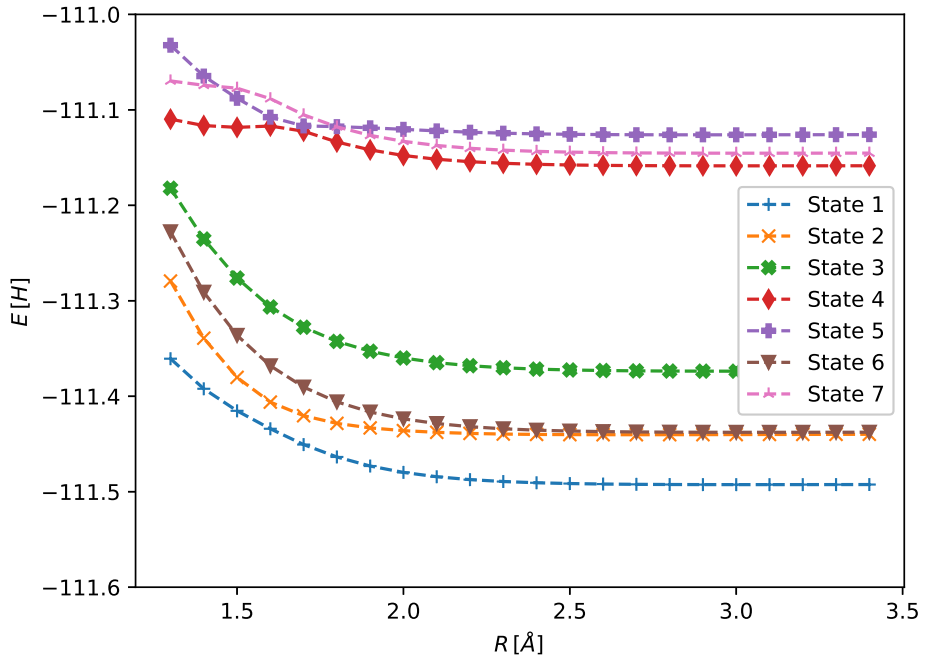

Figure B.17: PEC of the seven lowest MCSCF states computed for $\theta = 90°$, with 11A′, 2A″ orbital space and aug-cc-pVTZ basis set with $r = 1.12$ Å.

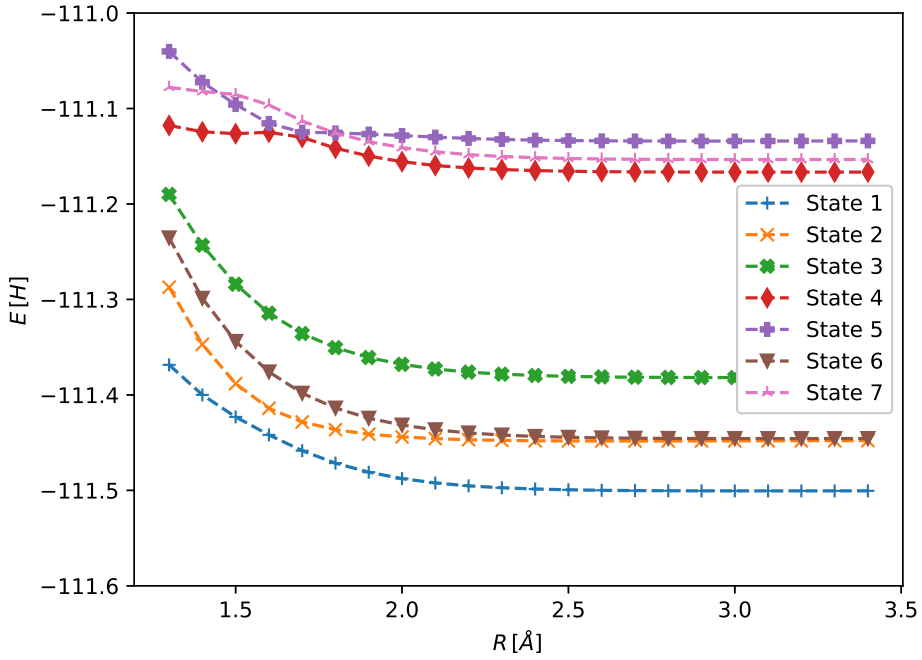

Figure B.18: PEC of the seven lowest MCSCF states computed for $\theta = 90°$, with 11A′, 2A″ orbital space and aug-cc-pVQZ basis set with $r = 1.12\,\text{Å}$.

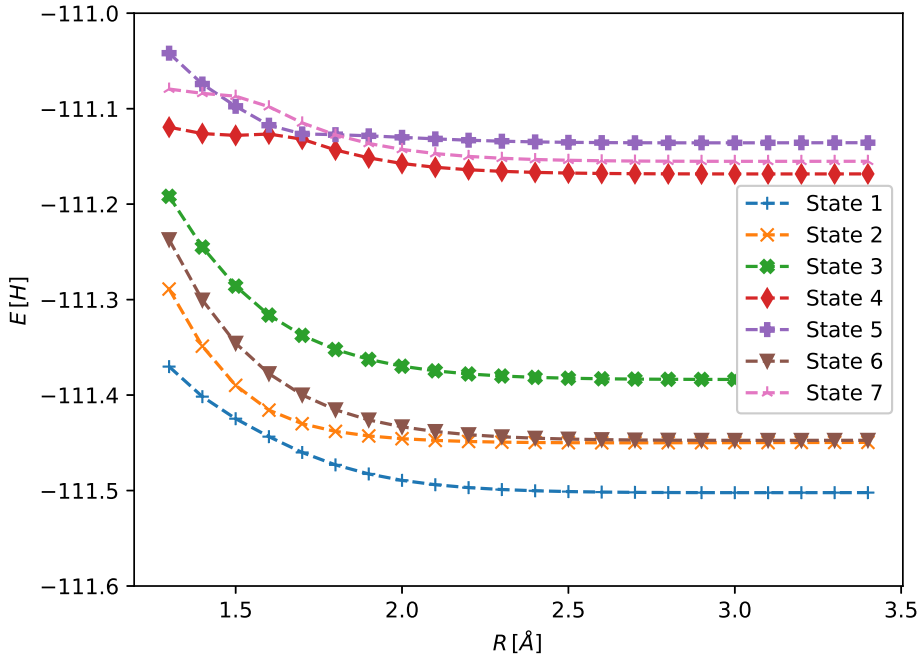

Figure B.19: PEC of the seven lowest MCSCF states computed for $\theta = 90°$, with 11A′, 2A″ orbital space and aug-cc-pV5Z basis set with $r = 1.12\,\text{Å}$.

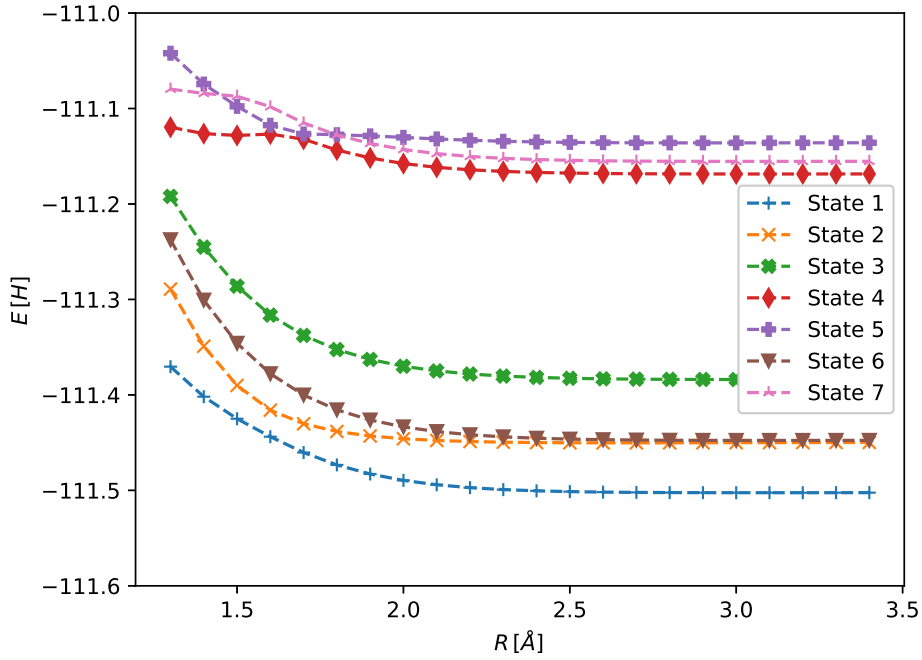

Figure B.20: PEC of the seven lowest MCSCF states computed for $\theta = 90°$, with 11A′, 2A″ orbital space and aug-cc-pV6Z basis set with $r = 1.12$ Å.

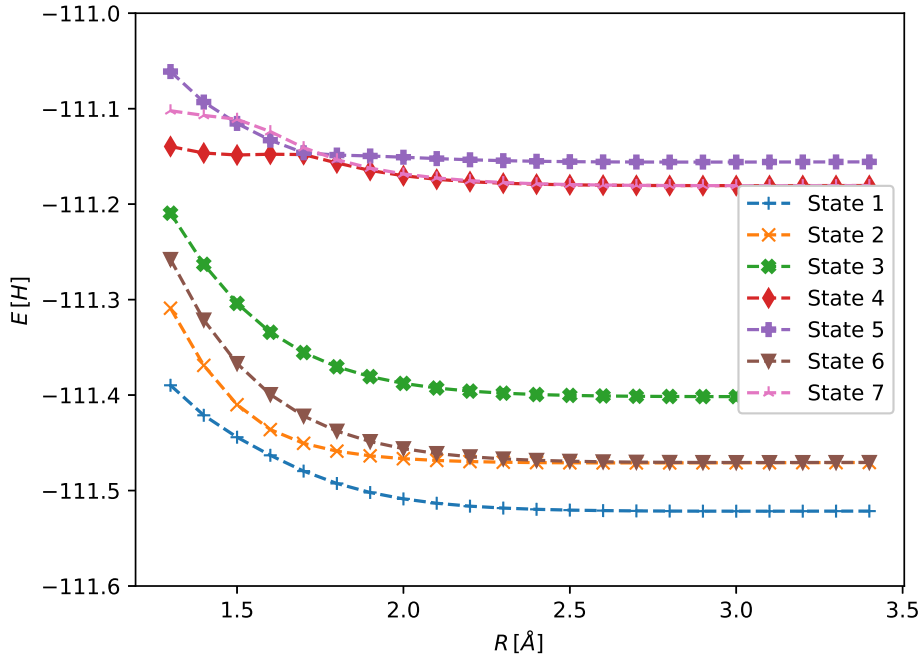

Figure B.21: PEC of the seven lowest MCSCF states computed for $\theta = 90°$, with 12A′, 3A″ orbital space and aug-cc-pVTZ basis set with $r = 1.12$ Å.

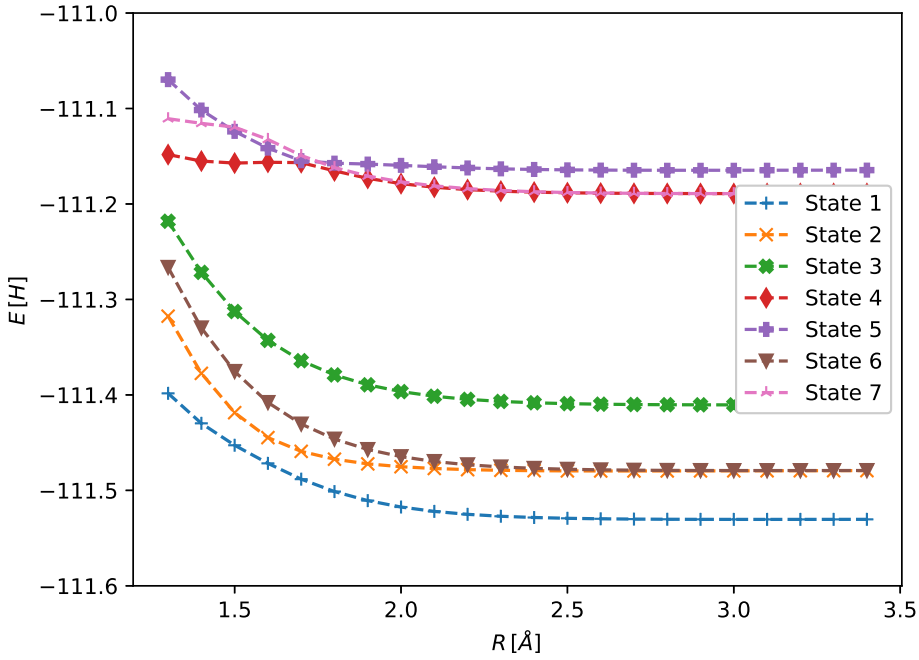

Figure B.22: PEC of the seven lowest MCSCF states computed for $\theta = 90°$, with 12A′, 3A″ orbital space and aug-cc-pVQZ basis set with $r = 1.12$ Å.

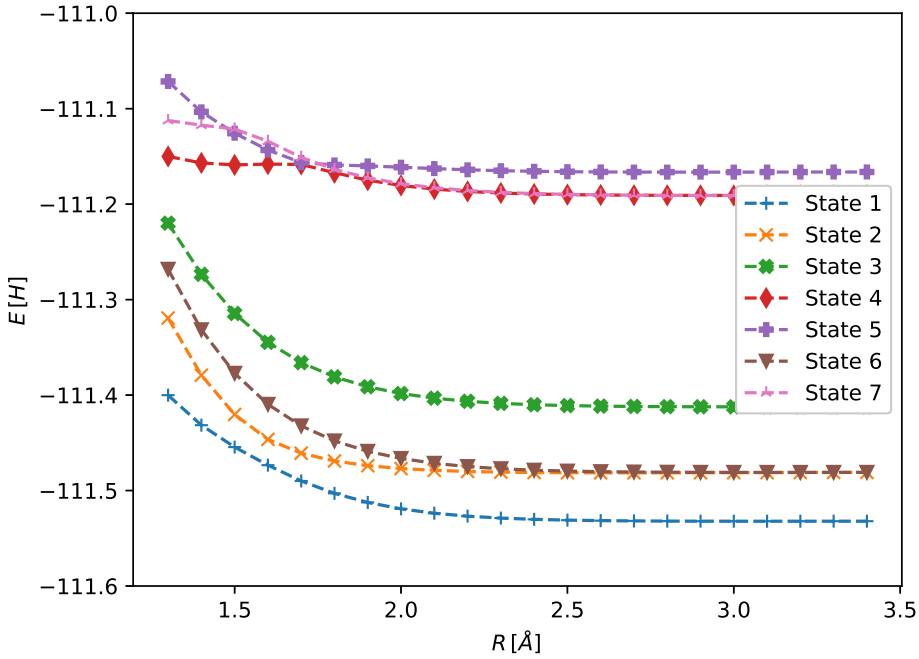

Figure B.23: PEC of the seven lowest MCSCF states computed for $\theta = 90°$, with 12A′, 3A″ orbital space and aug-cc-pV5Z basis set with $r = 1.12$ Å.

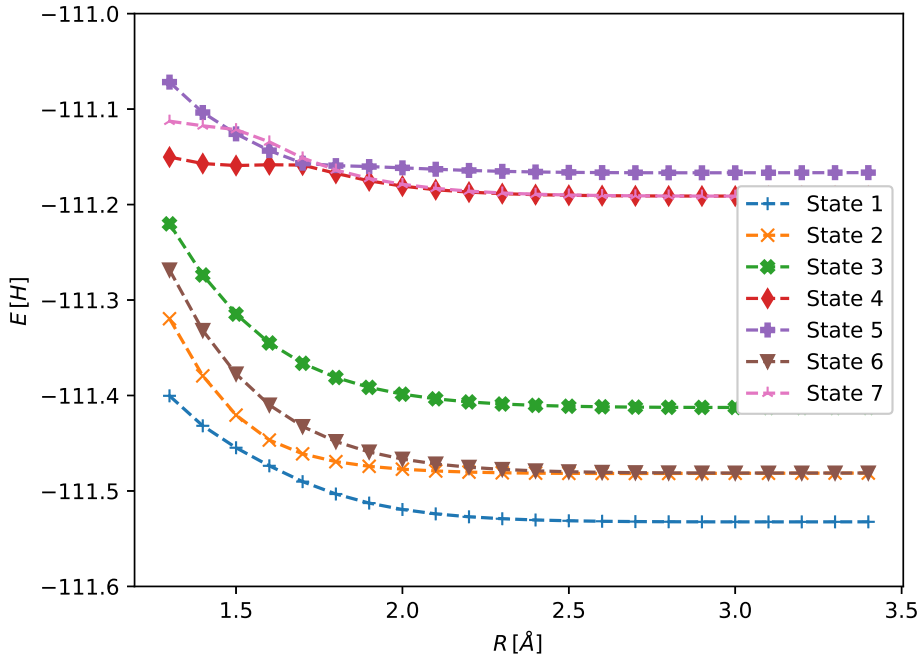

Figure B.24: PEC of the seven lowest MCSCF states computed for $\theta = 90°$, with 12A′, 3A″ orbital space and aug-cc-pV6Z basis set with $r = 1.12$ Å.